ABSTRACT

Title of Document: DESIGN AND ANALYSIS OF ADVANCED FREE SPACE OPTICAL COMMUNICATION SYSTEMS

Sugianto Trisno, Doctor of Philosophy, 2006

Directed By: Professor Christopher C. Davis
Department of Electrical and Computer Engineering

Free space optical (FSO) communication has emerged as a viable technology for broadband wireless applications. FSO technology offers the potential of high bandwidth capacity over unlicensed optical wavelengths. On long-range FSO links, atmospheric turbulence causes intensity fluctuations, which degrades links performance. The performance of an optical link can be improved by the use of a time delayed diversity technique, which takes advantage of the fact that the atmospheric path from transmitter to receiver is statistically independent for time intervals beyond the coherence time of the intensity fluctuations. Communications performance is improved because the joint probability of error is less than the probability of error from individual channels.

Theoretical analysis and experimental investigation were conducted to assess and characterize the performance of a time delayed diversity FSO system. Two experiments were conducted: inside our laboratory under simulated convective

turbulence and inter-building in clear atmospheric turbulence. In both cases, time delayed diversity system is shown to offer a notable performance improvement compared to a non-diversity FSO system, where the signal-to-noise ratio (SNR) performance can gain up to 4.7 dB and the bit error rate (BER) performance is doubled. These experimental studies confirm the effectiveness of a time delayed diversity technique to mitigate turbulence induced fading, and its optimality in a dual diversity scheme. This is the first published report of theoretical and experimental performance characteristics of FSO communication system utilizing time delayed diversity technique.

FSO technology has also emerged as a key technology for the development of rapidly deployable and secure communication and surveillance networks. In networking applications, broadcasting capability is frequently required to establish and maintain inter-node communications. One approach to deal with the broadcasting issue in FSO networking is the use of omnidirectional FSO links, which is based on non-directed line-of-sight (LOS) technique. Prototype omnidirectional FSO transceiver had been constructed and their performance investigated. Although omnidirectional FSO links cannot provide the performance of directional ones, the results suggest that they could be used in sensor networks or as alternative for traditional wireless networks, when the use of radio frequency (RF) technology is prohibited.

DESIGN AND ANALYSIS OF ADVANCED FREE SPACE OPTICAL COMMUNICATION SYSTEMS

By

Sugianto Trisno

Dissertation submitted to the Faculty of the Graduate School of the
University of Maryland, College Park, in partial fulfillment
of the requirements for the degree of
Doctor of Philosophy
2006

Advisory Committee:

Professor Christopher C. Davis, Chair
Professor Gilmer L. Blankenship
Professor Robert W. Gammon
Professor Julius Goldhar
Professor Thomas E. Murphy

Acknowledgements

I want to express my sincere gratitude to my advisor, Professor Christopher Davis, for his continuous guidance and support throughout my study at the University of Maryland, College Park. His wisdom and kindness had been invaluable and made the whole research experience enjoyable. I am also thankful to Dr. Stuart Milner, for introducing me to this field and still continuously instigating new ideas for me to explore. I also want to thank the members of my dissertation committee for their time and service.

I am thankful to all of my colleagues, present and past, in the Maryland Optics Group at the University of Maryland. I am particularly thankful to Dr. Igor Smolyaninov for introducing me to important technical aspects regarding free space optical systems. I am very much grateful to Tzung-Hsien Ho, for many discussions as well as collaborations; and most importantly, for his friendship. I also thank Dr. Quirino Balzano, Dr. Andre Schérz, Dr. Linda Wasiczko, Dr. Heba Yuksel, Aniket Desai, Clint Edwards, Jaime Llorca, and John Rzasa; for all fruitful technical and non-technical discussions we have had.

Finally, I want to thank my wife, Shierly, for supporting me during many years in graduate study. I truly appreciate her and I could not have done this without her. I also thank my parents and family for their continuous love and guidance throughout my entire life. I especially thank my brother, Tjandra, and my sister, Erni, for encouraging me and providing necessary assistance to pursue my graduate study.

But all things that are reproved are made manifest by the light:
for whatsoever doth make manifest is light.

--- The Letter of St. Paul to the Ephesians (5:13) ---

Table of Contents

Acknowledgements ii
Table of Contents iv
List of Tables vii
List of Figures viii
Chapter 1: Introduction 1
  1.1 Overview of Free Space Optical Communication 1
  1.2 Comparison of Free Space Optical and Radio Frequency Technologies 2
  1.3 Free Space Optical Communication Systems 4
  1.4 Atmospheric Optical Channel 6
  1.5 Free Space Optical Networking 9
  1.6 Dissertation Contribution: Free Space Optical System Enhancements 10
    1.6.1 Time Delayed Diversity 10
    1.6.2 Omnidirectionality 11
  1.7 Organization 13
Chapter 2: Free Space Optical System Design and Link Analysis 14
  2.1 Optical Sources and their Transmitted Fields 14
    2.1.1 Basic Characteristics of Semiconductor Lasers 14
    2.1.2 Wave Propagation in Free Space 16
    2.1.3 Beam Forming Optics 19
  2.2 Detection of Optical Radiation 20
    2.2.1 *pin* Photodiode 21
    2.2.2 Avalanche Photodiode 22
    2.2.3 Noise in the Detection Process 23
  2.3 Link Physics of the Atmospheric Channels 26
    2.3.1 Molecular Absorption and Scattering 26
    2.3.2 Optical Turbulence 28
    2.3.3 Spatial Power Spectrum Models 29
  2.4 Signal and Noise Level at Free Space Optical Receivers 30
    2.4.1 Optical Intensity Modulation Systems 31
    2.4.2 Non-coherent (Direct) Detection Model 32
    2.4.3 Signal-to-Noise Ratio in Direct Detection 34
    2.4.4 Coherent (Heterodyne) Detection Model 36
    2.4.5 Signal-to-Noise Ratio in Coherent Detection 38
  2.5 Modulation Schemes in Optical Wireless Communications 39
    2.5.1 On-Off Keying 40
    2.5.2 Manchester Encoded Signal 42
    2.5.3 Pulse Position Modulation 43
    2.5.4 Comparison of Modulation Schemes 44
    2.5.5 Effects of Timing Error on Performance 46
  2.6 Summary 47
Chapter 3: Time Delayed Diversity to Mitigate Atmospheric Induced Fading 49

3.1 Optical Wave Propagation in Atmospheric Turbulence 49
  3.1.1 Rytov Approximation 49
  3.1.2 Mean of Intensity Fluctuations 52
  3.1.3 Covariance Function of Intensity 54
  3.1.4 Distribution Models for Intensity Fluctuations 56
  3.1.5 The Effects of Atmospheric Turbulence on Performance 58
3.2 Design Considerations for a Time Delayed Diversity Scheme 61
  3.2.1 Temporal Covariance and Coherence Time 62
  3.2.2 Laser Beam Depolarization Effects 63
  3.2.3 Diversity Schemes in Free Space Optical Systems 66
3.3 Theoretical Modeling of Time Delayed Diversity System 68
3.4 Characterization of System Performance 74
  3.4.1 Bit Error Rate Performance 75
  3.4.2 The Effects of Delay Period on Receiver Performance 77
3.5 Comparison to Time Interleaving Scheme 79
3.6 Summary 81
Chapter 4: Experimental Investigations of Time Delayed Diversity System 83
4.1 Overall Descriptions of the Experimental System 83
4.2 Simulated Convective Turbulence Experiment 84
  4.2.1 Experimental System Design and Setup 85
  4.2.2 Buffer Synchronization and Communications Protocol 86
  4.2.3 The Effects of Localized Convective Turbulence 88
4.3 Results and Analysis for Simulated Convective Turbulence 90
4.4 Clear Atmospheric Turbulence Experiment 93
  4.4.1 Experimental System Design and Setup 94
  4.4.2 Link Budget Analysis 96
  4.4.3 User Interface and Data Acquisition Algorithm 98
4.5 Results and Analysis for Clear Atmospheric Turbulence 102
4.6 Polarization Modulation in Free Space Optical Communications 106
  4.6.1 Free Space Optical System using Binary Polarization Modulation......... 107
  4.6.2 Experimental Results and Analysis 109
4.7 Summary 109
Chapter 5: Omnidirectionality in Free Space Optical Communications 112
5.1 Diffuse and Line-of-Sight Transmissions 112
5.2 Theoretical Analysis of Omnidirectional Systems 114
  5.2.1 Omnidirectional Optical Link Analysis 114
  5.2.2 Modeling of Omnidirectional Receivers... 116
  5.2.3 Theoretical Performance of Omnidirectional Systems 118
5.3 Beam Forming Optics and Optical Filters 120
  5.3.1 Gaussian Beam Transformation by Lens 121
  5.3.2 Non-imaging Concentrators 123
  5.3.3 Thin Film Interference Filters 126
5.4 Construction of Omnidirectional Free Space Optical System 129
  5.4.1 Transmitter System Design 129
  5.4.2 Receiver System Design 130
5.5 Overall Transceiver Experimental Performance 132

5.6 System Level Design Issues 135
5.7 Summary 136
Chapter 6: Conclusions 138
6.1 Summary of Main Contributions 138
6.2 Future Work 139
Bibliography 142

List of Tables

Table 1.1: Properties of terrestrial FSO and RF communications. 4
Table 2.1: Basic characteristics of laser diodes. 16
Table 2.2: Comparison of baseband intensity modulation techniques. 46
Table 3.1: Demodulation error in a receiver using logical OR as digital combiner. .. 72
Table 4.1: Link budget analysis for 1 km experimental FSO link. 97
Table 5.1: Design parameters and performance of various CPCs. 126

List of Figures

Figure 1.1: Block diagram of FSO communication system. 5
Figure 1.2: FSO link loss due to various atmospheric conditions (clear, thin fog, moderate fog, and thick fog), for system with $P_T = 10$ mW, $q = 1$ mrad, and receiver diameter of 100 mm. 8
Figure 2.1: Intensity distribution profile in propagating Gaussian beam. 18
Figure 2.2: Example of beam collimation in long-range FSO links. 19
Figure 2.3: Spatial power spectrums for Kolmogorov, Tatarskii, and Von Kármán, from Eqs. (2.21) – (2.23), calculated for $l_0 = 10$ mm and $L_0 = 10$ m. 31
Figure 2.4: Block diagram of direct detection optical receiver. 33
Figure 2.5: SNR performance of direct detection FSO system with $q_B = 2$ mrad, $\Re = 0.45$ A/W, $D = 100$ mm, and $\Delta f = 1$ GHz; calculated for 100 m and 1 km links. 35
Figure 2.6: Block diagram of coherent detection optical receiver. 36
Figure 2.7: SNR performance of coherent detection FSO system with $P_{LO} = 1$ mW, $q_B = 2$ mrad, $\Re = 0.45$ A/W, $D = 100$ mm, and $\Delta f = 1$ GHz; calculated for 100 m and 1 km links. 39
Figure 2.8: BER performance for OOK (NRZ and RZ), from Eq. (2.38), and *L*-PPM ($L = 2$, 4, and 8), from Eq. (2.42). 45
Figure 2.9: Power spectrum of the transmitted signals for OOK (NRZ and RZ), from Eq. (2.39), and *L*-PPM ($L = 2$, 4, and 8), from Eq. (2.43). 46
Figure 3.1: Rytov variance calculated for atmospheric turbulence with C_n^2 value ranges from 10^{-14} to 10^{-12} $m^{-2/3}$ and $l = 785$ nm. 50
Figure 3.2: Aperture averaging factor versus receiver aperture size calculated from Eq. (3.21) for $L = 1$ km and $l = 785$ nm. 56
Figure 3.3: Average SNR performance in the presence of optical turbulence with $s^2 = 0.001$, 0.01, and 0.1; calculated from Eq. (3.28) for $\Lambda = 0.001$ 59
Figure 3.4: Theoretical BER performance of FSO system using constant threshold, from Eq. (3.31), and dynamic threshold, from Eq. (3.32); calculated for $s^2 = 0.001$, 0.01, and 0.1. The solid curve depicts BER performance in the absence of turbulence. 61
Figure 3.5: Temporal covariance functions for $s^2 = 0.002$, 0.01, and 0.05 obtained from measurements made with $L = 1$ km and $l = 785$ nm. The theoretical curves were computed from Eq. (3.19) and the use of Taylor turbulence hypothesis. 64
Figure 3.6: Mean of intensity depolarization calculated for FSO link with $L = 1$ km, $l = 785$ nm, and $l_0 = 1$ mm. 66
Figure 3.7: Average BER performance of FSO receiver with diversity branch *M* ranges from 1 to 4 and calculated for $s^2 = 0.001$ and 0.01. 69

Figure 3.8: Block diagram of theoretical model of time delayed diversity system. ... 70
Figure 3.9: Comparison of the false alarm, miss, and average error probabilities in a FSO link calculated from Eqs. (3.29) – (3.31) for $s^2 = 0.002$, 0.01, and 0.05.. 73
Figure 3.10: Average BER performance for practical system model, from Eq. (3.48), calculated for no diversity, $t = 0$, $t = t_c$, and $t \to \infty$ cases. The performance was evaluated for turbulence with $s^2 = 0.002$ and 0.01. 76
Figure 3.11: Average BER performance for theoretical system model, from Eq. (3.46), calculated for no diversity, $t = 0$, $t = t_c$, and $t \to \infty$ cases. The performance was evaluated for turbulence with $s^2 = 0.002$ and 0.01. 77
Figure 3.12: Effects of variable delay in reducing the average BER calculated for $s^2 = 0.002$. The BER reduction factor is defined as the average BER computed at delay period t, normalized to its value at $t = 1$ ms. 78
Figure 3.13: Block diagram of FSO receiver with time interleaving. 80
Figure 3.14: Comparison of SNR performance between time interleaving and time delayed diversity FSO systems calculated for $s^2 = 0.001$, 0.01, and 0.1; and $t_c \to \infty$ 81
Figure 4.1: Time delayed diversity FSO experiment in convective turbulence link. . 87
Figure 4.2: Flowchart of data transmissions and synchronizations. 89
Figure 4.3: Error statistics of the hot plates generated turbulence measured for s^2 ranges from 9×10^{-4} to 2×10^{-3}. The theoretical curves were calculated from Eq. (3.32) for $l = 1.3$ µm, and $s^2 = 5\times10^{-4}$ and 5×10^{-3}. 90
Figure 4.4: Temporal covariance functions of the convective turbulence obtained from measurements made with $l = 1.3$ µm, for $s^2 = 9.6\times10^{-4}$ and 1.6×10^{-3}. 91
Figure 4.5: BER performance of time delayed diversity FSO system measured under convective turbulence with $s^2 = 9.6\times10^{-4}$, and for the case of no delay, $t = 20$ ms, 40 ms, and 60 ms. 92
Figure 4.6: BER performance of time delayed diversity FSO system measured under convective turbulence with $s^2 = 1.6\times10^{-3}$, and for the case of no delay, $t = 20$ ms, 40 ms, and 60 ms. 93
Figure 4.7: Picture of time delayed diversity FSO transmitter system in clear atmospheric turbulence link. 95
Figure 4.8: Picture of time delayed diversity FSO receiver system in clear atmospheric turbulence link. 96
Figure 4.9: Flowcharts of user interface and control processes. 99
Figure 4.10: Measurements of intensity ratio of orthogonally polarized signals conducted for inter-building FSO link with $l = 785$ nm; $s^2 = 0.005$, 0.01, and 0.05. 103
Figure 4.11: Temporal covariance functions of the atmospheric turbulence obtained from measurements made with $l = 785$ nm; $s^2 = 0.01$, 0.02, and 0.05. 104
Figure 4.12: BER performance of time delayed diversity FSO system measured under clear atmospheric turbulence with $s^2 = 0.01$, for the case of no diversity, no delay, $t = 5$ ms, 10 ms, and 20 ms. The theoretical curves were calculated from

Eq. (3.48) for the case of no diversity and dual diversity with independent channels. 105
Figure 4.13: BER performance of time delayed diversity FSO system measured under clear atmospheric turbulence with $s^2 = 0.02$, for the case of no diversity, no delay, $t = 5$ ms, 10 ms, and 20 ms. The theoretical curves were calculated from Eq. (3.48) for the case of no diversity and dual diversity with independent channels. 106
Figure 4.14: BER performance of time delayed diversity FSO system measured under clear atmospheric turbulence with $s^2 = 0.05$, for the case of no diversity, no delay, $t = 5$ ms, 10 ms, and 20 ms. The theoretical curves were calculated from Eq. (3.48) for the case of no diversity and dual diversity with independent channels. 107
Figure 4.15: Performance comparison between OOK and PolSK FSO system measured under convective turbulence with $s^2 = 9.6\times10^{-4}$ and 1.6×10^{-3} 110
Figure 5.1: Two types of non-directed optical links: (a) LOS, and (b) diffuse. 112
Figure 5.2: Number of required transmitters for spherical omnidirectional coverage calculated for angular separations at full and half beam divergence. 116
Figure 5.3: FSO loss experienced in omnnidirectional links calculated from Eq. (5.5) for system having optimum performance at $q_B = 1$ mrad. 117
Figure 5.4: Optical power received by omnidirectional receiver with –35 dBm, –45 dBm, shot noise, and Johnson noise limit performance; calculated for $\Delta f = 1$ kHz and $P_T = 1$ mW, 10 mW, and 100 mW. 119
Figure 5.5: Optical power received by omnidirectional receiver with –35 dBm, –45 dBm, shot noise, and Johnson noise limit performance; calculated for $\Delta f = 1$ MHz and $P_T = 1$ mW, 10 mW, and 100 mW. 120
Figure 5.6: SNR performance calculated for $P_T = 1$ mW, 10 mW, and 100 mW, under practical and ideal shot noise limited receivers, for $\Delta f = 1$ kHz. The horizontal line depicts the operational SNR value corresponds to a BER of 10^{-9}. 121
Figure 5.7: SNR performance calculated for $P_T = 1$ mW, 10 mW, and 100 mW, under practical and ideal shot noise limited receivers, for $\Delta f = 1$ MHz. The horizontal line depicts the operational SNR value corresponds to a BER of 10^{-9}. 122
Figure 5.8: Diagram of a Gaussian beam transformed by a concave lens. 124
Figure 5.9: Example of rays entering and then expanding from the back of a CPC. 125
Figure 5.10: Dependence of transmission wavelength on light incidence angle calculated from Eq. (5.21) for a thin film interference filter with $n_E = 2.05$ ... 128
Figure 5.11: Block diagram of the transmitter in an omnidirectional FSO system. . 131
Figure 5.12: Block diagram of the receiver in an omnidirectional FSO system. 132
Figure 5.13: Prototype of the omnidirectional FSO communication system. 133
Figure 5.14: Measurements of achievable data rate in omnidirectional FSO link. The theoretical curve was calculated based on Eq. (5.9) for $\Gamma \cong 22.7$ dB. 134
Figure 5.15: BER performance of prototype omnidirectional FSO transceiver. The theoretical curve was calculated based on Eq. (2.38) for $\Delta f \cong 730$ kHz. 135

Chapter 1: Introduction

1.1 Overview of Free Space Optical Communication

Optical wireless communication has emerged as a viable technology for next generation indoor and outdoor broadband wireless applications. Applications range from short-range wireless communication links providing network access to portable computers, to last-mile links bridging gaps between end users and existing fiber optic communications backbones, and even laser communications in outer-space links [1]. Indoor optical wireless communication is also called wireless infrared communication, while outdoor optical wireless communication is commonly known as free space optical (FSO) communication.

In applying wireless infrared communication, non-directed links, which do not require precise alignment between transmitter and receiver, are desirable. They can be categorized as either line-of-sight (LOS) or diffuse links. LOS links require an unobstructed path for reliable communication, whereas diffuse links rely on multiple optical paths from surface reflections. On the other hand, FSO communication usually involves directed LOS and point-to-point laser links from transmitter to receiver through the atmosphere. FSO communication over few kilometer distances has been demonstrated at multi-Gbps data rates [2].

FSO technology offers the potential of broadband communication capacity using unlicensed optical wavelengths. However, in-homogeneities in the temperature and pressure of the atmosphere lead to refractive index variations along the transmission path. These refractive index variations lead to spatial and temporal variations in optical intensity incident on a receiver, resulted in fading. In FSO communication, faded links caused by such atmospheric effects can cause performance degradation manifested by increased bit error rate (BER) and transmission delays [3].

FSO technology has also emerged as a key technology for the development of rapidly deployable, secure, communication and surveillance systems, which can co-operate with other technologies to provide a robust, advanced sensor communication network. However, the LOS requirement for optical links reduces flexibility in forming FSO communication networks. Compared with broadcast radio frequency (RF) networks, FSO networks do not have an obvious simple ability to distribute data and control information within the network.

The objective of the research work presented here is to answer the following questions regarding: 1) how to improve the performance of FSO links for long-range FSO communications, where atmospheric turbulence effects can be severe; and 2) how to accommodate the broadcast requirements for short-range FSO sensor networking applications. These challenging problems are addressed by two different approaches, yet there is a possibility that these two techniques can be combined and realized in one general purpose FSO communication system.

1.2 Comparison of Free Space Optical and Radio Frequency Technologies

Traditionally, wireless technology is almost always associated with radio transmission, although transmission by carriers other than RF waves, such as optical waves, might be more advantageous for certain applications. The principal advantage of FSO technology is very high bandwidth availability, which could provide broadband wireless extensions to Internet backbones providing service to end-users. This could enable the prospect of delay-free web browsing and data library access, electronic commerce, streaming audio and video, video-on-demand, video teleconferencing, real-time medical imaging transfer, enterprise networking and work-sharing capabilities [4], which could require as much as a 100 Mbps data rate on a sustained basis.

In addition, FSO permits the use of narrow divergence, directional laser beams, which if deployed appropriately, offer essentially very secure channels with low probability of interception or detection (LPI/LPD). Narrow FSO beams also have considerable obscuration penetrating capability. For example, penetration of dense fog over a kilometer distance is quite feasible at Gbps data rates with beam divergence of 0.1 mrad. The tight antenna patterns of FSO links allow considerable spatial re-use, and wireless networks using such connectivity are highly scalable, in marked contrast to ad-hoc RF networks, which are intrinsically non-scalable [5].

However, FSO has some drawbacks as well. Since a LOS path is required from transmitter to receiver, narrow beam point-to-point FSO links are subject to atmospheric turbulence and obscuration from clouds, fog, rain, and snow [2,6] causing performance degradation and possible loss of connectivity. In addition, FSO links can have a relatively short range, because the noise from ambient light is high, and also because the square-law nature of direct detection receiver doubles the effective path loss (in dB) when compared to a linear detector. Table 1.1 summarizes the difference between FSO and RF technologies.

Table 1.1: Properties of terrestrial FSO and RF communications.

	FSO Links	RF Links
Typical Data Rate	100 Mbps to ~Gbps	Less than 100 Mbps[1]
Channel Security	High	Low
Component Dimension	Small	Large
Networking Architecture	Scalable	Non-scalable
Source of Signal Degradation	Atmospheric turbulence and obscuration	Multipath fading, rain, and user interferences

Obviously, FSO communication will not replace RF communication, rather they will co-exist. Hybrid FSO/RF networks combine the advantages and avoid the disadvantages of FSO or RF alone. Even if the FSO connectivity cannot be provided all the time, the aggregate data rate in such networks is markedly greater than if RF links were used alone. RF alone does not have the bandwidth for the transfer of certain types of data, for example high-definition video quality full-spectrum motion imagery. Hybrid wireless networks will provide maximum availability and capacity.

1.3 Free Space Optical Communication Systems

The major subsystems in an FSO communication system are illustrated in Fig. 1.1. A source producing data input is to be transmitted to a remote destination. This source has its output modulated onto an optical carrier; typically laser, which is then transmitted as an optical field through the atmospheric channel. The important aspects of the optical transmitter system are size, power, and beam quality, which determine laser intensity and minimum divergence obtainable from the system. At the receiver,

---

[1] More expensive new millimeter wave systems have recently become available, which provide data rates larger than 1 Gbps (e.g. GigaBeam WiFiber, http://www.gigabeam.com).

the field is optically collected and detected, generally in the presence of noise interference, signal distortion, and background radiation. On the receiver side, important features are the aperture size and the f/-number, which determine the amount of the collected light and the detector field-of-view (FOV).

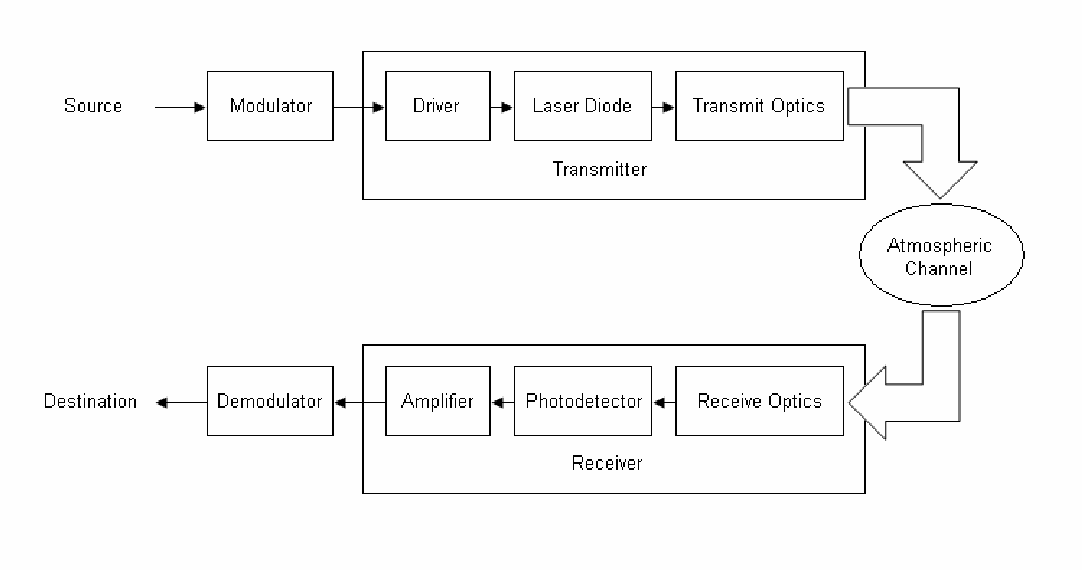

Figure 1.1: Block diagram of FSO communication system.

The modulation of the source data onto the electromagnetic wave carrier generally takes place in three different ways: amplitude modulation (AM), frequency modulation (FM), or phase modulation (PM), each of which can be theoretically implemented at any frequency. For an optical wave, another modulation scheme is also often used, namely intensity modulation (IM). Intensity is defined as flow energy per unit area per unit time expressed in W/m^2, and is proportional to the square of the field's amplitude. The light fields from laser sources then pass beam forming optics to produce a collimated beam. This practice is equivalent to providing antenna gain in RF systems.

There are two basic types of optical receivers: non-coherent receivers and coherent receivers. Non-coherent receivers directly detect the instantaneous power of the collected optical field as it arrives at the receivers, thus are often called direct or power detection receivers. These receivers represent the simplest type of implementation and can be used whenever the transmitted information occurs in the power variation (i.e. IM) of the optical field. Coherent receivers, better known as heterodyne receivers, optically mix a locally generated lightwave field with the received field, and the combined wave is photodetected. These receivers are used when information is modulated onto the optical carrier using AM, FM, or PM, and are essential for FM or PM detection.

The detection of optical fields is effected by various noise sources present at the receiver. The three dominant sources in FSO communications are: background ambient light, photodetector induced noise, and electronic thermal noise in circuits. Although background radiation may be reduced by the use of optical filtering, it still provides significant interference in the detection process. The detector quantum noise originates from the randomness of the photon counting process at the photodetector. The thermal noise can be modeled as additive white Gaussian noise (AWGN), whose spectral level is directly proportional to the receiver temperature.

1.4 Atmospheric Optical Channel

In FSO communication links, absorption of the beam by the atmosphere can be important, especially in adverse weather conditions of fog, snow, heavy rain, or obscuration. The combined effects of direct absorption and scattering of laser light can be described by a single path-dependent attenuation coefficient $\alpha(z)$. The power received at receiver can easily be calculated for links without significant turbulence effects. The received power P_R for a receiver with receiver area *A*, range *L*, and beam divergence angle q varies as

$$P_R \approx \frac{A}{pq^2 L^2} e^{-aL} P_T , \tag{1.1}$$

where P_T is the transmitted power, and a in this case is a constant value averaged over the propagation path *L*.

The received power can be increased by increasing the transmitter power, the receiver area, or by reducing the beam divergence of the transmitter beam, which is diffraction limited. For FSO system with transmitted optical power of 10 mW, beam divergence of 1 mrad, and receiver diameter of 100 mm, the received power is still exponentially dependent on the atmospheric attenuation coefficient, as illustrated in Fig. 1.2. For a typical receiver sensitivity of -35 dBm, only an operational range less than 300 m can be achieved under heavy obscuration conditions. Even under light obscuration conditions, the link margin is reduced quite significantly compared with clear air conditions.

When turbulence effects are included, the effects of the atmosphere are in a sense more subtle. This optical turbulence is caused almost exclusively by temperature variations in the atmosphere, resulting in random variations of refractive index. An optical wave propagating through the atmospheric turbulence will experience random amplitude and phase fluctuations, which will generate a number of effects: break up of the beam into distinct patches of fluctuating illumination, wander of the centroid of the beam, and increase in the beam width over the expected diffraction limit. For longer links, the problems presented by atmospheric turbulence are quite severe [2,3], since the average power received at the FSO receiver will decrease even more.

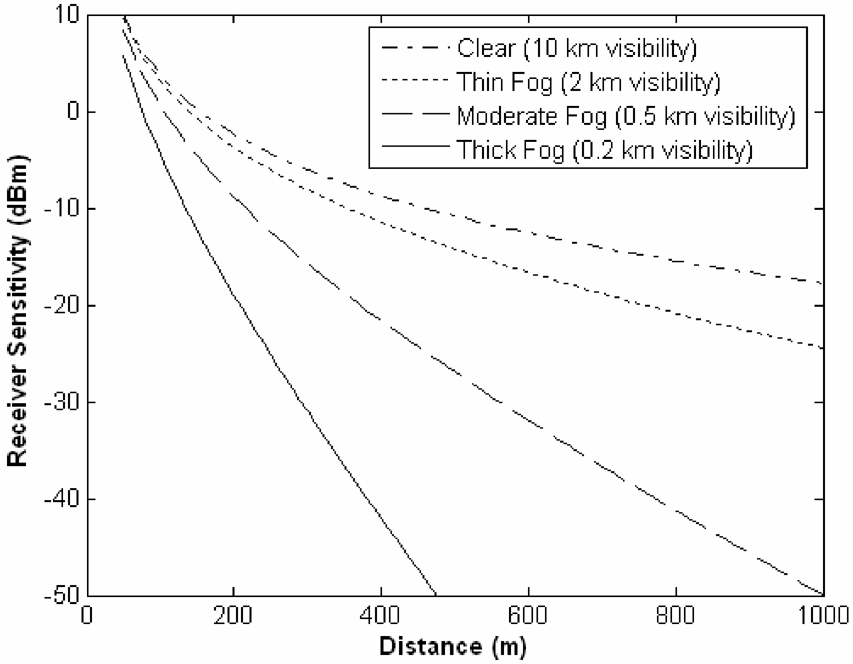

Figure 1.2: FSO link loss due to various atmospheric conditions (clear, thin fog, moderate fog, and thick fog), for system with $P_T = 10$ mW, $q = 1$ mrad, and receiver diameter of 100 mm.

Besides power loss, the atmosphere may also distort the optical wave shape during propagation through dense clouds. This is particularly true for transmission of high power, narrow optical pulses, in which the atmospheric scattering can cause pulse broadening through multipath effects. Scattered pulse fields may be reflected toward the receiver and still have appreciable energy to produce a distorted optical pulse shape. If an optical pulse is transmitted from the source, the pulse signals along the scattered paths arrive with delays relative to the direct path and combine to yield a wider, broadened optical field pulse from that transmitted.

1.5 Free Space Optical Networking

The individual FSO link between transmitter and receiver can be naturally extended to an FSO network topology. FSO networks could serve in a metropolitan area to form a backbone of base stations providing service to both fixed and mobile users. For some other application where no base station is present, FSO transceivers may need to be able to communicate with one another to form ad-hoc sensor networking. In both cases, a scalable, robust, and controlled network topology is required [7].

A major drawback of directed LOS systems is their inability to deal with broadcast communication modes. In networking, broadcasting capability is frequently required in order to establish communication among multiple nodes. With this capability, networking data and control messages can easily be flooded over the whole network. This problem can be eliminated by using non-directed LOS optical links, which can be described as omnidirectional links. There have been a number of systems based on non-directed communications [8,9]. They provide reliable performance mainly in short-range applications, i.e. several to tens of meters.

For longer range networking applications, such as in a military context with a network of high-altitude aircraft or in battlefield scenarios, only directional FSO links can provide high data rate capability and channel security. For directional FSO links, pointing, acquisition, and tracking (PAT) schemes are necessary in order to establish and allow the flow of information within the networks [10,11]. PAT involves a beam-steering device, which may be mechanical, such as galvo-mirror or gimbal; or non-mechanical, using an acousto-optic crystal or piezo-electric actuator. In typical directional FSO systems, there is a trade-off between the requirements of maximizing received optical power, yet minimizing the PAT sensitivity of the system.

1.6 Dissertation Contribution: Free Space Optical System Enhancements

In this dissertation, two advanced practical designs of FSO systems are presented for dealing with two key issues in FSO communications: atmospheric turbulence on long-range links and multi-connectedness for short-range links. On long-range links, atmospheric turbulence causes intensity fluctuations, which increase bit errors in FSO links. The performance of an optical link can be improved by the use of a time delayed diversity technique. For short-range links, omnidirectionality can be satisfied using large angle beam divergence transmitters to provide broadcasting capability.

1.6.1 Time Delayed Diversity

Two useful parameters for describing atmospheric turbulence are the coherence length and coherence time of the intensity fluctuations. It has been determined that aperture averaging can significantly reduce scintillation noise, if the receiver aperture can be made much larger than the transverse coherence length [12]. In addition, if the receiver observation time during each bit interval can be made much longer than the coherence time, time averaging can also reduce scintillation noise. Unfortunately, because of receiver size limitations, and for typical data rates in optical communication systems, these techniques do not always apply.

Several different techniques have been proposed to mitigate scintillation noise when aperture or time averaging cannot be used effectively [13,14]. In general, they can be categorized as spatial or temporal correlation approaches. In the spatial correlation approach, multiple receivers with small apertures are used to collect light at laterally separated spatial locations. The distance between the receivers should be large enough that spatial diversity results; otherwise a maximum-likelihood (ML) scheme is needed to obtain optimum detection. In the temporal correlation approach, only a single receiver is needed. ML detection can then be used if the receiver has knowledge of the temporal fading distribution.

In contrast, we have proposed a time delayed diversity scheme and developed a prototype of this system, which has been shown to significantly reduce the bit errors in a fading atmospheric channel [15,16]. In this scheme, the data stream is transmitted twice, in two orthogonal polarization channels, with a delay between the transmissions that is longer than the coherence time of the atmosphere. The bit errors are reduced because if one bit is detected in error because of channel fluctuations, then there is an independent probability of correctly re-detecting the same bit because the diversity delay is longer than the memory time of the channel.

This research focuses on our analytical and experimental work in the deployment of time delayed diversity FSO systems, including their design, construction, and testing. Our goals are to characterize the performance limit of the time delayed diversity scheme and to explore related system design and implementation issues.

1.6.2 Omnidirectionality

In wireless infrared networking, broadcasting capability can be suitably provided by non-directional diffuse links [17,18]. A diffuse link exploits the excellent reflective properties of most indoor environments. Diffuse systems also typically require higher power lasers. In this case, the optical signal in a diffuse link can undergo multiple reflections and still have appreciable energy. However, the multipaths can cause dispersion and limit the system to lower bit rates. On the other hand, there are no multipaths in non-directional LOS links, so high speed operation is possible. The major disadvantage for these networks is they are subject to blocking, which can be severe for indoor applications.

Our approach to deal with the broadcasting issue in networking for FSO communications is to use omnidirectional links [19]. They should provide reliable performance in short-range outdoor applications. Unlike indoor environments, this LOS approach will not be severely affected by blockage, since the blocking objects are usually mobile. The use of customized beam diverging optics in a laser transmitter front-end can achieve moderate distance (tens of meters) connectivity suitable for sensor networks applications. To achieve a hemisphere or full sphere coverage generally requires that these types of transceivers have multiple transmitters and receivers.

Omnidirectional FSO links do not offer the same channel security performance as directional ones. Their covertness resides mainly in their operation at unconventional wavelengths, since an interceptor would require narrow band filtered receivers to detect their emissions in the presence of ambient light. For example, systems operated at 1.55 μm, are not detected by standard CCD/MOS imaging or night vision technology based on silicon. Systems operated near 800 nm are invisible to the naked eye, and if transmitted powers are chosen appropriately will not be detectable in the presence of ambient light without relatively sophisticated detection techniques.

In this research, our goals are to present practical omnidirectional transceiver system design, to characterize omnidirectional link performance, and to explore related implementation issues.

1.7 Organization

The remainder of this dissertation is organized as follows: Chapter 2 reviews basic optical system and link design for FSO systems. The theoretical framework required for accessing FSO link performance is presented. Chapter 3 presents in depth the theoretical analysis and characterization of the time delayed diversity scheme under typical FSO communications scenarios. In Chapter 4, experimental investigations for time delayed diversity FSO system are described and the results are explained. The experiments were conducted under two difference turbulence conditions: laboratory convective turbulence and clear atmospheric turbulence. Chapter 5 describes the design, construction, and characterization of a prototype omnidirectional FSO system. The dissertation is concluded in Chapter 6, which summarizes the contributions of this work and suggests several possible directions for future work.

Chapter 2: Free Space Optical System Design and Link Analysis

2.1 Optical Sources and their Transmitted Fields

The key element in any optical communication system is an optical source that can easily be modulated. Such a source should produce energy concentrated in a narrow wavelength band, and should be capable of being modulated at very high rates. One of the primary sources of light in modern optical systems is the semiconductor laser. Their basic principles and characteristics, such as their output beam profile, will be important in assessing their performance when used in a free space optical (FSO) system.

2.1.1 Basic Characteristics of Semiconductor Lasers

A semiconductor laser consists of an active layer and surrounding *p*-type and *n*-type cladding regions, providing a *p*-*n* junction geometry. The emission is realized in the active layer having an energy gap E_g that corresponds to the desired emission wavelength l given by

$$l\left(mm\right)=\frac{1.240}{E_g\left(eV\right)}\,. \tag{2.1}$$

The semiconductor material needed for emission should have a direct bandgap, meaning that the conduction band lies directly above the valence band in momentum space. Therefore, carriers can efficiently recombine to emit photons, since the momentum is conserved. This makes the majority of semiconductor laser materials based on a combination of elements in the third group (such as Al, Ga, In) and the fifth group (such as N, P, As, Sb) of the Periodic Table; hence the emitted wavelength is typically in the infrared spectrum.

When forward bias is applied to the active layer, carrier density is increased. As the pumping is increased further, a population inversion between conduction and valence bands will result. This is the condition where the electron density in the conduction band exceeds local electron density of the valence band. In the population inversion condition, stimulated emission becomes greater than absorption, thus the active layer serves as an optical amplification medium, and the laser begins to oscillate. The feedback mechanism necessary for the laser oscillation is provided by two reflective facets at both ends of the active layer or laser cavity. In this process, there is noise component generated by the amplitude fluctuation of the signal light, called the relative intensity noise (RIN). Semiconductor lasers can produce high power levels, narrow linewidths (~1 nm), and low RIN (−160 to −150 dB/Hz).

The optical radiation within the resonance cavity sets up a pattern of electric and magnetic fields lines called the modes of the cavity, which can be described in terms of the longitudinal and transverse variations of the electromagnetic fields along the major axes of the cavity. Longitudinal modes are related to the length of the cavity and determine the principal structure of the frequency spectrum of the emitted radiation. Since the cavity length is much larger than emission wavelength, many longitudinal modes can exist. Transverse modes are associated with the electromagnetic field and beam profile in the direction perpendicular to the plane of the *p-n* junction, and determine the radiation pattern and the threshold current density.

For optical communication applications single mode lasers are preferred, which contain only single longitudinal and transverse modes. To accommodate this requirement, laser configurations having a built-in frequency selective reflector are developed. Two common types of such lasers are: distributed feedback (DFB) lasers and distributed Bragg reflector (DBR) lasers [20,21]. In DFB lasers, a Bragg grating formed along the cavity causes strong reflection at a certain wavelength, resulting in oscillation on a single mode with a narrower linewidth (< 0.1 nm). Therefore, no mode hoping occurs, so there is much less RIN. For the DBR lasers, the gratings are located at the ends of the active layer; hence no currents pass through the Bragg reflector regions. As a result, DBR lasers provide stable, tunable single mode operation while their other characteristics are similar to DFB lasers. Table 2.1 summarizes basic characteristics of the semiconductor lasers.

Table 2.1: Basic characteristics of laser diodes.

Laser Materials	III-V compounds
Emission Wavelength	800 - 1500 nm
Output Power	1 - 100 mW
Linewidth	0.1 - 5 nm
Modulation Bandwidths	Up to many GHz

2.1.2 Wave Propagation in Free Space

The transverse modes of a laser system take the form of narrow beams of light that propagate between the mirrors of the laser resonator and maintain a field distribution that remains distributed around and near the axis of the system. While there are many solutions to this problem, it turns out that the simplest solution is called a Gaussian beam, which is appropriate to the laser under ordinary conditions. These beams have a characteristic radial intensity profile that expands laterally as they propagate. Gaussian beams are special solutions to the electromagnetic wave equation, which are restricted under paraxial conditions.

The free space propagation of a single mode laser beam can be modeled as the lowest order Gaussian beam wave, also called a TEM$_{00}$ wave. Assuming the source is located at $z = 0$, the field distribution of this fundamental mode at $z = L$ is given by [22]

$$U(\mathbf{r}, L) = U_0 \frac{w_0}{w_L} \exp\left[- j(kL - \Phi) - r^2 \left(\frac{1}{w_L^2} + \frac{jk}{2R_L} \right) \right], \tag{2.2}$$

where r is the transverse distance from the beam center, w_0 is the minimum spot size, Φ is the phase shift, and $k = 2p/l$ is the wave number . The beam parameters, w_L and R_L, are the spot size and the radius of curvature of phase front at *L*, respectively. They are defined as

$$w_L^2 = w_0^2 \left[1 + \left(\frac{lL}{pw_0^2} \right)^2 \right], \tag{2.3}$$

and

$$R_L = L \left[1 + \left(\frac{pw_0^2}{lL} \right)^2 \right]. \tag{2.4}$$

Thus, the form of the fundamental Gaussian beam is uniquely determined once the minimum spot size and its location are specified.

The spot size is the transverse distance at which the field amplitude is down by a factor $1/e$ compared to its value on the axis. The minimum spot size is the beam spot size at the plane $z = 0$. From Eq. (2.3), it can be shown that w_L expands with distance L along the axis following a hyperbola that corresponds to the local direction of energy propagation. The angle between the asymptotes and the propagation axis is called beam divergence and is a measure of the angular beam spread. For an optical wave, the divergence is typically small and the half angle divergence q_B can be written as

$$q_B \approx \frac{l}{p\, w_0}. \tag{2.5}$$

The intensity of the optical wave is the squared magnitude of the field. Thus, the intensity distribution of the beam at $z = L$ can be written as

$$I(\mathbf{r}, L) = I_0 \frac{w_0^2}{w_L^2} \exp\left(-\frac{2r^2}{w_L^2} \right), \tag{2.6}$$

and Fig. 2.1 illustrates its expansion in free space propagation.

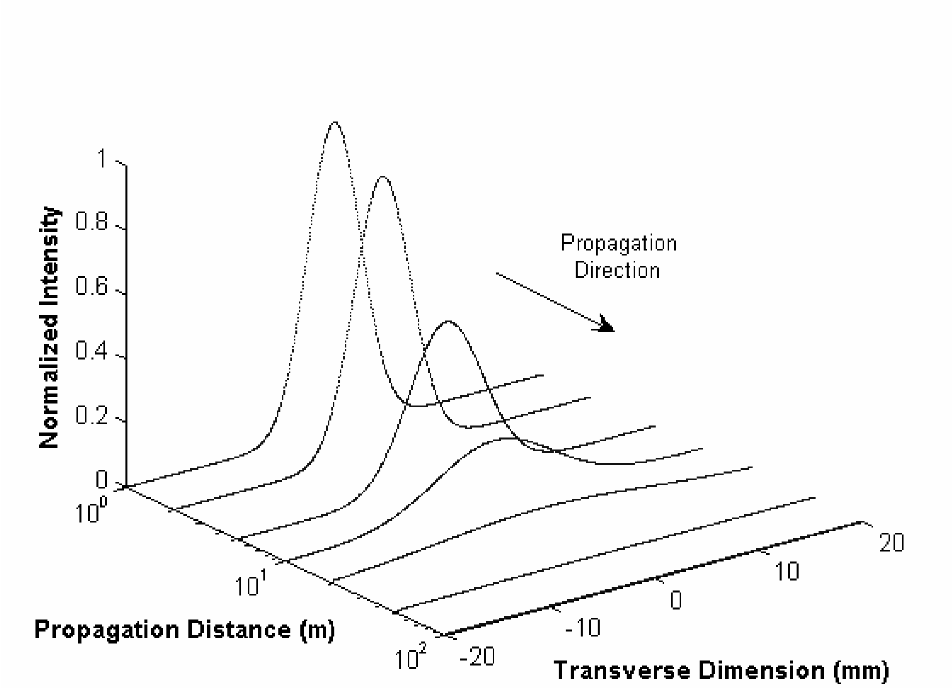

Figure 2.1: Intensity distribution profile in propagating Gaussian beam.

2.1.3 Beam Forming Optics

In long-range FSO communications, light fields from optical sources can be collected and refocused using beam forming optics, which will orient the light into particular directions. A combination of converging and diverging lenses placed at the source is used to produce a collimated beam. Fig. 2.2 shows a simple type of beam collimation commonly used in long-range links. For short-range links, in order to obtain omnidirectionality, the optical light needs to emerge over a wider angle, but at the expense of rapid beam expansion with distance. Both imaging and non-imaging omnidirectional optical designs will be discussed in more detail in Sec. 5.3.

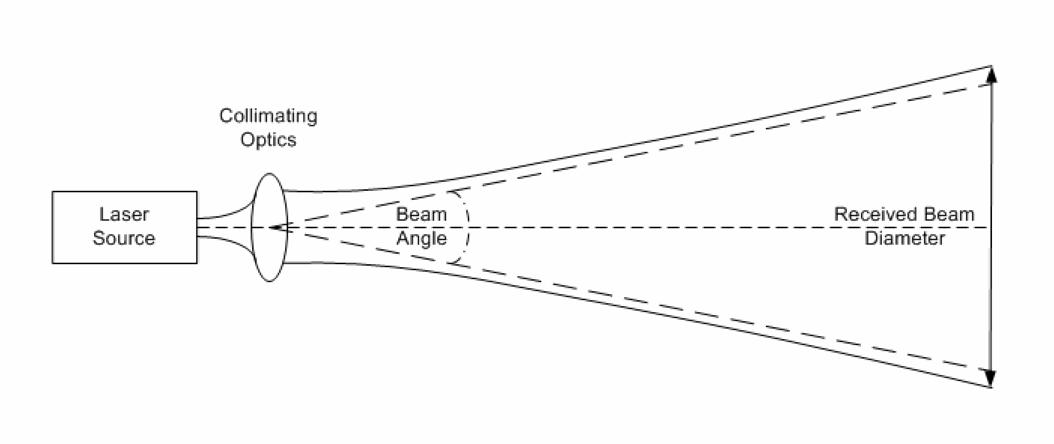

Figure 2.2: Example of beam collimation in long-range FSO links.

In an ideal collimation process, the converging lens focuses the light source to a point and the diverging lens expands it to a perfect beam. In practice, the source field is instead focused to a spot, and the expanded beam spreads during propagation with a planar beam diameter D_L of approximately

$$D_L = D_0\left[1+\left(\frac{2\theta_B L}{D_0}\right)^2\right]^{1/2}, \qquad (2.7)$$

where D_0 is the output lens diameter, L is the distance from the lens, and q_B is the transmitter beam angle, which for Gaussian beam is approximated by Eq. (2.5). At points in the near field, the emerging light is collimated with a diameter equals to the lens diameter, i.e. the light appears to uniformly exit over the entire lens. In the far field, the beam diameter expands with distance and appears as if the light is emerging from a single point. The expanding field far from the source is therefore confined to a two-dimensional solid angle Ω_B given by

$$\Omega_B = 2p\left[1 - \cos\left(q_B\right)\right] \approx pq_B^2 . \tag{2.8}$$

The advantage of beam forming can be emphasized by converting to an effective antenna gain parameter. From radio frequency (RF) theory, the effective antenna gain G_A can be written as

$$G_A = \frac{4p}{\Omega_B} \approx \frac{4}{q_B^2} , \tag{2.9}$$

which is inversely proportional to the beam angle. For optical wavelengths, the beam angle is typically on the order of a few mrad, which corresponds to an antenna gain of 65 dB. This is a significant advantage compared to RF transmitters with typical beams on the order of degrees, which gives an antenna gain of about 40 dB. However, it should be pointed out that with narrow beams, potential pointing and tracking problems are now generated, which are outside the scope of this dissertation.

2.2 Detection of Optical Radiation

When transmitted optical signals arrive at the receiver, they are converted to electronic signals by photodetectors. While there are many types of photodetectors in existence, photodiodes are used almost exclusively in optical communication applications because of their small size, suitable material, high sensitivity, and fast response time [23]. Two most commonly used photodiodes are the *pin* photodiode and the avalanche photodiode (APD) because they have good quantum efficiency and are made of semiconductors that are widely available commercially. For optimal design of the receiver system, it is important to understand the characteristics of these photodiodes and the noise associated with optical signal detection.

2.2.1 *pin* Photodiode

The *pin* photodiode consists of *p* and *n* regions separated by a very lightly *n*-doped intrinsic *i* region. In normal operation, a sufficient reverse bias voltage is applied across the device so that the intrinsic region is fully depleted. When an incident photon has energy greater than the bandgap energy of the material, the photon can give up its energy and excite an electron from the valence band to the conduction band. This generates free electron-hole pairs called photocarriers. The *pin* photodetector is designed so that these photocarriers are generated mainly in the depleted region, where most of the incident light is absorbed. The high electric-field present in the depletion region causes the photocarriers to separate and be collected across the reversed-bias junction. This produces a current flow in an external circuit, with one electron flowing for every photocarrier generated. The current flow is known as photocurrent.

The performance of a *pin* photodiode is often characterized by its responsivity $\Re$, given by

$$\Re = \frac{\eta q}{h\nu} = \frac{i_S}{P_O}\,, \tag{2.10}$$

where i_S is the average photocurrent generated by the optical power P_O incident on the photodiode. The quantum efficiency η is the number of the photocarriers generated per incident photon energy $h\nu$, and q is the electron charge. The parameter $\Re$ is quite useful since it specifies the photocurrent generated per unit optical power. The representative values for $\Re$ are 0.65 A/W for Si at 900 nm, 0.45 A/W for Ge at 1.3 µm, 0.9 A/W for InGaAs at 1.3 µm, and 1.0 A/W for InGaAs at 1.55 µm [23].

2.2.2 Avalanche Photodiode

The APD internally multiplies the primary signal photocurrent before it enters the input circuitry of the following amplifier. This increases the receiver sensitivity, since the photocurrent is multiplied before encountering the thermal noise associated with the receiver circuit. In this structure, photocarriers are created initially mostly in the lightly p-doped intrinsic layer called a π-layer, because the n^+-p junction is very thin. When there is sufficient voltage across the π-layer, the photocarriers can drift rapidly across it. Therefore, at the n^+-p junction near the positive electrode, a large field gradient is created and efficient avalanche multiplication occurs.

The performance of an APD is characterized by its multiplication factor M and is given by

$$M = \frac{i_M}{i_S}\,, \tag{2.11}$$

where i_M is the average value of total multiplied output current and i_S is the average un-multiplied photocurrent defined in Eq. (2.10). The avalanche mechanism is a statistical process, since not every photocarrier generated experiences the same multiplication. Thus, the measured value of M is expressed as an average quantity. It is also a function of the bias voltage. For practical applications, Si APD is operated typically with $M = 100$. The reverse bias voltage ranges from 10 to 100 V. If the bias voltage is too high, the photodiode may be in danger of creating self-sustaining avalanche current without photoexcitation, leading to extra noise from the photodiode.

Since an APD has much larger gain, it offers a better sensitivity than *pin* photodiode. The sensitivity increase may be on the order of 4 to 7 dB. However, they also have serious drawbacks, such as: a high operating voltage is required to provide a strong electric field, there is a strong temperature dependent of the multiplication factor, and there is additional noise due to saturation effects at high radiation levels [24]. Although these problems can be addressed and compensated, cost is increased. In contrast, a *pin* photodiode followed by an electronic amplifier could also provide good sensitivity margin with the expense of slower response time. For data transmission below one gigabit per second, the configuration of a *pin* photodetector and electronic amplifier may be advantageous over APD because of its low cost.

2.2.3 Noise in the Detection Process

The ability of a photodetector to detect an incoming signal is limited by intrinsic fluctuations or noise. If the signal power is less than the noise power, the signals will not be able to be distinguished clearly. The two most important sources of noise in the optical receiver are the shot noise resulting from the statistical nature of the photon-to-electron conversion process and the thermal noise associated with the amplifier circuitry. These sources of noise always accompany the optical signal. Another type of noise involved in the detection of optical radiation is dark current noise and background illumination noise, which may cause deleterious effects in FSO communication systems.

The principal noise associated with a photodetector is called quantum or shot noise. When an unmodulated lightwave is measured using a photodetector, two current components are obtained at the output. The first one is DC current, and the second one is the undesired shot noise signal. The shot noise arises from the statistical nature of the production and collection of discrete photoelectrons when an optical signal is incident on a photodetector. It has equal power density at all frequencies. If the electronic circuit after the photodetector only handles the frequency bandwidth Δf, the mean-square current amplitude of the shot noise $\left\langle i_{SN}^2 \right\rangle$ is given by

$$\left\langle i_{SN}^2 \right\rangle = 2 q i_S \Delta f \, , \tag{2.12}$$

where q is the magnitude of electron charge and i_S is the average photocurrent as in Eq. (2.10).

For an APD, in addition to the primary source of shot noise, there is a noise figure associated with the excess noise generated by the random avalanche process. This noise figure $F(M)$ is defined as the ratio of the actual noise generated in an avalanche photodiode to the noise that would exists if all carrier pairs were multiplied by exactly M and is given by

$$F(M) = \frac{\left\langle m^2 \right\rangle}{M^2} \, , \tag{2.13}$$

where $\left\langle m^2 \right\rangle$ is the mean square gain and can be approximated as M^{2+x} with x varying between 0 and 1 depending on the material and structure. Thus, the mean-square current amplitude of the shot noise for APD $\left\langle i_{SN}^2 \right\rangle_{APD}$ is given by

$$\left\langle i_{SN}^2 \right\rangle_{APD} = 2qi_S M^2 F(M)\Delta f = 2qi_M MF(M)\Delta f \ , \tag{2.14}$$

where i_S , i_M , and M are all defined as in Eq. (2.11).

Thermal noise, also called Johnson noise or Nyquist noise, is caused by the thermal agitation of charge carriers passing through a resistor. At temperatures above absolute zero, the thermal energy of the charge carriers in any resistor leads to fluctuations in local charge density. These fluctuating charges cause local voltage gradients that can derive a corresponding current into the rest of the circuit. If the circuits only handle a bandwidth of Δf and the resistance R is constant within this bandwidth, then the mean-square current amplitude of the Johnson noise $\left\langle i_{JN}^2 \right\rangle$ is given by

$$\left\langle i_{JN}^2 \right\rangle = \frac{4kT\Delta f}{R} \ , \tag{2.15}$$

where k is the Boltzmann's constant and T is the absolute temperature. One way to reduce this noise is by cooling the offending component to a lower temperature.

The dark current is the current that continues to flow through the bias circuit of the device even if no light is incident on the photodiode. It arises from electrons and/or holes that are thermally generated in the *p-n* junction of the photodiode. The dark current strongly depends on the type of semiconductor, operating temperature, and bias voltage; and is typically proportional to the term $\exp\left(-E_g / kT\right)$. Depending on the materials, their values range from 100 pA for Si up to 100 nA for Ge. Background illumination noise is caused by the light that is not part of the transmitted signals, such as ambient light. If the photodetector is not isolated from the background radiation, the appearance of this noise is inevitable. Due to the discreteness and randomness of both the dark current and background radiation, these noise sources are similar to the shot noise.

2.3 Link Physics of the Atmospheric Channels

The three primary atmospheric processes that affect optical wave propagation in free space are absorption, scattering, and refractive index fluctuations, or optical turbulence. Absorption and scattering by the constituent gases and particulates of the atmosphere give rise primarily to attenuation of the laser beam. Optical turbulence leads to receiver intensity fluctuations, beam broadening, beam wander, and beam break up; among other effects. Clearly, these deleterious effects have serious consequences in FSO communications.

2.3.1 Molecular Absorption and Scattering

Electromagnetic wave radiation is attenuated when propagating through the atmosphere due to absorption and scattering. Absorption occurs when a photon of radiation is absorbed by a gaseous molecule of the atmosphere, which converts the photon into kinetic energy or re-radiates it. Thus, absorption is a mechanism by which the atmosphere is heated. Atmospheric absorption is a strong function of wavelength, where the most severe absorption occurs at ultraviolet wavelengths (below 200 nm) due to O_2 and O_3 molecules, while there is very little absorption at visible wavelengths (400 to 700 nm).

Similar to absorption, light scattering is also strongly wavelength dependent. Particles that are small in comparison with the wavelength (i.e. air molecules, haze) will produce Rayleigh scattering, which has a symmetrical angular distribution. At ultraviolet and visible wavelengths Rayleigh scattering is quite pronounced, while scattering for wavelengths greater than 3 µm is basically nonexistent. Scattering by particles comparable in size to the wavelength is called Mie scattering, whereas scattering by particles much larger than the wavelengths (i.e. water droplets) can be described using geometrical optics. Unlike Rayleigh scattering, this type of scattering is more concentrated in the forward direction.

Molecular absorption and scattering effects are often combined and can be described by a single attenuation coefficient a, which can be written as

$$a(l) = a_A(l) + a_S(l), \tag{2.16}$$

where a_A and a_S are the coefficient parameters describing molecular absorption and scattering processes, respectively. The transmittance t of laser radiation that has propagated a distance L is related to the attenuation coefficient a as described by

$$t = \exp\left[-a(l)L\right], \tag{2.17}$$

where the product aL is called the optical depth. Both absorption and scattering are deterministic effects that are quite well known and can be predicted based on a variety of conditions.

2.3.2 Optical Turbulence

Other serious optical effects on a propagating laser beam are generally those caused by temperature variations manifested as refractive index fluctuations, commonly referred to as optical turbulence. In the visible and near infrared regions of spectrum, these index of refraction fluctuations are caused almost exclusively by temperature fluctuations; whereas in the far infrared region, humidity fluctuations may also contribute. Fluctuations in the index of refraction are related to corresponding temperature and pressure fluctuations. In particular, the refractive index of atmosphere *n* at a point **r** in space for optical wavelengths can be approximated according to

$$n(\mathbf{r}) \cong 1 + 79\times10^{-6}\,\frac{P(\mathbf{r})}{T(\mathbf{r})}, \tag{2.18}$$

where P is the pressure in millibars and T is the temperature in Kelvin.

Optical turbulence in the atmosphere can be characterized by three parameters: outer scale L_0, inner scale l_0, and the structure parameter of refractive index fluctuations C_n^2, which is a measure of the strength of the optical turbulence. An effective outer scale of turbulence is defined as the largest cell size at which turbulent energy is injected into a region. Near the ground, the outer scale is assumed to grow linearly with the height above ground. An effective inner scale of turbulence is identified with the smallest cell size before energy is dissipated into heat, and is usually on the order of millimeters (near the ground). The continuous distribution of cell sizes between the inner scale and outer scale forms the inertial subrange.

The refractive index structure parameter is considered the most critical parameter along the propagation path in characterizing the effects of atmospheric turbulence. It is usually defined as the proportionality constant in the refractive index structure function. Under statistically homogeneous and isotropic conditions, the refractive index structure function D_n in the inertial subrange exhibits the asymptotic behavior [25]

$$D_n(r) = \left\langle [n(0) - n(r)]^2 \right\rangle = C_n^2 r^{2/3}, \qquad (2.19)$$

where r is the separation between two points in space. The classic $2/3$ power law behavior was originally suggested by Kolmogorov on the basis of dimensional analysis. Values of C_n^2 for horizontal paths near the ground generally vary between 10^{-15} to 10^{-12} $\mathrm{m}^{-2/3}$, in which the latter is considered strong turbulence.

2.3.3 Spatial Power Spectrum Models

Under the assumption of a statistically homogeneous and isotropic atmosphere, the spatial power spectral density of refractive index fluctuations Φ_n is related to the structure function D_n by

$$D_n(r) = 8p \int_0^{\infty} k^2 \Phi_n(k) \left[1 - \frac{\sin(kr)}{kr} \right] dk \, . \qquad (2.20)$$

Based on the $2/3$ power law expression for the structure function in the inertial range given in Eq. (2.19), the associated three-dimensional power spectrum of refractive index fluctuations is defined by the classical Kolmogorov spectrum [25]

$$\Phi_n(k) = 0.033 C_n^2 k^{-11/3}, \; 1/L_0 \ll k \ll 1/l_0 \, , \qquad (2.21)$$

where k is the spatial wavenumber. Although this spectrum is theoretically valid only over the inertial range, it is often extended over all wavenumbers by assuming the inner scale is zero and outer scale is infinite. This spectrum is widely used in theoretical calculations, in part because of its relatively simple mathematical form.

Other spectral models have been proposed when inner scale or outer scale effects cannot be ignored. The extension of the Kolmogorov spectrum into the dissipation range ($k > 1/l_0$) requires truncation of the spectrum at high wavenumbers. This can be achieved using a Gaussian function, which leads to the Tatarskii spectrum [26]

$$\Phi_n(k) = 0.033 C_n^2 k^{-11/3} \exp\left(-\frac{k^2}{k_m^2}\right), \; k \gg 1/L_0 , \qquad (2.22)$$

where $k_m = 5.92/l_0$. If the Tatarskii spectrum is modified so it is finite and isotropic for wavenumbers $k < 1/L_0$, the turbulence can then be modeled as if it is statistically homogeneous and isotropic over all wavenumbers. A spectral model that is often used in this case is the Von Kármán spectrum

$$\Phi_n(k) = 0.033 C_n^2 \frac{\exp\left(-k^2/k_m^2\right)}{\left(k^2 + k_0^2\right)^{11/6}}, \; 0 \le k < \infty , \qquad (2.23)$$

where $k_0 = 1/L_0$. Fig. 2.3 illustrates these three spectrum models over a range of wavenumbers computed for inner and outer scales of 10 mm and 10 m, respectively.

2.4 Signal and Noise Level at Free Space Optical Receivers

Optical receivers are broadly divided into two basic types: direct detection receivers, which detect only the amplitude of the wave; and coherent detection receivers, which detect the wave itself (i.e. both amplitude and phase). To compare both receiver types, the signal and noise levels in both systems are calculated. For this comparison, an intensity modulation, with intensity referring to optical power and modulation referring to the electro-optical conversion process, is assumed.

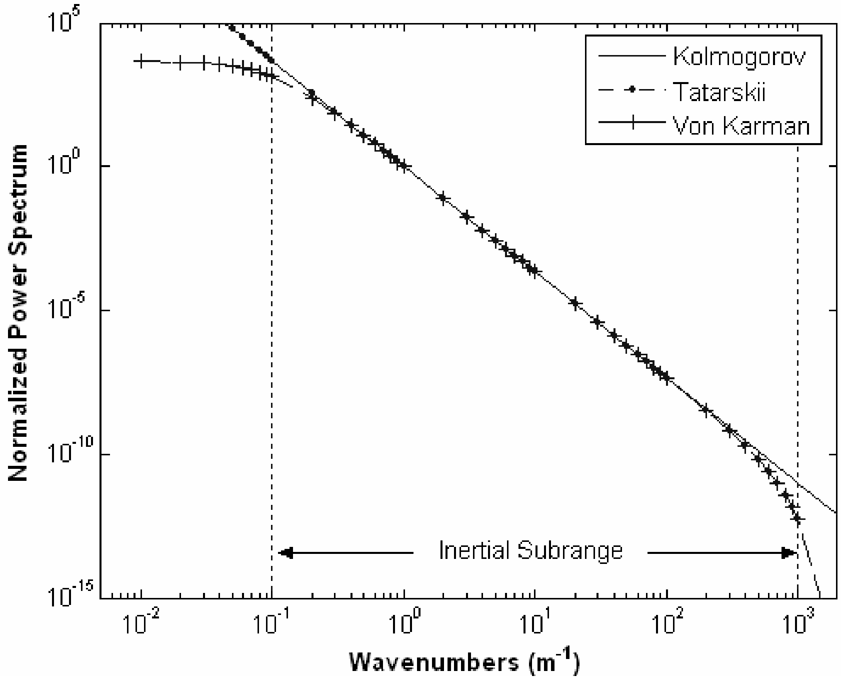

Figure 2.3: Spatial power spectrums for Kolmogorov, Tatarskii, and Von Kármán, from Eqs. (2.21) – (2.23), calculated for $l_0 = 10$ mm and $L_0 = 10$ m.

2.4.1 Optical Intensity Modulation Systems

Compared to a conventional wireless RF channel, the first important difference in an intensity-modulated channel is that the quantity that carries the information cannot be negative (i.e. unipolar waveforms). The second difference is the definition of power consumption of the system. In an intensity modulation system, the power consumption depends on the average optical power $\langle P_O \rangle$, which according to Eq. (2.10) is proportional to the average signal current $\langle i_S \rangle$. In the case of RF system, the power consumption depends on the average electrical power and is usually assumed to be proportional to the square of signal current $\langle i_S^2 \rangle$. Therefore, schemes that are power efficient in RF systems need not be so in optical intensity modulation systems.

Bandpass modulation schemes that are used in RF systems have to be provided with an offset before they can be transmitted by optical intensity modulation systems. Although this offset does not carry any information, it does determine the average intensity and thus the power consumption. Therefore, the power efficiency of bandpass schemes is worse than the power efficiency of baseband schemes, which leads to the motivation for the use of baseband modulation schemes in optical wireless systems [24,27]. The properties of baseband modulation schemes commonly used in optical wireless systems, such as on-off keying (OOK) and pulse position modulation (PPM), will be discussed further in Sec. 2.5.

2.4.2 Non-coherent (Direct) Detection Model

The simplest implementation of an optical receiver is a power-detecting receiver, also called a non-coherent or direct detection receiver. Because it responds only to the instantaneous power of the collected field, a direct detection receiver does not use the transverse spatial coherence of the transmitted optical field. In a typical model of a direct detecting FSO system, the information is intensity modulated onto an optical source and transmitted through an atmospheric channel to the receiver. The receiving lens collects a portion of the received optical field and focuses it onto a photodetector.

The optical field is always photodetected in the presence of various noise sources present in the optical detection process. In FSO systems, background radiation such as natural light, is also collected along with the transmitted optical field and is usually treated as an additive noise to the desired signal field. Another source of noise is the shot noise originating in the photodetection process and dark current at the photodetector itself. Lastly, the Johnson noise is also present in the electronic circuitry following the photodetection process. Fig. 2.4 shows the typical model for a direct detection system.

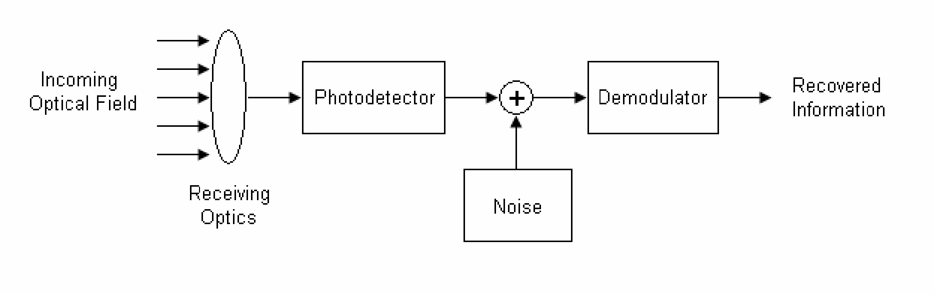

Figure 2.4: Block diagram of direct detection optical receiver.

Recall that free space propagation of a laser beam can be modeled using a Gaussian beam with intensity profile described in Eq. (2.6). If the receiver has an aperture diameter *D*, then the received signal power P_R at the photodetector is

$$P_R = \int_0^{2\pi} \int_0^{\infty} I(\mathbf{r}, L)\, r dr d\theta \cong \frac{\pi D^2}{8} I(0, L). \tag{2.24}$$

Assuming a *pin* photodetector is used, the output signal current induced by the incident optical wave is

$$i_S = \Re P_R, \tag{2.25}$$

where $\Re$ is the photodetector responsivity. Let the detector be followed by a filter of bandwidth Δf , where the bandwidth is chosen to match the frequency spread of the incoming signal envelope. If all noise sources have zero mean and are statistically independent of each other, then the total noise power in the detector current s_N^2 is defined by

$$s_N^2 = 2q\left(i_S + i_D + i_B\right)\Delta f + \frac{4kT\Delta f}{R}, \tag{2.26}$$

where i_D and i_B are the photodetector dark current and background illumination induced currents.

2.4.3 Signal-to-Noise Ratio in Direct Detection

To quantify the performance of a direct detection receiver, the output signal-to-noise ratio (SNR) is defined as the ratio of the detector signal power to the total noise power. In practice, the received power is typically large enough such that the signal current dominates over the dark current and background illumination noise. Therefore, the remaining noise terms are typically caused by shot noise and Johnson noise, which gives a SNR expression for direct detection $\Gamma_{0,DD}$ as

$$\Gamma_{0,DD} = \frac{i_S^2}{s_N^2} = \frac{i_S^2}{2qi_S\Delta f + 4kT\Delta f/R}. \tag{2.27}$$

If the shot noise dominates over the Johnson noise, then the resulting shot noise limited SNR $\Gamma_{0,DD-SNL}$ is given by

$$\Gamma_{0,DD-SNL} = \frac{i_S}{2q\Delta f} = \frac{hP_R}{2hn\Delta f}. \tag{2.28}$$

Eq. (2.28) represents the quantum limit performance that can be achieved using direct detection system.

Fig. 2.5 illustrates the computed SNR performance of direct detection system for link distances of 100 m and 1 km. The transmitted laser power varies from 1 to 100 mW. The receiver uses a *pin* photodiode with responsivity of 0.45 A/W, which corresponds to approximately 70% efficiency at 785 nm wavelength. The transmitted beam has 2 mrad beam divergence and the receiver aperture has 100 mm diameter. The bandwidth of the receiver circuits is set at 1 GHz, which is quite common in FSO communication system. The shot noise limited SNR performance can be approached when the transmitted power is made high. For links beyond 1 km, the use of laser power higher than 100 mW is required to approach this ideal performance.

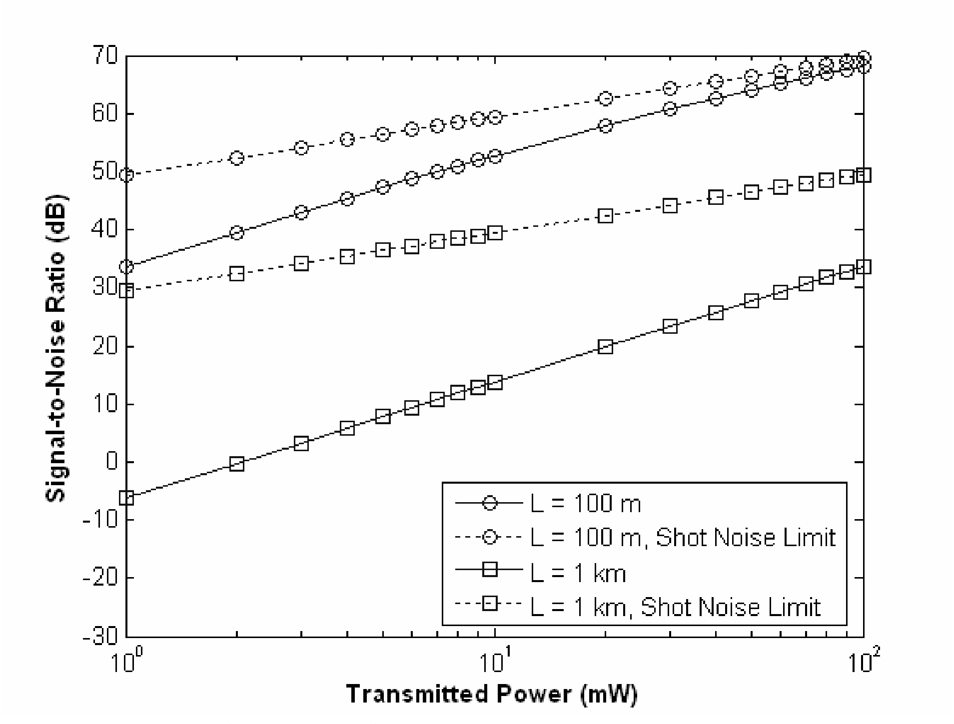

Figure 2.5: SNR performance of direct detection FSO system with $q_B = 2$ mrad, $\Re = 0.45$ A/W, $D = 100$ mm, and $\Delta f = 1$ GHz; calculated for 100 m and 1 km links.

2.4.4 Coherent (Heterodyne) Detection Model

In direct detection receivers, the quantum noise limit set by shot noise can be achieved with sufficiently strong received signal fields or a high sensitivity photodetector. If they are not available, it is possible to achieve the quantum limit of detection by the use of coherent detection or heterodyning. In this scheme, the detector is illuminated simultaneously by the signal light and a second source of light called the local oscillator (LO), which must be phase coherent with the signal. The objective of this mixing process is to convert the weak incoming signal to an intermediate frequency (IF) in the microwave frequency range for improved detection and processing. The schematic way in which coherent detection is carried out is shown in Fig. 2.6.

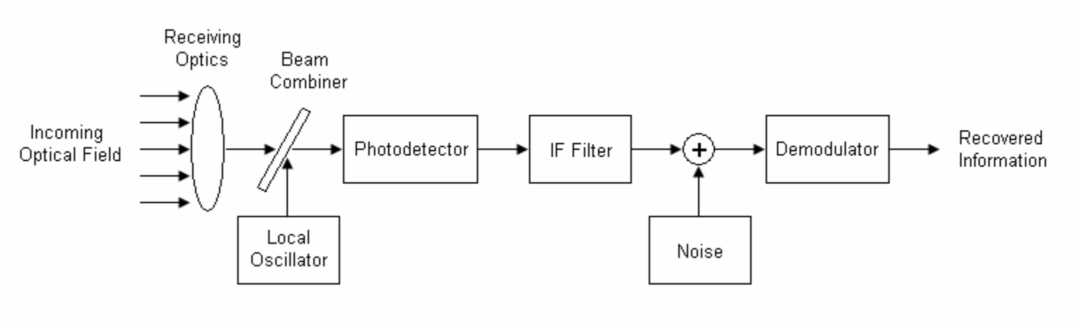

Figure 2.6: Block diagram of coherent detection optical receiver.

The complete expression for the transmitted optical signal field U_S at distance L can be written as

$$\begin{aligned} U_S(\mathbf{r},L,t) &= U_0 \frac{w_0}{w_L} \exp\left[-jkL - r^2\left(\frac{1}{w_L^2} + \frac{jk}{2R_L}\right)\right] \exp(jw_S t), \\ &= U_S(\mathbf{r}) \exp[j(w_S t - kL)] \end{aligned} \tag{2.29}$$

where w_S is the angular frequency of the optical signal. Similarly the expression for the LO field U_{LO} is

$$U_{LO}(\mathbf{r}, L, t) = U_{LO}(\mathbf{r}) \exp\left[j(w_{LO} t - j_{LO})\right], \tag{2.30}$$

where w_{LO} and j_{LO} are the angular frequency and longitudinal phase of the LO. Thus, the combined intensity incident on the photodetector can be described as

$$\begin{aligned} I(\mathbf{r}, L, t) &= \left| U_S(\mathbf{r}, L, t) + U_{LO}(\mathbf{r}, L, t)\right|^2 \\ &= \left| U_S(\mathbf{r}, L, t)\right|^2 + \left| U_{LO}(\mathbf{r}, L, t)\right|^2 \qquad , \\ &\quad + 2\,\mathrm{Re}\left\{ U_S(\mathbf{r}) U_{LO}^*(\mathbf{r}) \exp\left[j(w_{IF} t - j_{IF})\right]\right\} \end{aligned} \tag{2.31}$$

where $w_{IF} = w_S - w_{LO}$ is the IF angular frequency, $j_{IF} = kL - j_{LO}$ is the IF phase, and the first two terms correspond to constant intensity from the signal and LO independently.

Using the relations given by Eqs. (2.24) and (2.25), the detector current is related to the combined intensity according to

$$\begin{aligned} i(t) &= \frac{pD^2}{8} \Re\left[I_S(0, L) + I_{LO}(0, L) + 2\sqrt{I_S(0, L) I_{LO}(0, L)} \cos(w_{IF} t - j_{IF})\right] \\ &= i_S + i_{LO} + 2\sqrt{i_S i_{LO}} \cos(w_{IF} t - j_{IF}) \end{aligned} , \tag{2.32}$$

where i_S and i_{LO} are the direct detected signal and LO currents contributing in the shot noise generation. By eliminating the direct detection terms through bandpass filtering at the IF, the remaining current i_{IF} is

$$i_{IF}(t) = 2\sqrt{i_S i_{LO}} \cos(w_{IF} t - j_{IF}), \tag{2.33}$$

which contains the desired information in its envelope. The total noise power generated at the detector s_N^2 is now given by

$$s_N^2 = 2q\left(i_S + i_{LO} + i_D + i_B\right)\Delta f + \frac{4kT\Delta f}{R}\,. \tag{2.34}$$

2.4.5 Signal-to-Noise Ratio in Coherent Detection

The coherent detection scheme can be used when the incoming optical signal is very weak. Thus, the dark current and background illumination noise cannot be ignored when assessing the SNR performance. In addition, the signal power is obtained from the mean-squared value of the IF current. Thus, the SNR of coherent detection $\Gamma_{0,CD}$ is written as

$$\Gamma_{0,CD} = \frac{\left\langle i_{IF}^2 \right\rangle}{s_N^2} = \frac{2 i_S i_{LO}}{2q\left(i_S + i_{LO} + i_D + i_B\right)\Delta f + 4kT\Delta f / R}\,. \tag{2.35}$$

However, with a sufficiently powerful LO, its shot noise dominates and the other noise can be neglected. In this case, the SNR is again reduced to shot noise limited SNR $\Gamma_{0,CD-SNL}$ given by

$$\Gamma_{0,CD-SNL} = \frac{i_S}{q\Delta f} = \frac{hP_R}{hn\Delta f}\,. \tag{2.36}$$

The SNR performance of coherent detection system is calculated with the same parameters used in direct detection case and illustrated in Fig. 2.7, where LO power of 1 mW is used. The scheme starts to lose its advantage when the received power approaches LO power. At this level, the SNR performance is limited by LO power.

Comparison between Eqs. (2.28) and (2.36) demonstrates that ideal coherent detection has quantum limited performance twice that of direct detection. However, to make such a comparison, one must assume that it is possible to use the same parameters in working with both schemes. Furthermore, for optimum performance, not only must signal and LO be phase coherent, but their phase fronts and polarization states must be matched at the detector surface. In FSO receiver systems, these requirements are very difficult to realize. For example, under atmospheric turbulence channels, the phase front, the spot size, and the spatial coherency of the optical signal are randomly distorted; and the performance is limited to the coherence area of the collected random field [28].

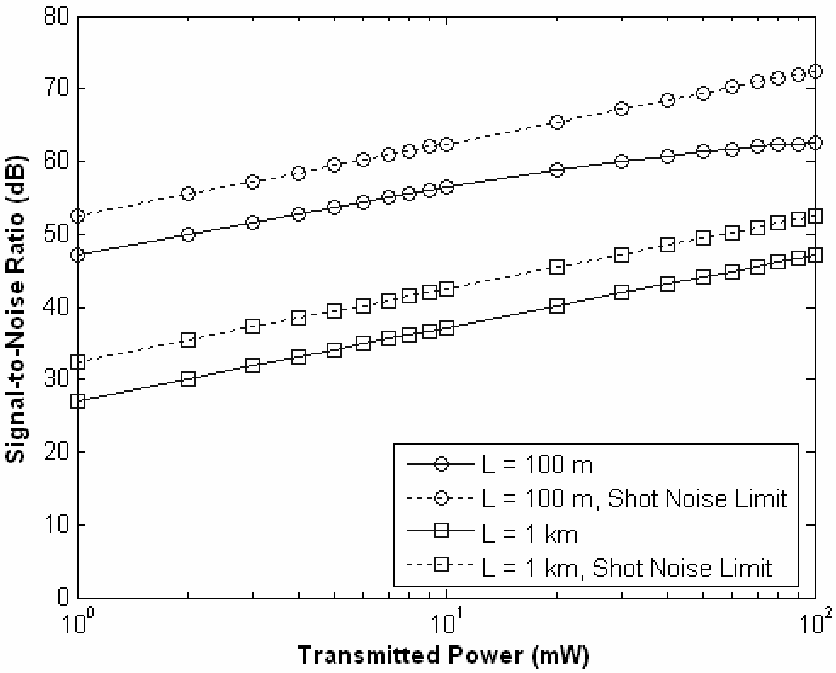

Figure 2.7: SNR performance of coherent detection FSO system with $P_{LO} = 1$ mW, $q_B = 2$ mrad, $\Re = 0.45$ A/W, $D = 100$ mm, and $\Delta f = 1$ GHz; calculated for 100 m and 1 km links.

2.5 Modulation Schemes in Optical Wireless Communications

In optical wireless systems, the intensity of an optical source is modulated to transmit signals. For digital data transmission, there is no practical alternative to digital modulation since it provides source coding (data compression), channel coding (error detection/correction), and easy multiplexing of multiple information streams [29]. The transmission of the digital data can be done on a bit-by-bit basis (binary encoding) or on a bit-word basis (block encoding). Several baseband modulation schemes for binary and block encoding are discussed; and their performance in terms of power and bandwidth efficiency is compared.

2.5.1 On-Off Keying

The simplest type of binary modulation scheme is OOK. In an active high OOK encoding, a ‘one’ is coded as a pulse, while a ‘zero’ is coded as no pulse or off field. To restrict the complexity of the modulator, the pulse shape is chosen to be rectangular. The bit rate is denoted as $R_b = 1/T_b$, where T_b is the bit duration; and is directly related to the rate at which the source can be switched on and off. The normalized transmit pulse shape for OOK is given by

$$p(t) = \begin{cases} 1 & \text{, for } t \in [0, T_b) \\ 0 & \text{, elsewhere} \end{cases}. \tag{2.37}$$

In the demodulator, the received pulse is integrated over one bit period, then sampled and compared to a threshold to decide a ‘one’ or ‘zero’ bit. This is called the maximum likelihood receiver, which minimizes the bit error rate (BER). Because of detector noise, errors may be made in determining the actual symbols transmitted. In OOK transmission, the random noise can be approximated as Gaussian distribution. Assuming both symbol have identical noise variance and are equally likely to be transmitted, the threshold level is set halfway between the symbols currents. Thus, the BER can be calculated as in [29,30]

$$\Pr(e)_{OOK} = \frac{1}{2}\operatorname{erfc}\left(\frac{i_S}{2\sqrt{2}s_N}\right) = \frac{1}{2}\operatorname{erfc}\left(\frac{1}{2\sqrt{2}}\sqrt{\Gamma_0}\right), \tag{2.38}$$

where $\operatorname{erfc}(x) = (2p)^{-1/2}\int_x^{\infty}\exp\left(-t^2\right)dt$ and Γ_0 is the SNR for direct detection receiver defined in Eq. (2.27).

Another important parameter that needs to be considered in any modulation scheme is the bandwidth requirement. The bandwidth is estimated by the first zeros in the spectral density of the signal. The spectral density is given by the Fourier transform of the autocorrelation function. For uncorrelated input bits, the spectrum of OOK signals is given by [30]

$$S(f)_{OOK} = \frac{i_S^2}{4R_b}\operatorname{sinc}^2\left(\frac{pf}{R_b}\right)\left[1 + R_b\sum_{k=-\infty}^{\infty}d\left(f - kR_b\right)\right], \tag{2.39}$$

where $\operatorname{sinc}(x) = \sin(x)/x$ and $d(x)$ is the Dirac delta function. Because the duration of the pulses is finite, the spectrum extends to infinity. The impulse at zero frequency accounts for the DC component that is present in any unipolar signal and determines the power consumption.

There is a variation of OOK, in which the pulse shape is high for only a fraction of bit duration dT_b with $0 \le d < 1$. The benefit obtained from this scheme is a reduction in transmitted power. However, as d decreases, the bandwidth requirement grows faster than the decrease in power requirement. Thus, this type of OOK is inferior to PPM, which offers less bandwidth to achieve a given reduction in power. For $d = 0.5$, this scheme is commonly called return-to-zero (RZ) OOK. In RZ-OOK, it is intuitive to show that the power requirement is reduced to half of the regular non-return-to-zero (NRZ) OOK discussed earlier, with the expense of doubling the bandwidth.

2.5.2 Manchester Encoded Signal

The basic disadvantage of OOK signaling is that key receiver parameter values, such as power levels, must be known to optimally set the threshold. A pulse format that avoids this difficulty uses pulse-to-pulse comparison for decoding. One way to do this in binary encoding is called Manchester coding, where a ‘one’ is signified when the optical signal is on during the first half of the symbol interval, and a ‘zero’ is signified when the optical signal is on during the second half of the symbol interval. The transmit pulse shape p_m for $m = \{0, 1\}$ can be written as

$$p_m(t) = \begin{cases} 1 & \text{, for } t \in [0, T_b/2) \text{ and } m = 1 \\ 1 & \text{, for } t \in [T_b/2, T) \text{ and } m = 0 \\ 0 & \text{, elsewhere} \end{cases} . \tag{2.40}$$

The demodulator separately integrates the detector output over the two half bit intervals and compares them for bit decoding. The bit is decoded according to which integration produces the higher value, and no threshold need be selected. The system still uses pulse signaling, but the pulse time is one half the bit time, and this results in higher required bandwidths. The BER is now the probability that the bit half interval containing the pulse does not produce the higher value. Since the Manchester signaling is identical to 2-PPM, all the results for PPM can be applied directly in analyzing this scheme.

2.5.3 Pulse Position Modulation

In block encoding, bits are transmitted in blocks instead of one at a time. Optical block encoding is achieved by converting each word of *l* bits into one of $L = 2^l$ optical fields for transmission. One of the most commonly used optical block encoding schemes is PPM, where an input word is converted into the position of a rectangular pulse within a frame. The frame with duration T_f is divided into *L* slots and only one of these slots contains a pulse. This scheme can also be denoted as *L*-PPM, in order to emphasize the choice of *L*. The transmit pulse shape for *L*-PPM is given by

$$p_m(t) = \begin{cases} 1 & , \text{ for } t \in \left[(m-1)T_f / L, mT_f / L\right) \\ 0 & , \text{ elsewhere} \end{cases}, \tag{2.41}$$

where $m \in \{1,\ 2,\ ...,\ L\}$. Since L possible pulse positions code for $\log_2 L$ bits of information, the bit rate is $R_b = \log_2 L / T_f$.

The optimum *L*-PPM receiver consists of a filter bank, each integrating the photocurrent in one pulse interval. The demodulated pulse is taken to originate from the slot in which the most current level was found. If the demodulated pulse position is the correct pulse position, $\log_2 L$ bits are decoded correctly. Otherwise, we assume that all $L-1$ wrong positions are equally likely to occur. Therefore bit errors usually occur in groups. For Gaussian noise, the BER can be written as [27,29]

$$\Pr(e)_{PPM} \approx \frac{1}{2}\text{erfc}\left(\frac{1}{2\sqrt{2}}\sqrt{\frac{L}{2}\log_2 L\Gamma_0}\right). \tag{2.42}$$

Substituting $L = 2$ yields the BER for Manchester signals, which is identical to the BER of OOK modulation. The expression for the PPM spectrum, assuming random input bits, is given by [24,31]

$$S(f)_{PPM} = \frac{i_S^2}{4}\left[T_f \operatorname{sinc}^2\left(\frac{pfT_f}{L}\right) - T_f \operatorname{sinc}^2\left(pfT_f\right) + d(f)\right]. \tag{2.43}$$

2.5.4 Comparison of Modulation Schemes

In order to compare different modulation schemes, the power and bandwidth efficiency, defined as the required power and bandwidth at a desired transmission speed and BER quality, were calculated. Power efficiency can readily be derived from the BER expressions. Fig. 2.8 shows the BER performance of OOK, for both NRZ and RZ, and *L*-PPM for $L = 2$, 4, and 8. It is fairly obvious that 8-PPM has the best BER performance, and hence is the most power efficient scheme. To achieve a given BER value p_e, the power requirement in OOK and *L*-PPM scheme can be written as

$$P_{OOK} = 2\sqrt{2}\,\frac{s_N}{\Re}\operatorname{erfc}^{-1}\left(2p_e\right), \tag{2.44}$$

and

$$P_{PPM} = 2\sqrt{2}\,\frac{s_N}{\Re}\left(\frac{L}{2}\log_2 L\right)^{-1/2}\operatorname{erfc}^{-1}\left(2p_e\right) = \frac{P_{OOK}}{\sqrt{\frac{L}{2}\log_2 L}}. \tag{2.45}$$

Thus, it is evident that *L*-PPM requires a factor of $\sqrt{(L/2)\log_2 L}$ less power than OOK to obtain a particular BER performance.

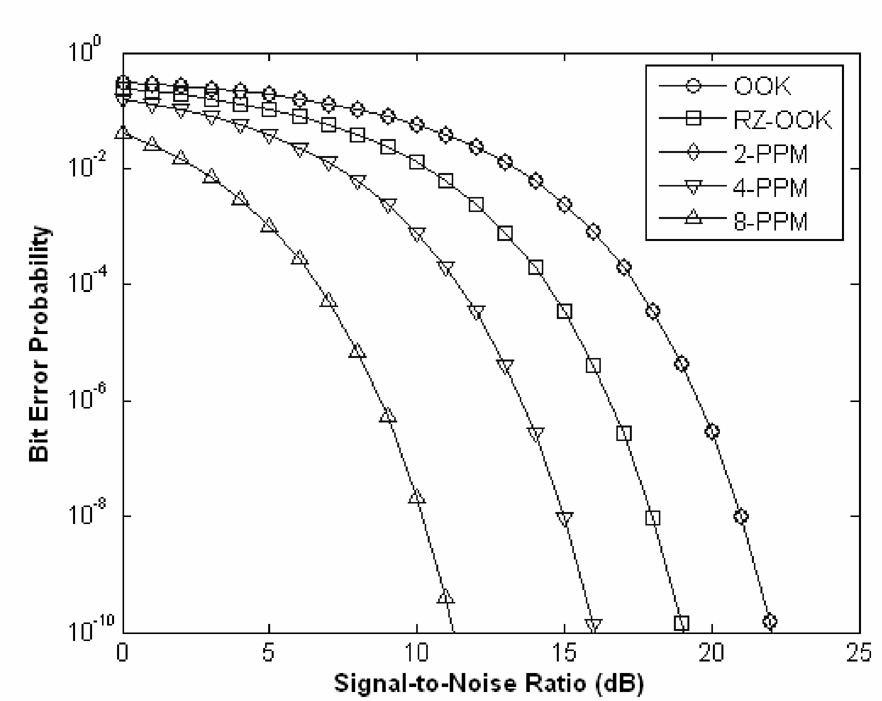

Figure 2.8: BER performance for OOK (NRZ and RZ), from Eq. (2.38), and *L*-PPM ($L = 2$, 4, and 8), from Eq. (2.42).

Another important measure of performance is the bandwidth efficiency. The bandwidth required for modulation can be estimated from the first zero of the transmitted signals power spectrum. Fig. 2.9 illustrates the spectral density envelope (without the Dirac impulses) of the transmitted signals for OOK and *L*-PPM. Note that only positive frequency is shown and the frequency is normalized to the bit rate R_b. The bandwidth efficiency is defined as the ratio between bit rate and required bandwidth (in bps/Hz). The required bandwidth is $B_{req} = R_b$ for OOK and $B_{req} = LR_b / \log_2 L$ for *L*-PPM. Thus, the bandwidth efficiency of *L*-PPM can be shown to be at least 1.9 times worse than OOK. To conclude, the comparison results are also summarized in Table 2.2.

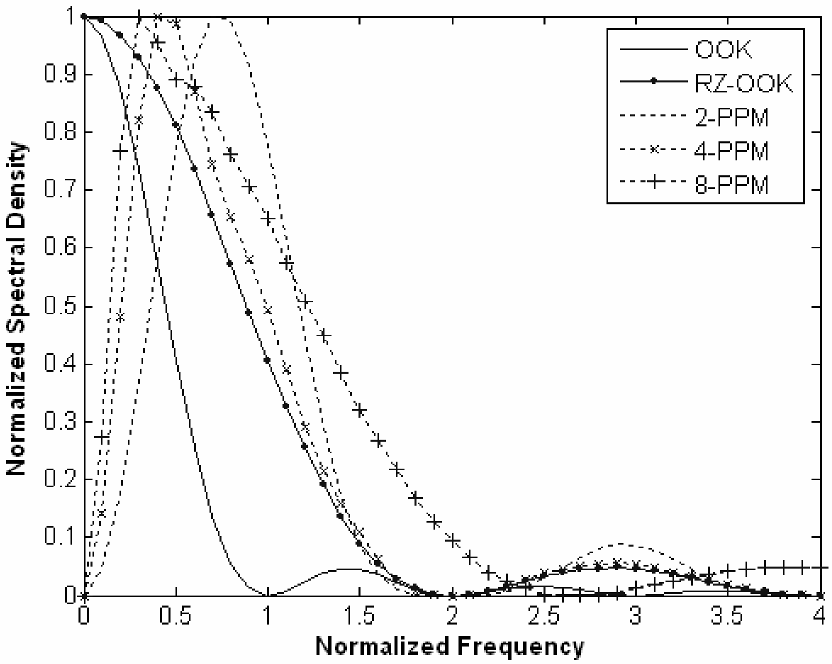

Figure 2.9: Power spectrum of the transmitted signals for OOK (NRZ and RZ), from Eq. (2.39), and L-PPM ($L = 2$, 4, and 8), from Eq. (2.43).

Table 2.2: Comparison of baseband intensity modulation techniques.

Modulation Scheme	Optical Power (dB)	Bandwidth Requirement
OOK	P_0	R_b
RZ-OOK	$P_0 - 3$	$2R_b$
Manchester Signaling	P_0	$2R_b$
L-PPM	$P_0 - 5\log_{10}\left[(L/2)\log_2 L\right]$	$LR_b/\log_2 L$

2.5.5 Effects of Timing Error on Performance

All the modulation schemes previously discussed require accurate pulse or slot integrations for ideal decoding. These integrations must be clocked by auxiliary timing circuits that provide the start and stop markers for the integrators, so that the integration variables are produced only over the exact slot times. If the timing is not accurate, the integrations occur over offset intervals, leading to false integration values that can degrade the decoding performance. In OOK system, the timing errors essentially cause additional variations in signal current, which can be viewed as additional noise source, hence always degrade the performance. Thus, they must be maintained to a small fraction of the bit time for adequate decoding.

In a PPM based system, the decoding process does not perform a threshold test, but rather an integrator comparison test. Timing offsets cause loss in pulse energy in the correct interval, and consequently a build-up of energy in the incorrect interval. This causes relatively faster decrease in performance as the offset is increased relative to the pulse time. For Manchester signals, since the slot interval is only half the bit interval, they are more susceptible to timing errors than the OOK system. Furthermore, the slot timing capability places a lower limit on the slot times that can be used in PPM systems, limiting their advantage over OOK systems.

2.6 Summary

In this chapter, the characteristics and properties of several important design parameters in FSO communication systems are discussed. A semiconductor laser or laser diode is the preferable type of optical source used in transmitter systems because of its fast modulation capability, narrow linewidth, moderately high power, and small production cost. For single mode laser diodes, the beam propagation in free space can be correctly modeled as a Gaussian beam. This model predicts the divergence of the beam as it propagates away from the source, decreasing the received optical power by a receiver system. This free space loss in FSO system may be compensated by beam forming optics, which provides directivity and gain similar to antennas in RF system.

At the receiver system, photodiodes are used almost exclusively in the photodetection process because they have high sensitivity and fast response time. For FSO communications, when the transmission rate is below one gigabit per second, the use of *pin* photodiodes in combination with electronic post-amplifiers is preferable to the use of APDs. The presence of noise limits the ability of a receiver to detect an incoming signal, which is typically characterized by the SNR. The two most important noise sources typically used in assessing the SNR of FSO systems are the shot noise and the thermal noise. The SNR is also affected by the degradation of the optical signal traveling through the atmospheric channel. In addition to free space loss, the atmosphere also introduces attenuation caused by either molecular absorption or scattering, and fading caused by optical turbulence.

Although an ideal coherent detection receiver outperforms direct detection receiver, its implementation in FSO communication systems is far from routine. The primary reason being the difficulty in maintaining the coherency between the signal and LO fields. Atmospheric turbulence causes the received signal field to experience random amplitude and phase fluctuations, which may result in random distortion of phase front and loss of spatial coherency. Signal transmission in optical wireless systems is generally realized using an intensity modulation technique. For FSO systems, although the power efficiency is inferior to PPM, OOK encoding is more commonly used due to its efficient bandwidth usage and robustness to timing errors. Therefore, in this research work, FSO systems are designed using intensity modulation/direct detection (IM/DD) with an OOK technique.

Chapter 3: Time Delayed Diversity to Mitigate Atmospheric Induced Fading

3.1 Optical Wave Propagation in Atmospheric Turbulence

Theoretical studies of optical wave propagation are traditionally classified as belonging to either weak or strong fluctuations theories. For weak intensity fluctuations, the most widely used analysis method is the classical Rytov approximation [26]. Its most useful results for free space optical (FSO) performance analysis are the expressions for the mean and covariance functions of received intensity fluctuations. The presence of optical turbulence will always degrade the performance of FSO system because of the randomness of the received signal. To evaluate this performance mathematically, distribution models for intensity fluctuations are required.

3.1.1 Rytov Approximation

One way to characterize the strength of the turbulence fluctuations is by examining the Rytov variance σ_R^2 for a plane wave, which is defined by

$$\sigma_R^2 = 1.23 C_n^2 k^{7/6} L^{11/6}, \tag{3.1}$$

where C_n^2 is the refractive index structure parameter described in Sec. 2.3.2. The Rytov variance physically represents the intensity fluctuations induced by atmospheric turbulence. In terms of the Rytov variance, the intensity fluctuations are called “weak” if $s_R^2 < 0.3$, and “strong” if $s_R^2 > 1$. Fig. 3.1 illustrates example of Rytov variances for typical C_n^2 values range from 10^{-14} to 10^{-12} m$^{-2/3}$ at propagation distance up to 1 km.

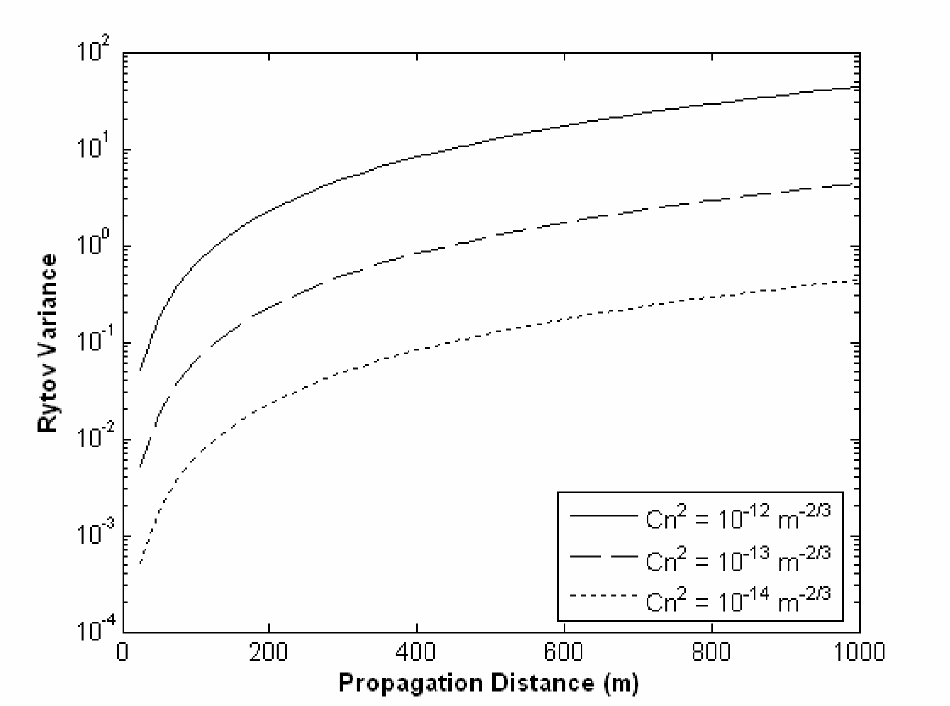

Figure 3.1: Rytov variance calculated for atmospheric turbulence with C_n^2 value ranges from 10^{-14} to 10^{-12} m$^{-2/3}$ and $l = 785$ nm.

From Maxwell’s equations, an optical field **U** of a propagating monochromatic electromagnetic wave at any point **R** can be described by

$$\nabla^2 \mathbf{U}(\mathbf{R}) + k^2 n^2(\mathbf{R}) \mathbf{U}(\mathbf{R}) + 2\nabla[\mathbf{U}(\mathbf{R}) \cdot \nabla \log n(\mathbf{R})] = 0, \tag{3.2}$$

where *n* is the random index of refraction. For optical wavelengths, the last term in Eq. (3.2), which is related to polarization effects, is usually negligible. This leads to the reduced wave equation

$$\nabla^2 U(\mathbf{R}) + k^2 n^2(\mathbf{R}) U(\mathbf{R}) = 0, \tag{3.3}$$

where U denotes the scalar component transverse to the direction of propagation. In the classical Rytov method, the optical field U at a propagation distance L is represented by [26,32]

$$\begin{aligned} U(\mathbf{R}) &= U(\mathbf{r},L) = U_0(\mathbf{r},L)\exp[y(\mathbf{r},L)] \\ &= U_0(\mathbf{r},L)\exp\left[\sum_{n=1}^{\infty} y_n(\mathbf{r},L)\right] \end{aligned} \quad , \tag{3.4}$$

where U_0 is the free space Gaussian beam wave as in Eq. (2.2) and y_n is the n^{th} order complex phase perturbations of the field.

Spectral representations are developed for calculating the statistical moments of the random optical field, which are valid up to second-order approximations [33]. The statistical moments m_k that are of greatest interest in FSO communications are the second-order moment or the mutual coherence function (MCF)

$$\begin{aligned} m_2(\mathbf{r}_1,\mathbf{r}_2,L) &= \left\langle U(\mathbf{r}_1,L)U^*(\mathbf{r}_2,L)\right\rangle \\ &= U_0(\mathbf{r}_1,L)U_0^*(\mathbf{r}_2,L)\left\langle \exp[y(\mathbf{r}_1,L)+y^*(\mathbf{r}_2,L)]\right\rangle , \\ &= M_2(\mathbf{r}_1,\mathbf{r}_2,L)\exp[2E_1(0,0)+E_2(\mathbf{r}_1,\mathbf{r}_2)] \end{aligned} \tag{3.5}$$

and the general fourth-order moment

$$\begin{aligned} m_4(\mathbf{r}_1,\mathbf{r}_2,\mathbf{r}_3,\mathbf{r}_4,L) &= \left\langle U(\mathbf{r}_1,L)U^*(\mathbf{r}_2,L)U(\mathbf{r}_3,L)U^*(\mathbf{r}_4,L)\right\rangle \\ &= U_0(\mathbf{r}_1,L)U_0^*(\mathbf{r}_2,L)U_0(\mathbf{r}_3,L)U_0^*(\mathbf{r}_4,L) \\ &\quad \times\left\langle \exp[y(\mathbf{r}_1,L)+y^*(\mathbf{r}_2,L)+y(\mathbf{r}_3,L)+y^*(\mathbf{r}_4,L)]\right\rangle \quad , \\ &= M_4(\mathbf{r}_1,\mathbf{r}_2,\mathbf{r}_3,\mathbf{r}_4,L)\exp[4E_1(0,0)+E_2(\mathbf{r}_1,\mathbf{r}_2)+E_2(\mathbf{r}_1,\mathbf{r}_4) \\ &\qquad +E_2(\mathbf{r}_3,\mathbf{r}_2)+E_2(\mathbf{r}_3,\mathbf{r}_4)+E_3(\mathbf{r}_1,\mathbf{r}_3)+E_3^*(\mathbf{r}_2,\mathbf{r}_4)] \end{aligned} \tag{3.6}$$

where $\langle\ldots\rangle$ indicates the long-time average and * denotes the complex conjugate operator. Assuming collimated wave propagation in a statistically homogeneous and isotropic random medium, the three integral functions E_1, E_2, and E_3 can be written as

$$E_1(0,0) = -2p^2 k^2 L \int_0^\infty k\Phi_n(k)\,dk \ , \tag{3.7}$$

$$\begin{aligned} E_2(\mathbf{r}_1,\mathbf{r}_2) = 4p^2 k^2 L \int_0^1 \int_0^\infty & k\Phi_n(k)\, J_0\left[k\left|\mathbf{p} - 2j\Lambda x\mathbf{q}\right|\right] \\ & \times \exp\left(-\frac{\Lambda L k^2 x^2}{k}\right) dk\,dx \end{aligned} \ , \tag{3.8}$$

$$\begin{aligned} E_3(\mathbf{r}_1,\mathbf{r}_2) = -4p^2 k^2 L \int_0^1 \int_0^\infty & k\Phi_n(k)\, J_0\left[(1 - j\Lambda x)\left|\mathbf{p}\right|\right] \\ & \times \exp\left(-\frac{\Lambda L k^2 x^2}{k}\right) \exp\left[-\frac{jLk^2 x}{k}\right] dk\,dx \end{aligned} \ , \tag{3.9}$$

where $\mathbf{p} = \mathbf{r}_1 - \mathbf{r}_2$, $\mathbf{q} = (\mathbf{r}_1 + \mathbf{r}_2)/2$, $\Lambda = 2L/kw_L^2$, and J_0 is the Bessel function of the first kind. These second-order and fourth-order moments lead to descriptions of the mean and covariance function of received intensity.

3.1.2 Mean of Intensity Fluctuations

The MCF of the optical field determines, among other quantities, the mean intensity of the field. Its general form in Eq. (3.5) can be rewritten as

$$\begin{aligned} m_2(\mathbf{r}_1,\mathbf{r}_2,L) = M_2(\mathbf{r}_1,\mathbf{r}_2,L) & \exp\left[s_r^2(\mathbf{r}_1,L) + s_r^2(\mathbf{r}_2,L) - T\right] \\ & \times \exp\left[-\frac{1}{2}\Delta(\mathbf{r}_1,\mathbf{r}_2,L)\right] \end{aligned} \ , \tag{3.10}$$

where $s_r^2(\mathbf{r},L) = [E_2(\mathbf{r},\mathbf{r}) - E_2(0,0)]/2$ describes the atmospherically induced change in the mean intensity profile in the transverse direction, and $T = -2E_1(0,0) - E_2(0,0)$ describes the change in the on-axis mean intensity at the receiver plane caused by turbulence. The last exponential term is the complex degree of coherence, where $\Delta(\mathbf{r}_1,\mathbf{r}_2,L)=E_2(\mathbf{r}_1,\mathbf{r}_1)+E_2(\mathbf{r}_2,\mathbf{r}_2)-2E_2(\mathbf{r}_1,\mathbf{r}_2)$.

Evaluating this MCF at $\mathbf{r}_1 = \mathbf{r}_2 = \mathbf{r}$ leads to an expression for the mean intensity fluctuations $\langle I \rangle$

$$\langle I(\mathbf{r},L)\rangle = I_0 \frac{w_0^2}{w_L^2}\exp\left(-\frac{2r^2}{w_L^2}\right)\exp\left[2s_r^2(\mathbf{r},L)-T\right], \tag{3.11}$$

from which the additional beam spread due to turbulence can be deduced. The expressions for s_r^2 and T evaluated using the Kolmogorov spectrum are given by

$$s_r^2(\mathbf{r},L) = 1.11 s_R^2 \Lambda^{5/6}\frac{r^2}{w_L^2}\,, \tag{3.12}$$

$$T = 1.33 s_R^2 \Lambda^{5/6}\,, \tag{3.13}$$

where s_R^2 is the Rytov variance defined in Eq. (3.1). From these two results, the mean intensity profile can be approximated by the Gaussian function [33]

$$\langle I(\mathbf{r},L)\rangle \cong I_0 \frac{w_0^2}{w_E^2}\exp\left(-\frac{2r^2}{w_E^2}\right), \tag{3.14}$$

where w_E is a measure of the effective beam spot size affected by turbulence defined as

$$w_E = w_L\left[1+1.33 s_R^2 \Lambda^{5/6}\right]^{1/2}. \tag{3.15}$$

This expression is considered a measure of the turbulence induced beam spreading, which increases the beam width beyond normal diffraction effects.

3.1.3 Covariance Function of Intensity

The fourth-order moment of the field is a cross correlation function between four spatial points in the receiver plane and can be expressed in the form

$$\begin{aligned} m_4(\mathbf{r}_1,\mathbf{r}_2,\mathbf{r}_3,\mathbf{r}_4,L) = m_2(\mathbf{r}_1,\mathbf{r}_2,L)m_2(\mathbf{r}_3,\mathbf{r}_4,L)\exp\big[E_2(\mathbf{r}_1,\mathbf{r}_4) \\ + E_2(\mathbf{r}_3,\mathbf{r}_2) + E_3(\mathbf{r}_1,\mathbf{r}_3) + E_3^*(\mathbf{r}_2,\mathbf{r}_4)\big]. \end{aligned} \tag{3.16}$$

An important specialized case leads to the expressions of the covariance function of the received intensity C_I defined by

$$C_I(\mathbf{r}_1,\mathbf{r}_2,L) = \frac{m_4(\mathbf{r}_1,\mathbf{r}_1,\mathbf{r}_2,\mathbf{r}_2,L)}{m_2(\mathbf{r}_1,\mathbf{r}_1,L)m_2(\mathbf{r}_2,\mathbf{r}_2,L)} - 1 = \frac{\langle I(\mathbf{r}_1,L)I(\mathbf{r}_2,L)\rangle}{\langle I(\mathbf{r}_1,L)\rangle\langle I(\mathbf{r}_2,L)\rangle} - 1 . \tag{3.17}$$

For $\mathbf{r}_1 = \mathbf{r}_2$, this equation reduces to the normalized intensity variance σ_I^2, also called the scintillation index, of the optical wave

$$\sigma_I^2(\mathbf{r},L) = \frac{\langle I^2(\mathbf{r},L)\rangle}{\langle I(\mathbf{r},L)\rangle^2} - 1, \tag{3.18}$$

which includes both temporal variation in received intensity and spatial variation within a receiver aperture. Under weak fluctuation conditions, this normalized intensity variance is approximately equal to the Rytov variance [34] given by Eq. (3.1), i.e. $\sigma_I^2 = \sigma_R^2$.

Based on the Rytov solution of a plane wave for homogeneous and isotropic turbulence, the covariance function of intensity under weak fluctuations can be expressed in the form [33]

$$C_I(r,L) = 8\pi^2 k^2 L \int_0^1 \int_0^\infty \kappa \Phi_n(\kappa) J_0(\kappa r)\left[1 - \cos\left(\frac{L\kappa^2 \xi}{k}\right)\right] d\kappa d\xi , \tag{3.19}$$

where $r = |\mathbf{r}_1 - \mathbf{r}_2|$ is the transverse distance between two points. The covariance function is useful in defining a characteristic coherence length r_c associated with intensity fluctuations. This usually involves the $1/e^2$ point of the normalized covariance function c_I defined by

$$c_I(r,L) = \frac{C_I(r,L)}{C_I(0,L)} = \frac{C_I(r,L)}{\sigma_I^2(L)}. \tag{3.20}$$

This coherence length can be shown to be directly related to the first Fresnel zone $\sqrt{\lambda L}$. If the collecting receiver aperture is larger than the coherence length, the fluctuations will be spatially averaged, hence reducing the intensity variance by a factor of *A* [12,33]

$$A = \frac{\sigma_I^2(D)}{\sigma_I^2} \approx \left[1 + 1.06\left(\frac{kD^2}{4L}\right)\right]^{-7/6}, \tag{3.21}$$

where $\sigma_I^2(D)$ is the intensity variance averaged over an aperture with diameter *D.*

The effects of aperture averaging in reducing the scintillation index on FSO links have also been observed experimentally [35,36]. Fig. 3.2 shows the aperture averaging factor as a function of receiver aperture diameter for a 1 km link. It shows that using an aperture diameter of 200 mm can reduce the intensity variance by a factor of 5.55×10^{-3}. Although the Rytov variance suggests that scintillation index can increase without limit, this is never experimentally observed since the scintillation is saturated and is typically limited to the order of unity. For a receiver with 200 mm aperture diameter, the averaging effect can reduce the intensity variance to the weak fluctuation regime.

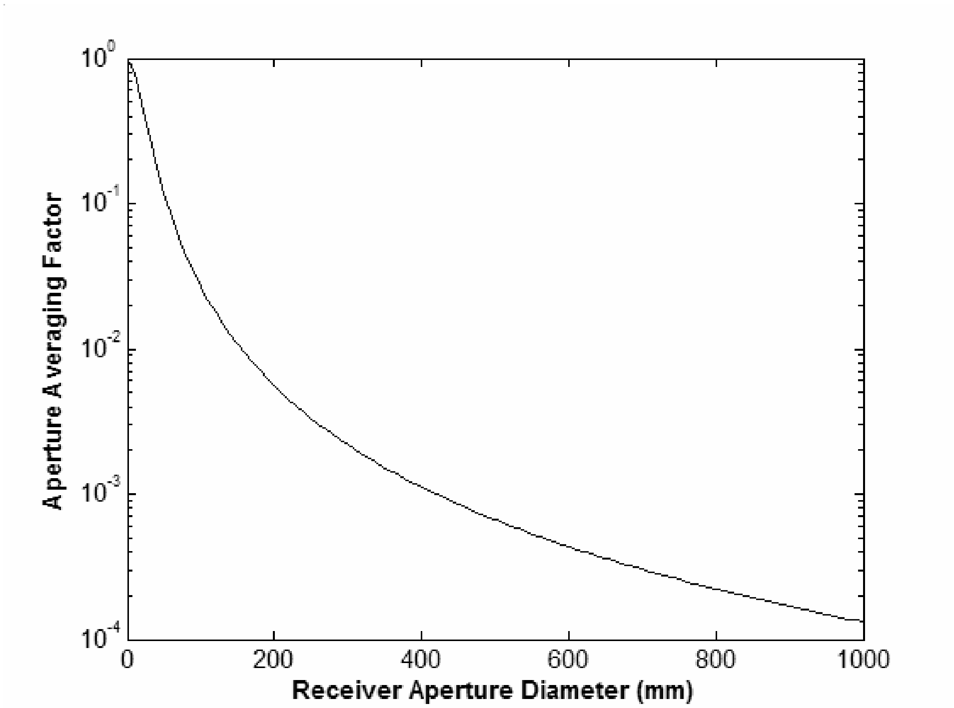

Figure 3.2: Aperture averaging factor versus receiver aperture size calculated from Eq. (3.21) for $L = 1$ km and $l = 785$ nm.

3.1.4 Distribution Models for Intensity Fluctuations

The performance of an FSO system with an atmospheric turbulence channel can be evaluated mathematically with knowledge of the probability density function (PDF) of the randomly fading intensity signal. Although many different PDF models have been proposed to deal with more general intensity fluctuation conditions, such as: *K* distribution, lognormal-Rician distribution, or gamma-gamma distribution [37,38,39]; the lognormal distribution is generally the accepted PDF in the weak fluctuation regime. Under weak fluctuations where single scattering of the optical wave occurs, the results of the Rytov approximation can directly lead to the derivation of this PDF model.

The Rytov approximation in Eq. (3.4) leads to the conclusion that the first-order complex phase perturbation y_1 is a complex Gaussian random process [26,32,33] and can be represented as

$$y_1(\mathbf{r},L) = c_1(\mathbf{r},L) + jS_1(\mathbf{r},L), \tag{3.22}$$

where c_1 and S_1 are the first-order log-amplitude and phase perturbation, respectively. Writing the total complex phase perturbation (up to second-order) as $y = (c_1 + c_2) + j(S_1 + S_2)$ and assuming that $c = c_1 + c_2$ remains Gaussian distributed, the intensity of the random field *I* takes the form

$$I = |U_0|^2 \exp(y + y^*) = I_0 e^{2c}, \tag{3.23}$$

where I_0 is the intensity of the unperturbed field as in Eq. (2.6). Rearranging this last relation leads to

$$c = \frac{1}{2}\ln\left(\frac{I}{I_0}\right), \tag{3.24}$$

which shows that under the Rytov approximation, the logarithm of the intensity is Gaussian or normally distributed. In this case, the PDF for the intensity fluctuations p_I is the lognormal distribution

$$p_I(i) = \frac{1}{i\sqrt{2ps_I^2}} \exp\left\{-\frac{1}{2s_I^2}\left[\ln\left(\frac{i}{\langle I(\mathbf{r},L)\rangle}\right) + \frac{1}{2}s_I^2\right]^2\right\},\ i > 0, \tag{3.25}$$

where the intensity variance s_I^2 can be obtained from the Rytov variance s_R^2.

3.1.5 The Effects of Atmospheric Turbulence on Performance

The most practical implementation for FSO communication involves the use of an intensity modulation/direct detection (IM/DD) system. The transmitted data is on-off keying (OOK) intensity modulated and goes through an atmospheric channel to the receiver. The receiver aperture collects the received optical signal and focuses it onto a photodetector, which converts the instantaneous optical power into electrical current for the detection process. In the presence of atmospheric turbulence between transmitter and receiver, the received signal exhibits random intensity fluctuations. Thus, the instantaneous received signal power P_R as expressed in Eq. (2.24) is a random quantity. The observed quantity is now the averaged or mean received signal power $\langle P_R \rangle$ given by

$$\langle P_R \rangle \cong \frac{\pi}{8} D^2 \langle I(0,L) \rangle = \frac{P_R}{1+1.33\sigma_I^2 \Lambda^{5/6}} . \tag{3.26}$$

Furthermore, it follows that the mean signal current is $\langle i_S \rangle = \Re \langle P_R \rangle$, where $\Re$ is the photodetector responsivity.

The output current from the detector $i = i_S + i_N$ in this case is a random variable, which has the mean value $\langle i_S \rangle$ and the variance $\sigma_i^2 = \sigma_S^2 + \sigma_N^2$, where σ_S^2 represents fluctuations in the signal that become a contributor to the detector noise and related to the normalized intensity variance σ_I^2 by

$$\sigma_S^2 = \langle i_S^2 \rangle - \langle i_S \rangle^2 = \langle i_S \rangle^2 \sigma_I^2 . \tag{3.27}$$

Using the relations given in Eqs. (3.26) and (3.27), and the definition of the output signal-to-noise ratio (SNR) in the absence of optical turbulence Γ_0 given in Eq. (2.27), the averaged SNR $\langle \Gamma_0 \rangle$ at the output of the detector assumes the form

$$\langle \Gamma_0 \rangle = \frac{\langle i_S \rangle^2}{s_i^2} = \frac{\Gamma_0}{\left(1 + 1.33 s_I^2 \Lambda^{5/6}\right)^2 + \Gamma_0 s_I^2} . \tag{3.28}$$

Thus, the presence of turbulence induced signal fluctuations will always deteriorate the SNR performance of IM/DD FSO system. Fig. 3.3 illustrates the mean SNR performance for three different normalized intensity variance values.

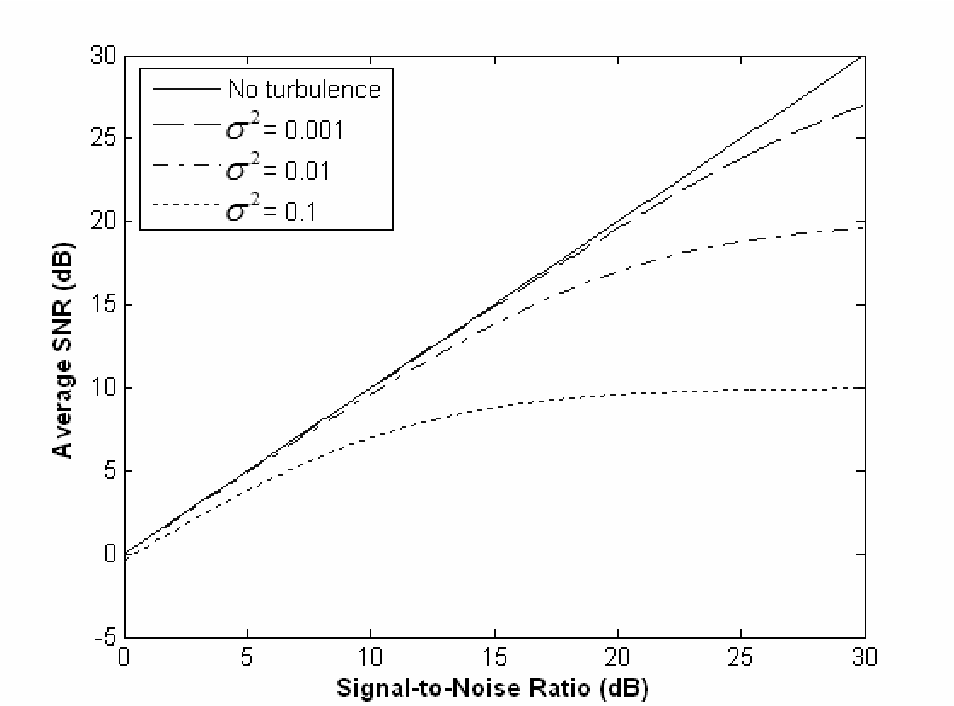

Figure 3.3: Average SNR performance in the presence of optical turbulence with $s^2 = 0.001$, 0.01, and 0.1; calculated from Eq. (3.28) for $\Lambda = 0.001$.

In the presence of optical turbulence, the bit error rate (BER) expression in Eq. (2.38) must be modified to incorporate the effects of signal fluctuations. In this case, the threshold level is now set to half the average signal corresponding to a received pulse ($i_T = \langle i_S \rangle / 2$). The false alarm probability p_f does not depend on the random received signal and can be written as

$$p_f = \Pr(1|0) = \frac{1}{2}\mathrm{erfc}\left(\frac{1}{2\sqrt{2}}\sqrt{\langle\Gamma_0\rangle}\right). \tag{3.29}$$

However, the miss probability p_m is now

$$p_m = \Pr(0|1) = \frac{1}{2}\mathrm{erfc}\left(\left[\frac{2i_S}{\langle i_S\rangle} - 1\right]\frac{1}{2\sqrt{2}}\sqrt{\langle\Gamma_0\rangle}\right), \tag{3.30}$$

where i_S is the random detector signal corresponding to the instantaneous received intensity. To compute the average BER $\langle \Pr(e) \rangle$, these equations must be averaged over the intensity fluctuation spectrum. This gives

$$\begin{aligned}\langle \Pr(e)\rangle = \frac{1}{4}\Bigg\{&\mathrm{erfc}\left(\frac{1}{2\sqrt{2}}\sqrt{\langle\Gamma_0\rangle}\right)\\ &+\int_0^\infty p_I(i_S)\,\mathrm{erfc}\left(\left[\frac{2i_S}{\langle i_S\rangle} - 1\right]\frac{1}{2\sqrt{2}}\sqrt{\langle\Gamma_0\rangle}\right)di_S\Bigg\},\end{aligned} \tag{3.31}$$

where $p_I(i)$ is the PDF of the intensity fluctuations.

The limiting performance of the average BER can be achieved by assuming the threshold level is dynamically set at half the instantaneous received signal level ($i_T = i_S / 2$), which leads to the expression

$$\langle \Pr(e)\rangle_L = \frac{1}{2}\int_0^\infty p_I(i_S)\,\mathrm{erfc}\left(\frac{i_S}{2\sqrt{2}\langle i_S\rangle}\sqrt{\langle\Gamma_0\rangle}\right)di_S\ . \tag{3.32}$$

Fig. 3.4 shows the numerical computation of theoretical BER for a FSO system as a function of no turbulence SNR using both Eqs. (3.31) and (3.32). While the expression in Eq. (3.31) gives a more accurate description of practical systems, the expression in Eq. (3.32) is more elegant and mathematically convenient. Observe that for different intensity variances in the weak fluctuation regime, the performance of the practical system approaches ideal system performance limit. We will use Eq. (3.32) when deriving an expression for the theoretical performance limit, and Eq. (3.31) when a more accurate model is needed for comparison with experimental results.

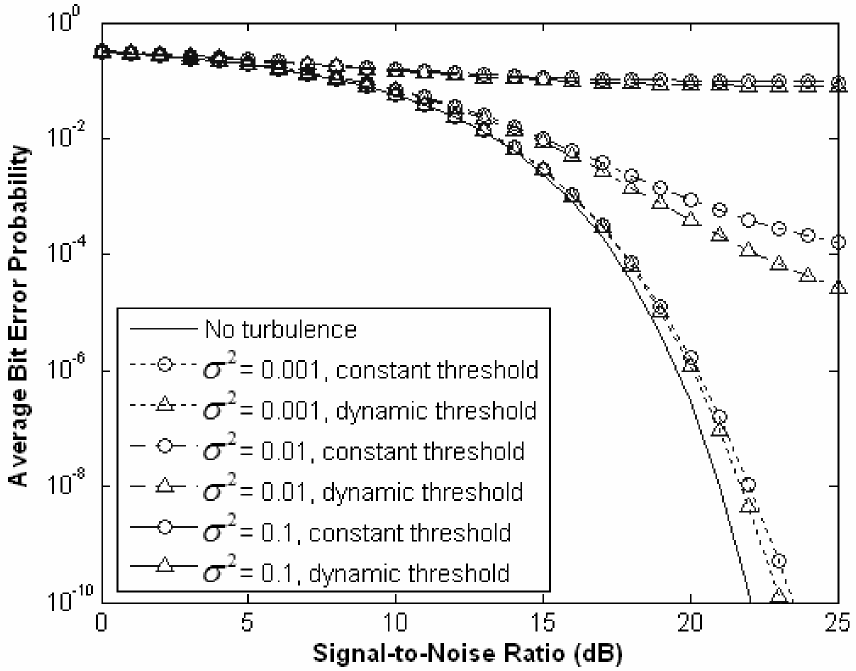

Figure 3.4: Theoretical BER performance of FSO system using constant threshold, from Eq. (3.31), and dynamic threshold, from Eq. (3.32); calculated for $s^2 = 0.001$, 0.01, and 0.1. The solid curve depicts BER performance in the absence of turbulence.

3.2 Design Considerations for a Time Delayed Diversity Scheme

One common way to improve the reliability of communication through a fading channel is by the use of diversity schemes. They provide two or more inputs at the receiver unit so that the fading phenomena among those inputs are uncorrelated. Communications performance is improved because the joint probability of error is less than the probability of error from individual channels. The time delayed diversity technique involves continuous retransmission of data streams separated by a time delay on the order of coherence time [15,16]. Given that time delayed diversity can use orthogonal polarization transmission, a concise discussion concerning the depolarization effects on a laser beam propagating in atmospheric turbulence is presented.

3.2.1 Temporal Covariance and Coherence Time

The statistical quantities of optical turbulence discussed thus far are in terms of spatial statistics, whereas in our work we were also concerned with the temporal statistics. Using the Taylor frozen turbulence hypothesis [40], a connection can be made between these two types of statistical quantities. This hypothesis states that temporal variations of meteorological quantities at a point are produced by advection of these quantities by the mean speed flow and not by the changes in the quantities themselves. This hypothesis permits converting spatial statistics into temporal statistics by knowledge of the average wind speed transverse to the direction of observation.

In the atmosphere, there are two time scales of concern: one is due to motion of the atmosphere across the observation path, and the other resulting from dynamics of the eddies. The first time scale, that due to advection, is typically on the order of 1 ms; while the second time scale, associated with the eddy turnover time, is typically on the order of 10 s. Because the second time scale is much slower than the first, it can be neglected in comparison with the average wind flow. Thus, under the Taylor frozen turbulence hypothesis, turbulent eddies are treated as frozen in space and are moved across the observation path by the average wind speed component v.

The temporal covariance function of the intensity fluctuations $C_I\left(t,L\right)$ can be obtained by substitution of $r \to vt$, where t is the time lag. Plots of the normalized covariance functions for several different weak scintillation conditions (with variance of 0.002, 0.01, and 0.05) obtained from our measurements are shown in Fig. 3.5 along with the theoretical calculations. The experiments were made with a 785 nm laser and a propagation length of approximately 1 km. The received signal amplitudes within a 50 ms window were recorded and the covariance functions were numerically computed. The coherence times for these particular fluctuation conditions, similarly defined as in Eq. (3.20), are approximately 7 ms, 5 ms, and 3.5 ms (for variance of 0.002, 0.01, and 0.05, respectively). This suggests that delays longer than few milliseconds should be sufficient for time delayed diversity to perform efficiently.

3.2.2 Laser Beam Depolarization Effects

The following analysis is concerned with determining the depolarized component of a laser beam propagated through atmospheric turbulence. We are interested in finding out whether depolarization effects could cause crosstalk between the two orthogonal polarization transmission channels in a time delayed diversity scheme. The expression for depolarization fluctuation, defined as a ratio between the depolarized and the main polarized components, is obtained by solving Maxwell's equations in free space using the method of small perturbations [41]. Recall that, the complete equation governing the behavior of the optical field **U** in a medium with no free charge can be written as

$$\nabla^2 \mathbf{U} + k^2 n^2 \mathbf{U} + 2\nabla\left[\mathbf{U}\cdot\nabla \log n\right] = 0\,, \tag{3.33}$$

where $n \approx 1 + n_1$ is the refractive index and n_1 represents small fluctuations about the mean.

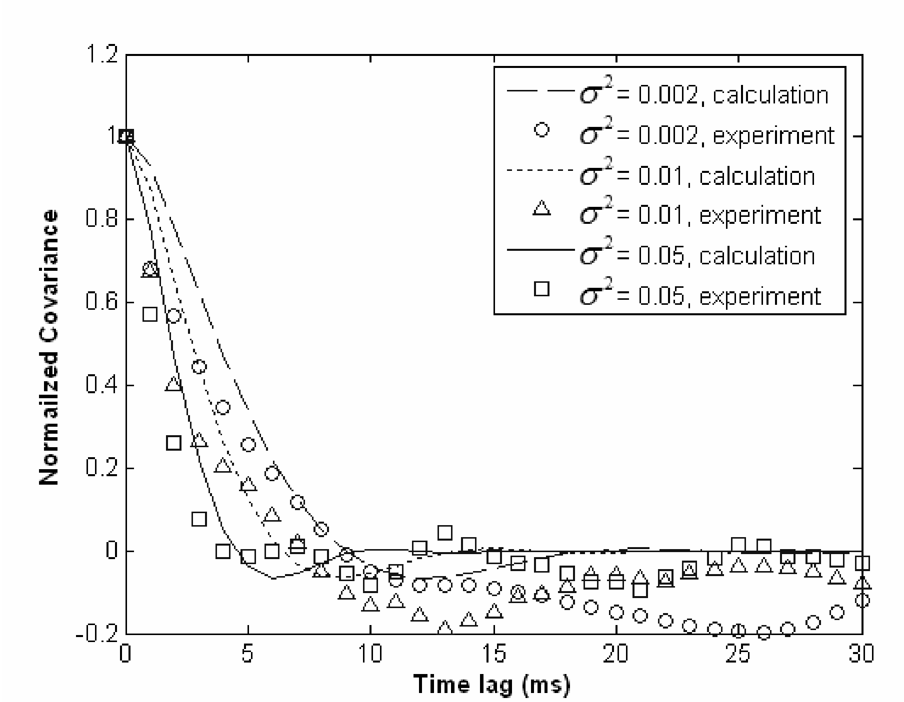

Figure 3.5: Temporal covariance functions for $s^2 = 0.002$, 0.01, and 0.05 obtained from measurements made with $L = 1$ km and $l = 785$ nm. The theoretical curves were computed from Eq. (3.19) and the use of Taylor turbulence hypothesis.

Let the optical field be expanded in the zeroth and first order terms of its perturbation series $\mathbf{U} = \mathbf{U}_0 + \mathbf{U}_1$, i.e. the incident and scattered wave. Assuming that the incident wave is linearly polarized in the *y*-direction and propagates along the *z*-direction, i.e. $\mathbf{U}_0 = A_0 e^{ikz}\hat{\mathbf{y}}$, the equation for the depolarized component of scattered wave in *x*-direction can be written as

$$\nabla^2 U_{1x} + k^2 U_{1x} = -2A_0 e^{ikz}\frac{\partial^2 n_1}{\partial x \partial y}\,. \tag{3.34}$$

If the depolarization fluctuation is defined as $y = U_{1x}/U_0$, where $U_0 = A_0 e^{ikz}$ and U_{1x} is the solution of the inhomogeneous Helmholtz differential equation, then

$$y = \frac{1}{2p}\int_V \frac{\partial^2 n_1(\mathbf{r}')}{\partial x' \partial y'} e^{-ik(z-z')} \frac{e^{ik|\mathbf{r}-\mathbf{r}'|}}{|\mathbf{r}-\mathbf{r}'|} dV' . \tag{3.35}$$

The solution of Eq. (3.35) can be found by first obtaining the spectral density of the correlation function of y in the plane of constant *z*. By the method of spectral expansion [26,41], the spectral density of the depolarized component can be expressed as

$$S_y(k_1, k_2, 0) = \frac{2pL}{k^2}\langle n_1^2 \rangle k_1^2 k_2^2 \Phi_n(k_1, k_2, 0) , \tag{3.36}$$

where Φ_n is the spatial power spectrum of refractive index fluctuations and $\langle n_1^2 \rangle$ is the mean squared refractive index fluctuation. The correlation function R_y can be obtained by taking the two-dimensional Fourier transform of S_y and the mean square fluctuations $\langle y^2 \rangle$ can be found from $R_y(0)$. Using a Gaussian-like spectral density for Φ_n (i.e. Tatarskii or Von Kármán spectrums) gives

$$\langle y^2 \rangle = \left\langle \left| \frac{U_{1x}}{U_0} \right|^2 \right\rangle = \frac{4\sqrt{p}\, L \langle n_1^2 \rangle}{k^2 l_o^2} , \tag{3.37}$$

where l_0 is the turbulence inner scale length. Note that $\langle y^2 \rangle$ can also be interpreted as the mean intensity depolarization, defined as the ratio between depolarized and main polarized received intensity.

Fig. 3.6 illustrates the mean intensity depolarization for our experimental range of a 1 km length as a function of $\langle n_1^2 \rangle$, where a scale length of 1 mm is used. It is evident that even for uncommonly large $\langle n_1^2 \rangle$ value (i.e. strong turbulence), the intensity of the depolarized component is predicted to be at least 30 dB smaller than the intensity of the main polarized component. Thus, a polarizing beam splitter (PBS) with an extinction ratio on the order of 30 dB should be sufficient to eliminate the possible crosstalk between the two polarization channel components in our system.

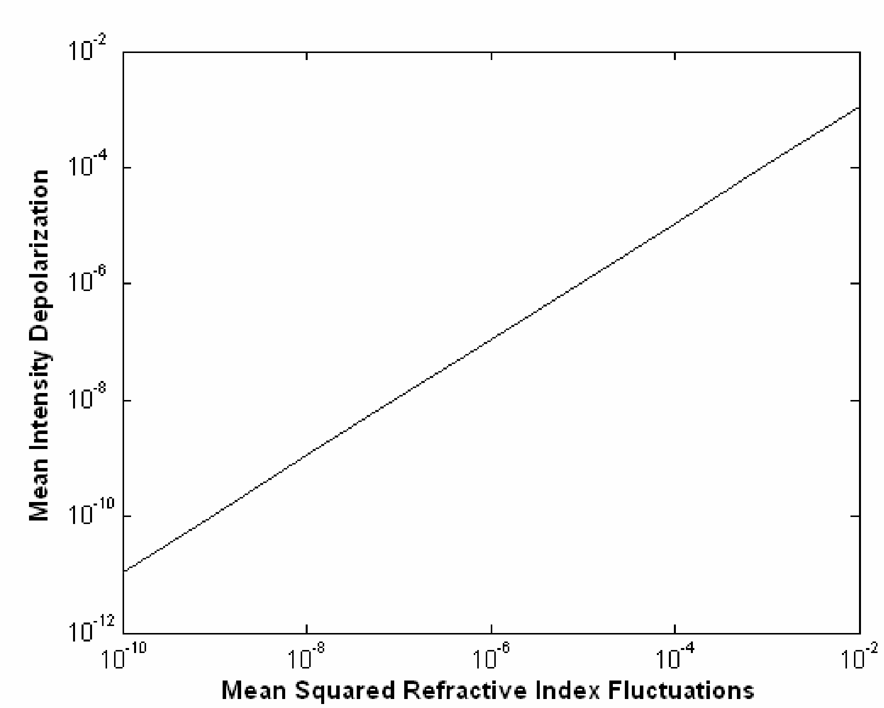

Figure 3.6: Mean of intensity depolarization calculated for FSO link with $L = 1$ km, $l = 785$ nm, and $l_0 = 1$ mm.

3.2.3 Diversity Schemes in Free Space Optical Systems

It has long been recognized by the radar and wireless communications community that reliable information transmission can be realized over a fading channel through the use of diversity techniques. Since the intensity fluctuations due to atmospheric turbulence has dependence on position, time, and wavelength; therefore spatial, temporal, and wavelength based diversity techniques could be used in FSO systems to create the least correlation between the fading received signals. After reception, they need to be combined such that the fades can be smoothed out.

Linear combining methods involve relatively simple weighted linear sums of multiple received signals. In coherent detection FSO systems, three common combining methods are: selection combining (SC), maximal ratio combining (MRC), and equal gain combining (EGC). Of the three architectures, the MRC receiver is optimal in that it yields a carrier with the largest average SNR and the least fading. For direct detection FSO systems, it is practical to use an array of detectors and combine the signal after the detection. This technique is called a post-detection linear combining method and has average SNR performance equivalent to the MRC.

To analyze the average SNR performance of a detector array receiver, let the summed output signal *Z* of statistically independent detectors be described by

$$Z = \sum_{k=1}^{M} i_k = \sum_{k=1}^{M} i_{S,k} + i_{N,k} \ , \tag{3.38}$$

where $i_{S,k}$ is a received fading signal with mean $\langle i_S \rangle$ and variance σ_S^2, $i_{N,k}$ is a zero-mean random noise with variance σ_N^2, and M is the number of detectors or diversity branches. For identically distributed random signal and noise, it follows that the average output SNR of an M-array detectors receiver $\langle \Gamma_M \rangle$ is given by

$$\langle \Gamma_M \rangle = \frac{\left(M \langle i_S \rangle \right)^2}{M \sigma_i^2} = M \langle \Gamma_0 \rangle , \tag{3.39}$$

where $\sigma_i^2 = \sigma_S^2 + \sigma_N^2$ is the variance of single detector output current and $\langle \Gamma_0 \rangle$ is the average SNR of a single detector as in Eq. (3.28). The expression in Eq. (3.39) is equivalent to the average SNR performance of the MRC scheme.

The above analysis shows that the output SNR from an *M*-array detectors receiver can improve the output SNR of a single detector receiver by the factor of *M*. However, the average SNR performance will only be a useful measure for systems communicating analog signal. In digital communication links, the performance measure is provided not directly by the SNR, but rather by the BER. Recall that the limit BER performance of single detector FSO receiver in the presence of turbulence is given by Eq. (3.32). Extending this expression for an array detector receiver, assuming the *M* branches are statistically independent as a result of the diversity, the average BER can be bounded by the M^{th}-power of the expression for average SNR in Eq. (3.32).

Fig. 3.7 shows the average BER performance curves of array detector receivers for various number of diversity branches with intensity fluctuations variance of 0.001 and 0.01. The graph clearly suggests that the biggest incremental improvement is achieved by using dual branch ($M = 2$) diversity. Consider the intensity variance of 0.001 and at BER value of 10^{-9}, the improvement between $M = 1$ (no diversity) and $M = 2$ is approximately 4 dB, between $M = 2$ and $M = 3$ is 2.5 dB, and between $M = 3$ and $M = 4$ is 1.8 dB. Given the increasing cost and complexity of array detector receiver circuitry, dual diversity may be considered as optimal.

3.3 Theoretical Modeling of Time Delayed Diversity System

To investigate the performance of time delayed diversity scheme, a theoretical model is required. Any ideal time delayed diversity system can be modeled as a dual branch diversity system over two correlated identically distributed lognormal fading channels [16]. The transmitter unit has two transmission paths: one for the prompt path and the other for the delayed path, with two orthogonal polarizations used as the transmission channels. By adjusting the delay between two transmissions with respect to turbulence coherence time, their dependency can be reduced (i.e. the channels become less dependent). Assuming an appropriate synchronization mechanism can be achieved, the receiver unit employs post-detection combining method by adding the signals from the two branches. A block diagram of this time delayed diversity system model is illustrated in Fig. 3.8.

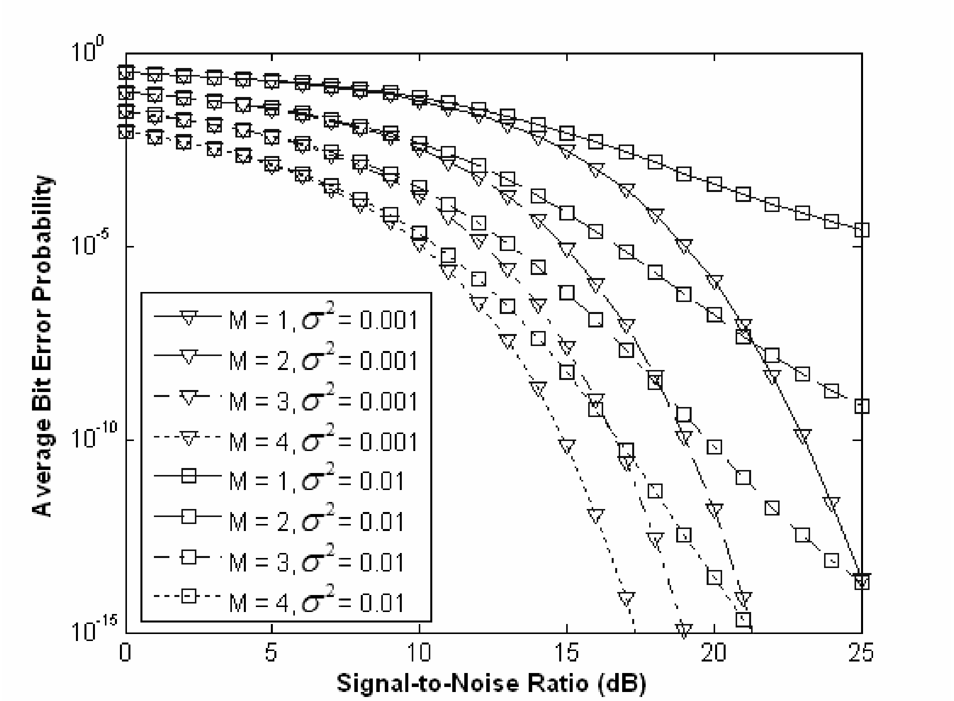

Figure 3.7: Average BER performance of FSO receiver with diversity branch *M* ranges from 1 to 4 and calculated for $s^2 = 0.001$ and 0.01.

Consider data that is transmitted twice and separated by a delay period t . The transmitted laser intensity in the two polarization states can be defined as $I_1 = I(t)$ and $I_2 = I(t - t)$. At the receiver, the received signal in each path $i_{S,k}$ for $k \in \{1,2\}$

has similar statistical behavior to the received intensity. Under weak fluctuations assumption, the joint PDF of random intensities I_1 and I_2 is

$$p_{I_1I_2}\left(i_1,i_2,t\right)=\frac{1}{i_1i_2\,2p\left|\Sigma\left(t\right)\right|^{1/2}}\exp\left[-\frac{1}{2}\left(\ln\mathbf{i}-\boldsymbol{\mu}\right)^T\Sigma^{-1}\left(t\right)\left(\ln\mathbf{i}-\boldsymbol{\mu}\right)\right], \tag{3.40}$$

where $\ln\mathbf{i}=\left[\ln i_1,\ln i_2\right]^T$ and $\boldsymbol{\mu}=\left(\ln\left\langle I\right\rangle-s_I^2/2\right)\mathbf{1}_{2\times1}$, with the mean received intensity $\left\langle I\right\rangle$ is given by Eq. (3.14). The temporal covariance matrix $\Sigma\left(t\right)$ can be written in term of the normalized intensity variance s_I^2 and the covariance function C_I as

$$\Sigma\left(t\right)=\begin{bmatrix} s_I^2 & C_I\left(t\right) \\ C_I\left(t\right) & s_I^2 \end{bmatrix}=s_I^2\begin{bmatrix} 1 & c_I\left(t\right) \\ c_I\left(t\right) & 1 \end{bmatrix}, \tag{3.41}$$

where in obtaining the last expression, the relation in Eq. (3.20) is used.

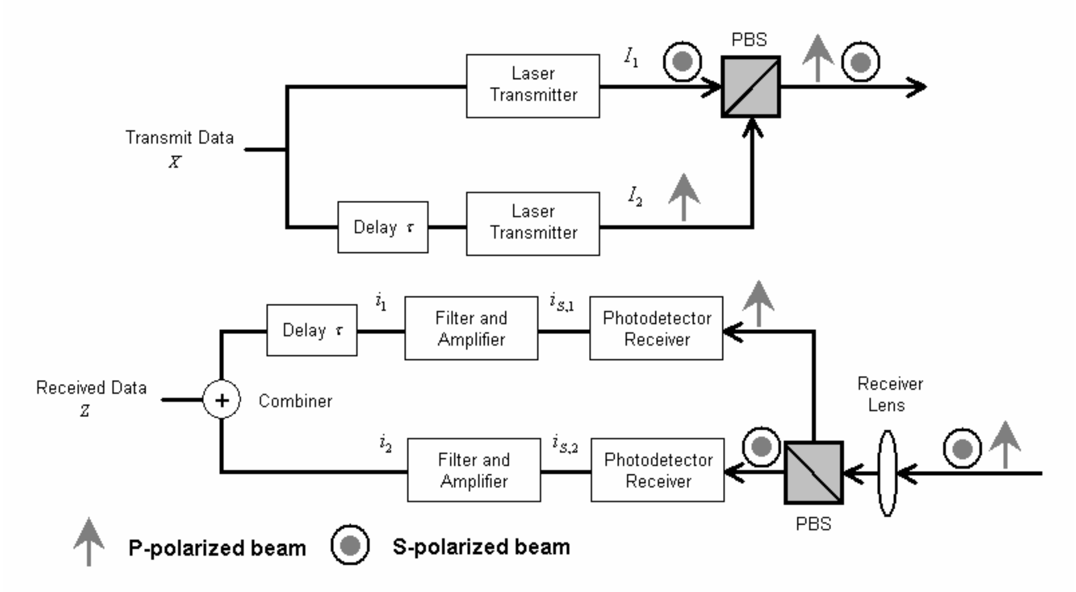

Figure 3.8: Block diagram of theoretical model of time delayed diversity system.

Suppose a simple synchronization method, such as applying an inverse delay, is performed by the receiver before the two paths are combined. Thus, the output signal of the combiner is $Z = i_1 + i_2 = \left(i_{S,1} + i_{S,2}\right) + \left(i_{N,1} + i_{N,2}\right)$. It follows that the average output SNR of the combiner $\left\langle \Gamma_Z \right\rangle$ is given by

$$\left\langle \Gamma_Z \right\rangle = \frac{\left(\left\langle i_{S,1} \right\rangle + \left\langle i_{S,2} \right\rangle\right)^2}{s_Z^2} = \frac{4\left\langle i_S \right\rangle^2}{s_Z^2}, \tag{3.42}$$

where the last equality is obtained by assuming that both received signals $i_{S,1}$ and $i_{S,2}$ have identical means $\left\langle i_{S,1} \right\rangle = \left\langle i_{S,2} \right\rangle = \left\langle i_S \right\rangle$. The output variance s_Z^2 can be written as

$$\begin{aligned} s_Z^2 &= s_{S,1}^2 + s_{S,2}^2 + 2\mathrm{Cov}\left(i_{S,1}, i_{S,2}\right) + s_{N,1}^2 + s_{N,2}^2 \\ &= 2\left\{\left\langle i_S \right\rangle^2 s_I^2 \left[1 + c_I\left(t\right)\right] + s_N^2\right\} \end{aligned}, \tag{3.43}$$

where the simplification in Eq. (3.43) is derived using the relations defined in Eqs. (3.17), (3.20), and (3.27); and assuming identical distributions of both random signal and noise. It can be shown that the average SNR at the combiner output $\left\langle \Gamma_Z \right\rangle$ is related to the SNR for a single detector output Γ_0 by

$$\left\langle \Gamma_Z \right\rangle = \frac{2\Gamma_0}{\left(1 + 1.33 s_I^2 \Lambda^{5/6}\right)^2 + s_I^2 \left[1 + c_I\left(t\right)\right]\Gamma_0}. \tag{3.44}$$

As has been previously stated, the average BER performance is an accurate performance metric to assess the performance of digital communication systems and to capture the advantage of diversity systems in reducing fading. For a time delayed diversity system in the presence of turbulence, assuming an ideal case where the threshold level can be dynamically set to half of the instantaneous signal at the combiner output (i.e. $i_T = \left(i_{S,1} + i_{S,2}\right)/2$), the expression for the conditional BER in the combiner output $\Pr\left(e\right)$ can be written as

$$\Pr(e) = \frac{1}{2}\operatorname{erfc}\left(\frac{i_{S,1} + i_{S,2}}{4\sqrt{2}\langle i_S \rangle}\sqrt{\langle \Gamma_Z \rangle}\right). \tag{3.45}$$

The average BER is then obtained by integrating this expression over the joint density function of I_1 and I_2 given in Eq. (3.40). This leads to an expression for $\langle \Pr(e) \rangle$ as

$$\langle \Pr(e) \rangle = \frac{1}{2}\int_0^\infty\int_0^\infty p_{I_1 I_2}\left(i_{S,1}, i_{S,2}, t\right)\operatorname{erfc}\left(\frac{i_{S,1} + i_{S,2}}{4\sqrt{2}\langle i_S \rangle}\sqrt{\langle \Gamma_Z \rangle}\right) di_{S,1}\, di_{S,2}\ . \tag{3.46}$$

However, the theoretical system model described above presents several issues in its implementation. The first issue involves the buffering and synchronization mechanisms, where the notion of transmission delay is implemented. Since the coherence times are in the order of milliseconds, there is no sensible delay line available for this purpose. Thus in our system, the buffering and synchronization are applied to the data bits in the digital domain, instead of to the analog carrier signals. This forces the demodulation to be performed prior to the combining process. The combiner then logically adds the two synchronized bit streams to produce the recovered information. The possibilities that an error can occur for a given transmitted bit and demodulation result are summarized in Table 3.1.

Table 3.1: Demodulation error in a receiver using logical OR as digital combiner.

Transmitted Bit	Received Channel 1	Received Channel 2	Recovered Bit	Error Status
0	0	0	0	Correct
0	0	1	1	Error
0	1	0	1	Error
0	1	1	1	Error
1	0	0	0	Error
1	0	1	1	Correct
1	1	0	1	Correct
1	1	1	1	Correct

Another important issue is regarding the assumption of an ideal threshold, which is capable of describing half the instantaneous signal value. A more practical implementation is the use of a low pass filter to get the average signal value at a given time window, and use half of this constant value as the detection threshold. This method corresponds to the abstraction derived in Eqs. (3.29) to (3.31). Also notice that the false alarm probability, as defined in Eq. (3.29), is still constant for any intensity variance, whereas the miss probability is greatly affected by the received intensity variations. This effect is illustrated in Fig. 3.9 for different examples of intensity variance encountered in our experiments.

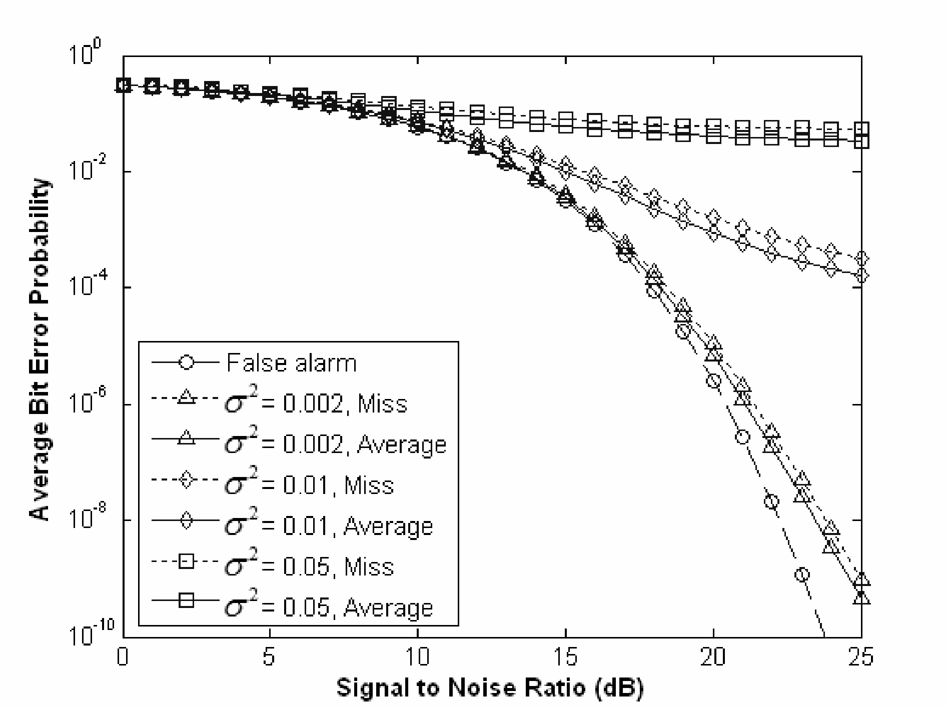

Figure 3.9: Comparison of the false alarm, miss, and average error probabilities in a FSO link calculated from Eqs. (3.29) – (3.31) for $s^{2} = 0.002$, 0.01, and 0.05.

From the relations given in Table 3.1, the conditional BER now corresponds to the false alarm probability of either channel or the miss probabilities for both channels. Also observe that the miss probability is typically much larger than the false alarm probability; hence the average probability of error can be adequately approximated only by the miss probability. Therefore, the conditional BER for practical time delayed diversity system $\Pr(e)_{TDD}$ is given by

$$\Pr(e)_{TDD} \approx \frac{1}{2} p_{m,1} p_{m,2} = \frac{1}{8} \prod_{k=1}^{2} \operatorname{erfc}\left(\left[\frac{2 i_{S,k}}{\langle i_S \rangle} - 1 \right] \frac{1}{2\sqrt{2}} \sqrt{\langle \Gamma_0 \rangle} \right), \tag{3.47}$$

where the mean and variance of the received signals at both channels are taken to be equal. Again, the average BER at the combiner output $\langle \Pr(e) \rangle_{TDD}$ is obtained by integrating this expression over the joint PDF $p_{I_1 I_2}$ and can be written as

$$\begin{aligned} \langle \Pr(e) \rangle_{TDD} = & \frac{1}{8} \int_0^\infty \int_0^\infty p_{I_1 I_2} \left(i_{S,1}, i_{S,2}, t \right) \\ & \times \prod_{k=1}^{2} \operatorname{erfc}\left(\left[\frac{2 i_{S,k}}{\langle i_S \rangle} - 1 \right] \frac{1}{2\sqrt{2}} \sqrt{\langle \Gamma_0 \rangle} \right) d i_{S,k} \end{aligned} . \tag{3.48}$$

3.4 Characterization of System Performance

To characterize the performance of a time delayed diversity system over fading atmospheric turbulence channels, both average SNR and average BER are common performance measures used in wireless communication systems. Although it is easier to find, average SNR may not capture all the benefits of diversity. To capture the importance of time delayed diversity schemes in reducing fading-induced fluctuations, we need to look at the average BER. This measure reveals the actual system behavior and performance in digital communications. In addition, the effect of variable delay period on the performance of time delayed diversity system is also discussed.

3.4.1 Bit Error Rate Performance

In this section, the BER performance of the theoretical model of time delayed diversity system is investigated and characterized. The parameters used in the simulations are based on the design for the clear atmosphere experimental setup. In this setup, the FSO link between transmitter and receiver units is approximately 1 km long. At the transmitter, two 785 nm laser diode modules with equal power and orthogonally polarized are used for the prompt and delayed channels. The receiver uses an aspheric lens with aperture diameter of 200 mm. The two polarizations of the received optical beam are split using a 30 dB sensitivity PBS and separately detected by high-speed amplified silicon photodetectors. The received electrical signals are then threshold detected and re-amplified to satisfy the desired signal level standards.

The average BER performances were calculated for two intensity variance values of 0.002 and 0.01; and the results are showed in Figs. 3.10 and 3.11 for the practical and theoretical system models, respectively. For each model, three different cases, namely $t = 0$, $t = t_c$, and $t \to \infty$, were evaluated and compared to a system with no diversity. The values used for t_c are taken from the results given in Sec. 3.2.1, thus the case of $t = t_c$ represents the performance of time delayed diversity on FSO links. The case of $t = 0$ corresponds to increasing the transmitted power by 1.5 dB (i.e. double the input SNR) with no diversity; and the case of $t \to \infty$ corresponds to a completely independent fading channel condition.

The theoretical system performance results in Fig. 3.11 suggest that time delayed diversity can give a SNR gain of about 4 dB (at BER of 10^{-9}) and 5.8 dB (at BER of 10^{-4}) over a no diversity system for intensity variances of 0.002 and 0.01, respectively. Notice when the received SNR is doubled due to an increase in transmitted laser power, the performance improvement is still inferior to time delayed diversity on the order of a few dB. A larger improvement is exhibited for stronger turbulence, although in this situation the BER value is much larger. The results indicate that given some BER requirement, the required SNR value can be lower for a time delayed diversity system. This further implies, for the same turbulence condition, longer FSO communication links can be achieved when this scheme is employed.

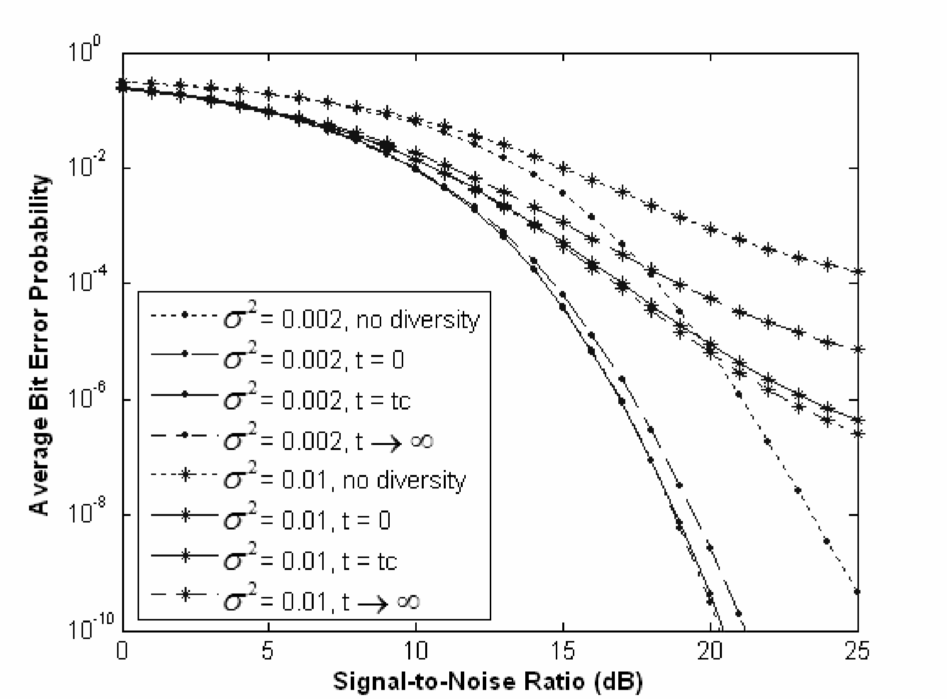

Figure 3.10: Average BER performance for practical system model, from Eq. (3.48), calculated for no diversity, $t = 0$, $t = t_c$, and $t \rightarrow \infty$ cases. The performance was evaluated for turbulence with $s^2 = 0.002$ and 0.01.

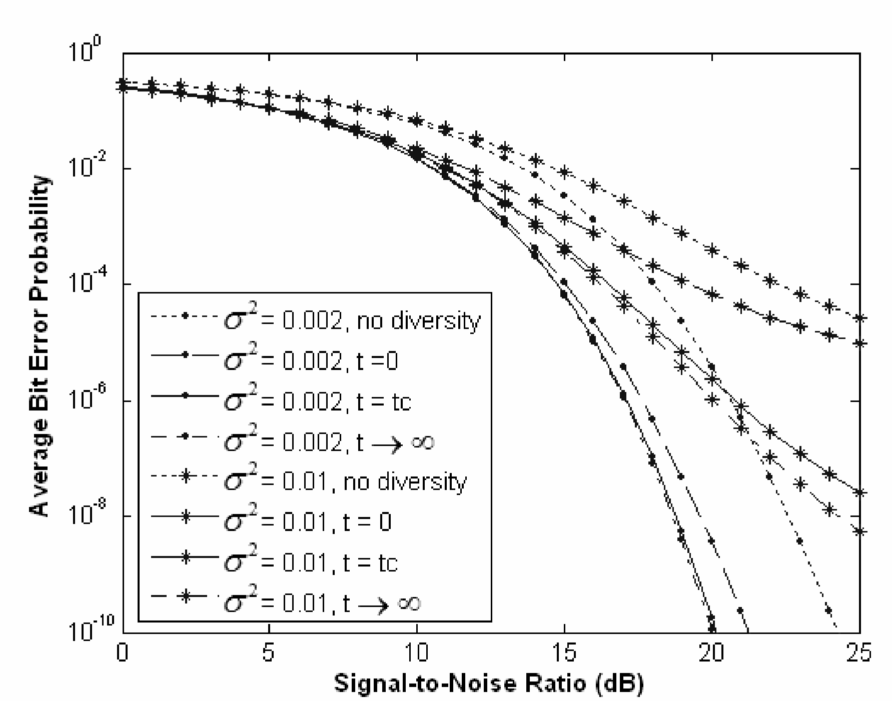

Figure 3.11: Average BER performance for theoretical system model, from Eq. (3.46), calculated for no diversity, $t = 0$, $t = t_c$, and $t \rightarrow \infty$ cases. The performance was evaluated for turbulence with $s^2 = 0.002$ and 0.01.

3.4.2 The Effects of Delay Period on Receiver Performance

From the simulation results, observe that in the limiting case of $t \rightarrow \infty$, the average BER performance can still be improved further. This additional SNR gain is due to the fact that the temporal covariance does not completely vanished beyond the coherence time. Introduction of additional delay provides more independence between the two channels. By increasing the delay period, we can improve performance but communication latency and the required buffer size are also increased. Therefore, the optimum delay period need to be chosen to satisfy a given performance requirement. An example regarding how this delay affects the average BER performance is shown for a turbulence variance of 0.002 and is plotted in Fig.

3.12. The SNR is chosen to have a value of 141, which corresponds to a BER value of 10^{-9} under no turbulence conditions.

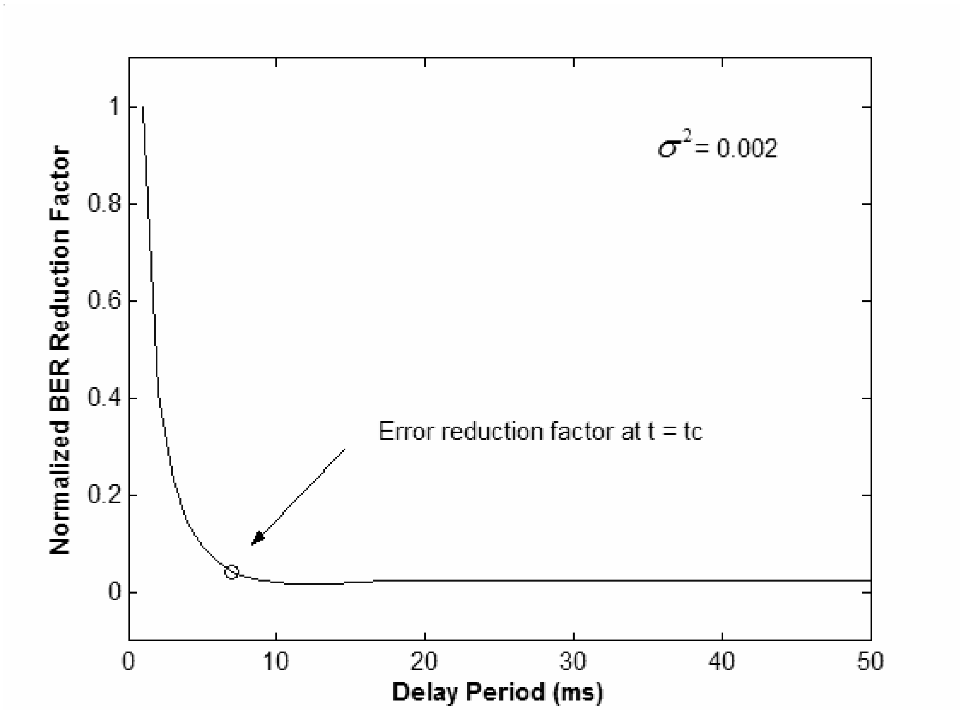

Figure 3.12: Effects of variable delay in reducing the average BER calculated for $s^2 = 0.002$. The BER reduction factor is defined as the average BER computed at delay period t, normalized to its value at $t = 1$ ms.

The average BER was computed for various delay periods from 1 to 50 ms, and the BER reduction factor is defined by normalizing the average BER to its maximum value, which occurs for a delay period of 1 ms. This metric can be considered as a trade-off parameter between communication performance and costs, similar to the aperture averaging factor defined earlier in Sec. 3.1.3. In this example, the reduction factor has a minimum of approximately 2.5%, and is almost constant for delay periods longer than 20 ms. When the delay periods equal to the coherence time (i.e. 7 ms in this case), this value is around 4.3%. This indicates only small performance improvement (less than 2%) may be gained by extending the delay period further, while system costs could be more than doubled.

3.5 Comparison to Time Interleaving Scheme

There are other types of diversity schemes that could be used in FSO communications, such as: space, wavelength, and time diversity [42,43]. In space diversity, the receivers are separated by distance on the order of the coherence length of the intensity covariance function. For a few kilometer link ranges, the coherence length is on the order of centimeters, and multiple receivers only need to be placed centimeters apart to see approximately independent channel fades. Wavelength diversity may be implemented either by using hybrid FSO and radio frequency (RF) systems or by using combination of semiconductor and quantum cascade lasers (QCLs), which can be adjusted to operate in the mid and long-wave infrared regions (3 to 20 μm) [44].

In the time diversity scheme, also termed as time interleaving, identical messages are transmitted in different time slots (interleaved) separated by time periods on the order of the coherence time. The receiver receives M independently faded copies of the signal, applies appropriate delay to each copies, combines them, and demodulates the messages. Fig. 3.13 shows an FSO receiver that uses time interleaving. Since both time interleaving and time delayed diversity use similar statistical property of intensity fluctuations (i.e. temporal covariance), the comparison will only be made between these two diversity schemes. Assuming similar buffering and synchronization mechanisms are utilized, this time interleaving system with $M = 2$ is isomorphic to the time delayed diversity described in Sec. 3.3.

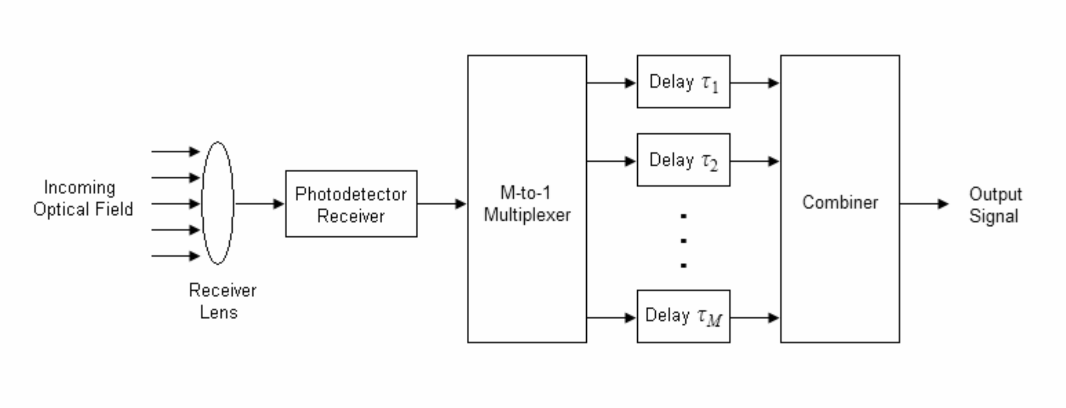

Figure 3.13: Block diagram of FSO receiver with time interleaving.

In contrast to a time delayed diversity transmitter, the transmitted power in a time interleaving system is not divided into two orthogonal polarization components; hence there is no 3 dB reduction in the transmitted power. Thus, the average SNR at combiner output is a useful metric in comparing the performance of these two diversity schemes. Fig. 3.14 shows the average SNR output of both time delayed diversity and time interleaving systems for intensity variance of 0.001, 0.01, and 0.1. The calculations were made with the assumption that the delay period was long enough such that perfectly independent channels were obtained (i.e. $t_c \to \infty$).

Observe that for smaller SNR values, time interleaving outperforms time delayed diversity system by up to 3 dB. However, in the limit where the SNR value becomes more useful for obtaining reliable communications, the performance of both systems converges. Furthermore, time interleaving has a major drawback of incurring large delays due to having to wait for all the copies to be received before the messages can be detected. Consequently for $M = 2$ case, this causes the data rate to decrease by two times, resulting in only 50% bandwidth efficiency in comparison with the time delayed diversity system.

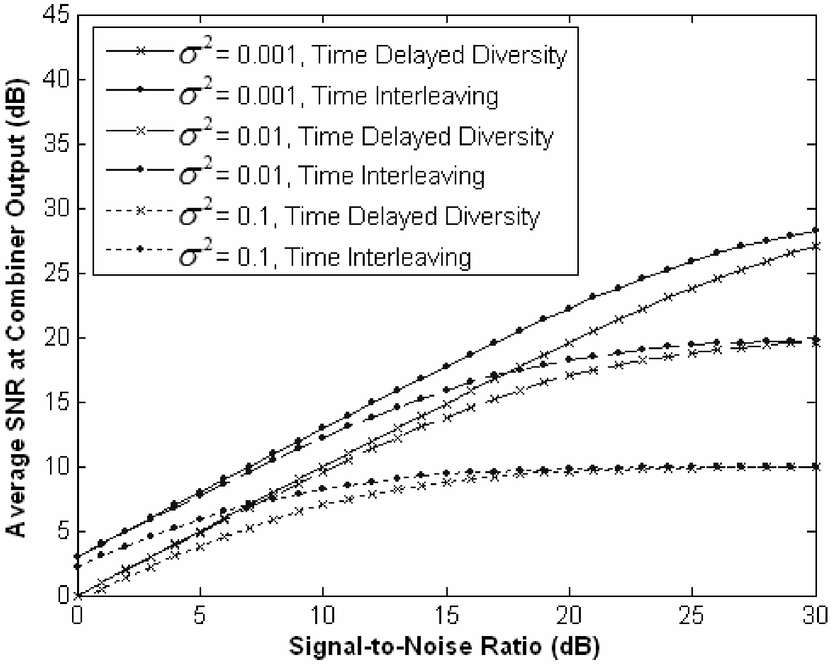

Figure 3.14: Comparison of SNR performance between time interleaving and time delayed diversity FSO systems calculated for $s^{2} = 0.001$, 0.01, and 0.1; and $t_c \to \infty$.

3.6 Summary

Theoretical analysis of FSO communication systems using a time delayed diversity scheme has been presented. For typical weak intensity fluctuation conditions observed on our experimental setup, the classical Rytov approximation is used to derive and obtain the statistical properties of the atmospheric channel, most important of which are the expressions for the mean and covariance function of intensity fluctuations. It has been pointed out that the lognormal distribution is typically used as an appropriate and correct PDF model in the weak intensity fluctuation regime. Several important issues related specifically to time delayed diversity, such as temporal covariance of intensity fluctuations, laser polarization fluctuations, and diversity receiver architecture, are also analyzed; and the results were used to determine the parameters required in developing a prototype system used in our experimental work.

We also derived and characterized the performance of a time delayed diversity system, which can be modeled as a dual branch diversity system over two correlated identically distributed lognormal fading channels. The theoretical performance results indicate that time delayed diversity can give an SNR gain up to 5.8 dB over no diversity systems. The SNR gain can be further improved when the transmission delay is made longer than 20 ms. However this will only give a very small incremental improvement ($\leq 2\%$), while the communication costs may be potentially increased by at least two times. Comparison between time delayed diversity and time interleaving schemes is also presented. Although time interleaving does not suffer from 3 dB power penalty as time delayed diversity does, it has a key disadvantage in the reduction of bandwidth efficiency to only one half of the time delayed diversity value.

Chapter 4: Experimental Investigations of Time Delayed Diversity System

4.1 Overall Descriptions of the Experimental System

Recall that in a time delayed diversity system, the transmitted information is carried in two different channels: one for the prompt data and another for the delayed data. Since theoretically the atmosphere has been shown to have little chirality, the polarization state of a propagating optical wave should be well preserved on link up to several kilometers range (i.e. no significant depolarization effects) [2,41]. This provides orthogonal polarization channels in the time delayed diversity scheme. The prompt data is transmitted using a transverse magnetic (TM) or P-polarized laser beam, and the delayed data is transmitted using a transverse electric (TE) or S-polarized laser beam. The delay is provided by buffering the data into the memory of the host computer.

The dual orthogonal polarization channels in our experimental system are realized using two laser modules, one is P-polarized and another is S-polarized; which are optically combined and transmitted to free space through a common transmit aperture. For our experiments, the laser modules operate in constant current mode and could support digital modulation from DC to 10 Mbps. Although it has been suggested that the preferable transmission wavelength for all visibility conditions is 10 μm, the improvement compared to typical wavelength used in optical communications (i.e. 785 to 1550 nm) is only ~0.2% [43]. Since the attenuation is basically flat over these wavelengths, they do not play a crucial role in the transmitter design.

At the receiver, the laser beam is split into two polarization components and separately detected. The P-polarization corresponds to the prompt channel, thus the receiver must delay this data stream before combining with the data stream carried by the S-polarization. A similar buffering mechanism as in the transmitter is used to provide this delay, and the appropriately synchronized data streams are logically added to recover the information. The communication uses RS-485 protocol for serial communications, which can operate at sufficiently high data rate (up to 10 Mbps), and provide close to raw data error measurement (i.e. no coding effect is included). The measurement data and error analysis was conducted using MatLab.

4.2 Simulated Convective Turbulence Experiment

A preliminary experiment to implement time delayed diversity technique had been conducted and some results on performance of free space optical (FSO) links have been obtained [15]. In this experimental work, commercially available FSO transceivers designed for point-to-point laser communication are used and modified. We studied the performance of our time delayed diversity FSO system under the conditions of laboratory generated convective turbulence. The discussion regarding RS-485 used as the synchronization and communications protocol is also presented.

4.2.1 Experimental System Design and Setup

For our experiments, we used modified LumenLink OWL155/200 optical transceivers. These transceivers are designed for direct line-of-sight (LOS), point-to-point laser communication over distance up to 200 m, supporting data rates up to 155 Mbps. The transmitted laser power is 10 mW at an infrared wavelength of 1.3 μm. The output beam is collimated with full angle beam divergence about 2 mrad. The receiver unit uses a 40 mm diameter aspheric lens in front of a 75 μm InGaAs photodetector. Since these FSO systems operate with PECL signal levels, interface circuits are required and designed to translate them to the signal levels used in RS-485 communication protocol.

To build a time delayed diversity transmitter, two LumenLink transmitters are used. The driver circuits were designed to control these transmitters directly from a host computer. The host computer controls data transmission for both the prompt channel and provides data buffering for the delayed channel. A polarizing beam splitter (PBS) is used to construct orthogonal polarization transmission by passing the transmitted (P-polarized) and reflected (S-polarized) laser beam carrying prompt and delayed data, respectively. At the receiving end, the two channels are separated by PBS and independently detected by two LumenLink receivers. The receiver software provides the buffering mechanism for the prompt channel and combines it with the delayed channel using a post-detection combiner.

The buffer size becomes part of the communication parameters in time delayed diversity scheme. It has to be determined prior to data transmissions, so the transmitter and receiver can be synchronized and information can be correctly recovered. The size of the buffer can be varied according to the observed turbulence. This memory buffer size N_{buffer} is related to the delay period t by knowing the operating bit rate R_{bit} according to

$$N_{buffer} \cong \frac{t}{T_{bit}} = t\,R_{bit}\,, \tag{4.1}$$

where $T_{bit} = 1/R_{bit}$ is the bit period. For a bit rate of 10 Mbps, a memory buffer size of 100 kbits is required in order to get the effects of 10 ms delay separation.

The performance of time delayed diversity system was investigated under the presence of localized turbulence generated by hot plates. Hot plates placed on the path between transmitter and receiver of an FSO link, are known to generate convective turbulence [45]. In our experiment, Cimarec2 hot plates, which have temperature variations from 5º to 540º C with temperature control on a scale from 1 to 10, were used. To vary signal-to-noise ratio (SNR) values at the receiver, an iris diaphragm is placed in front of the main receiver aperture to control the received optical power. Our experimental setup is illustrated in Fig. 4.1.

4.2.2 Buffer Synchronization and Communications Protocol

As it had been mentioned earlier, RS-485 serial data standard is used as the communication protocol in our prototype system. RS-485 can support communications up to 1.2 km and bit rates up to 10 Mbps, noting that data rate must be traded off against cable length [46]. RS-485 transmission lines are differential in nature, thus minimizing the emitted electromagnetic interference (EMI) by cross-canceling the opposing fields around each wire. The receivers are designed to respond to the differential signals and must be sensitive to a 200 mV differential voltage. An

RS-485 receiver outputs ‘one’ if this differential voltage is larger than +200mV, and ‘zero’ if it is smaller than -200mV.

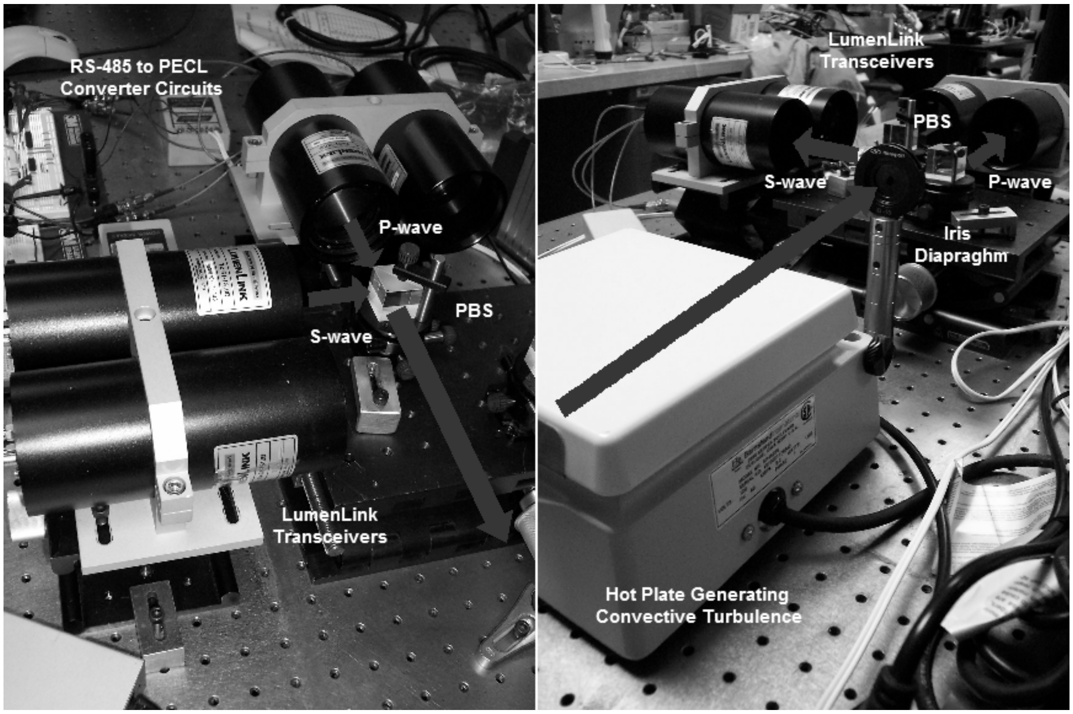

Figure 4.1: Time delayed diversity FSO experiment in convective turbulence link.

Similar to RS-232 serial protocol, an RS-485 communication is asynchronous, meaning that a clock signal is not sent along with the data. Each word is synchronized using its start bit and an internal clock on each side keeps tabs on the timing. When idle, the transmission line is in the logic ‘one’. A transmission starts with a start bit, which is in the logic ‘zero’. Then each bit is sent down the line, one at a time, starting with the least significant bit (LSB). If a parity checker is used, one additional parity bit is inserted right after the last data bit, then the signal is appended with stop bit(s) (logic ‘one’) to make up the transmission.

In our system, two RS-485 ports are used, one for each channel (i.e. prompt and delayed). The transmission buffering is then performed in the following way. For a given buffer size *N* in byte, an array of size *N* is created. Every time incoming random input data arrives, the data is sent to the serial port of prompt channel and also copied to the head of buffer array. Then, the data from the tail of buffer array is retrieved and sent to the serial port of delayed channel. In the receiver, since *N* is known, the buffering can be applied to the prompt channel, synchronizing the two data channels for the combiner. The flowchart of these processes is shown in Fig. 4.2, and the control software was programmed in MatLab.

4.2.3 The Effects of Localized Convective Turbulence

Experimental studies of the effects of local strong turbulence on the performance of FSO links suggest that hot plates placed near FSO transmitter or receiver generate strong convective turbulence, although this may not necessarily have the same characteristics as the atmospheric turbulence [45]. At the transmitter, localized convective turbulence will immediately produce wavefront aberration, which leads to a reduction in the received power and possibly random steering in beam trajectory (i.e. beam wander). The effect of localized turbulence at the receiver is less severe, since a wavefront tilt at the receiver cannot steer the beam off to any significant extent. Thus, the major effect is undesirable spot dancing of the received light in the receiver focal plane, which leads to scintillation.

It is also suggested that at stronger convective turbulence conditions the link performance is dependent on the location of the turbulence source. More specifically, the errors are more likely to occur when the heater is placed near the transmitter. However, at weaker turbulence levels, location of turbulence along the path is insignificant. Therefore, in our experiments, the hot plates were fixed and located in

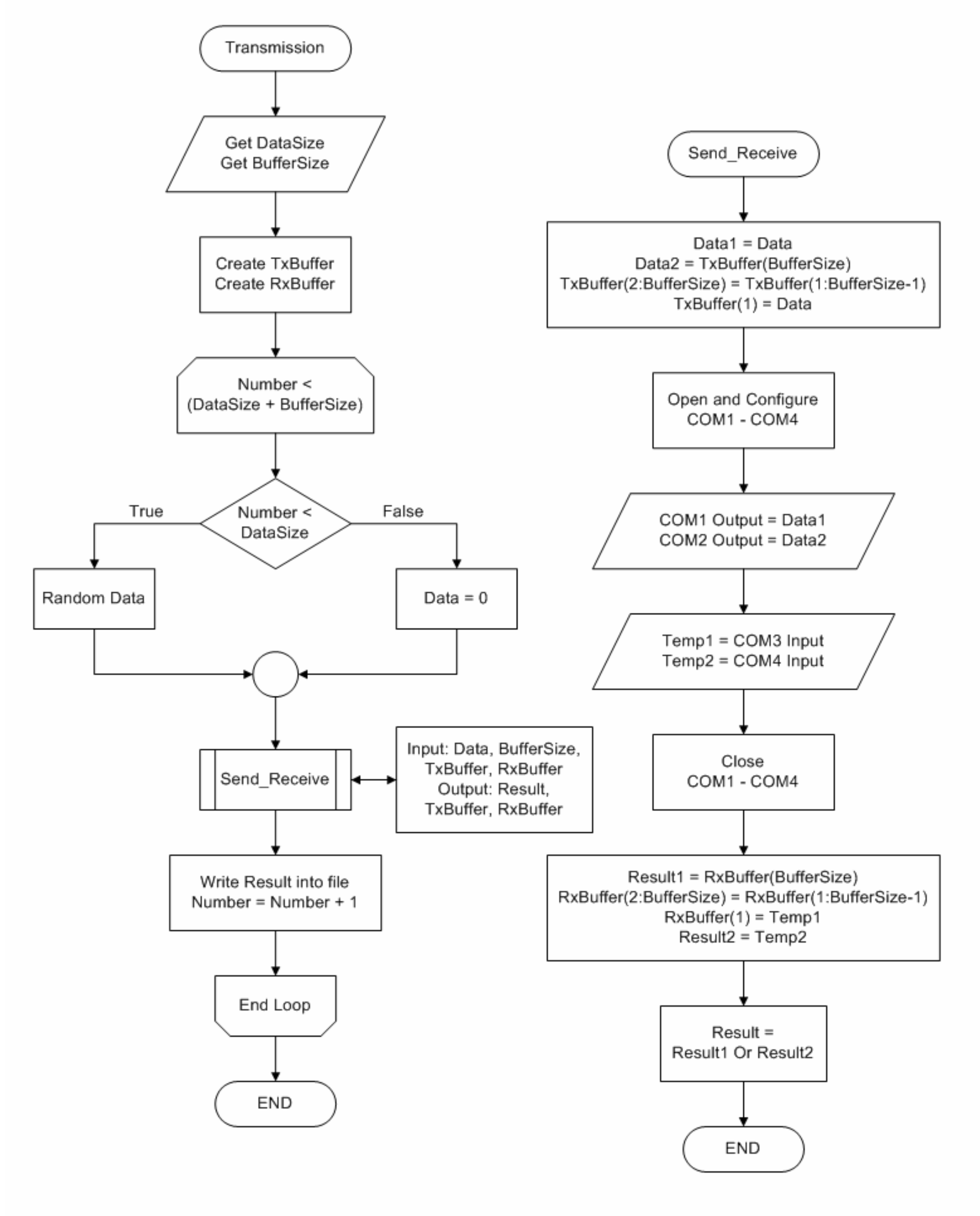

Figure 4.2: Flowchart of data transmissions and synchronizations.

the middle of the propagation path. To characterize the error statistics of the turbulence generated by these hot plates, random binary data were transmitted from the transmitter to the receiver along the turbulence path. We then measured bit error as a function of SNR for several different temperature values. Fig. 4.3 shows the experimental results for several intensity variance values ranging from 9×10^{-4} to 2×10^{-3}.

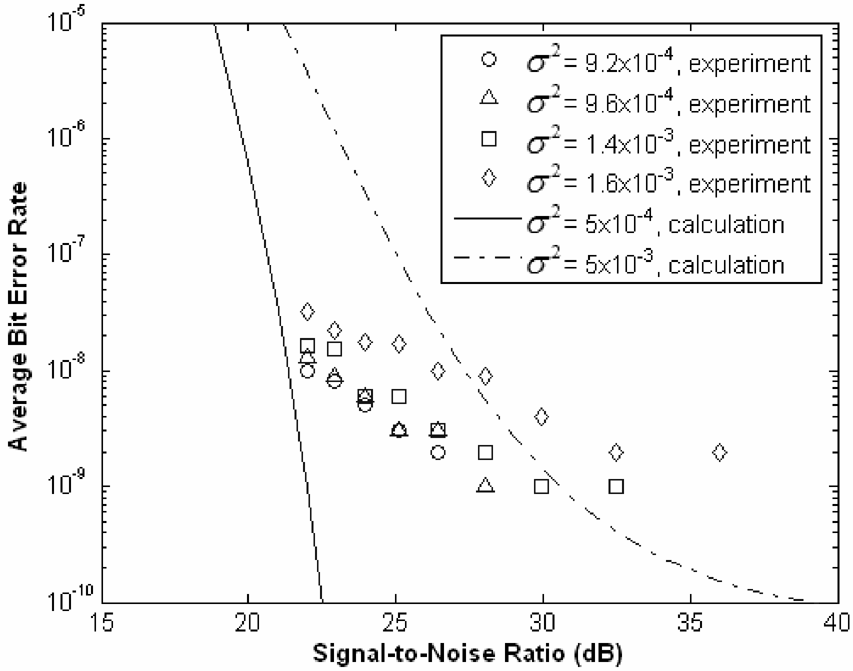

Figure 4.3: Error statistics of the hot plates generated turbulence measured for s^{2} ranges from 9×10^{-4} to 2×10^{-3}. The theoretical curves were calculated from Eq. (3.32) for $l = 1.3$ µm, and $s^{2} = 5\times10^{-4}$ and 5×10^{-3}.

4.3 Results and Analysis for Simulated Convective Turbulence

First, the temporal statistics of hot plate generated turbulence was investigated and measured to obtain the coherence time. The laser beam was transmitted over the heated plate and the received laser intensity was measured using a digital oscilloscope. We recorded several time series within a 500 ms period window and sampling rates of 1000 samples per second. To obtain the temporal covariance function, the mean of the signal was subtracted, and self-convolution was performed on the time series. Fig. 4.4 shows some typical examples of temporal covariance functions for intensity variance values of 9.6×10^{-4} and 1.6×10^{-3}.

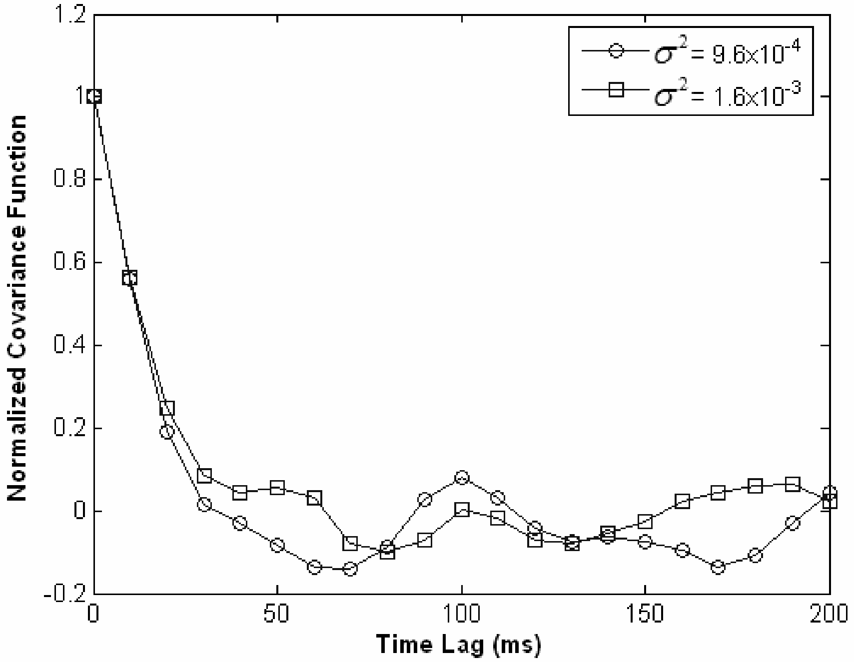

Figure 4.4: Temporal covariance functions of the convective turbulence obtained from measurements made with $l = 1.3$ µm, for $s^2 = 9.6\times10^{-4}$ and 1.6×10^{-3}.

The performance of our time delayed diversity system was measured for different time delay periods. Based on the experiments, the coherence times are on the order of 20 ms. Thus, for simplicity we set one delay period to be 20 ms regardless of the intensity variance values. For a data rate of 10 Mbps, this implies a buffer size of 200 kbits. Figs. 4.5 and 4.6 show the bit error rate (BER) performance of time delayed diversity FSO system corresponds to intensity variance values of 9.6×10^{-4} and 1.6×10^{-3} respectively, using several different delay periods compared to the BER performance of the non-delayed FSO system.

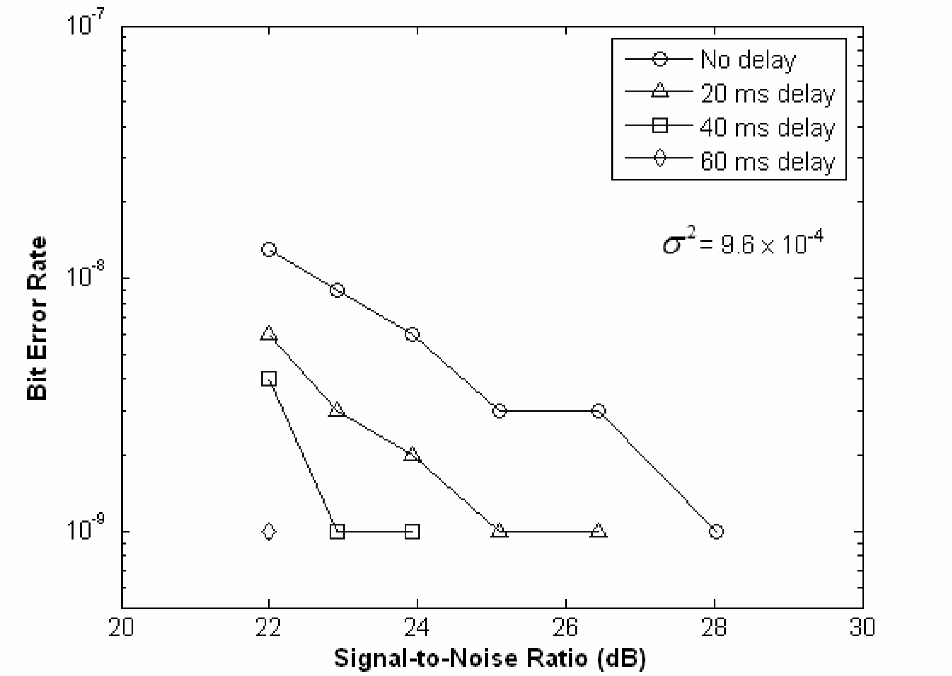

Figure 4.5: BER performance of time delayed diversity FSO system measured under convective turbulence with $s^2 = 9.6\times10^{-4}$, and for the case of no delay, $t = 20$ ms, 40 ms, and 60 ms.

The results clearly suggest the performance improvements of time delayed diversity system over a non-delayed FSO system. On average, the improvements gained by 20 ms period time delayed diversity system correspond to $s^2 = 9.6\times10^{-4}$ and $s^2 = 1.6\times10^{-3}$ are about 2.3 dB and 4.6 dB. As it is suggested by the theory, larger improvement is exhibited for stronger turbulence condition, although in this situation the BER is worse. Further improvements still can be gained by extending the delay into 40 ms and 60 ms periods. In these cases, additional improvements ranging from 1.6 to 3.8 dB can be achieved. These experimental studies confirm the usefulness of time delayed diversity technique to mitigate the effects of fading induced by turbulence.

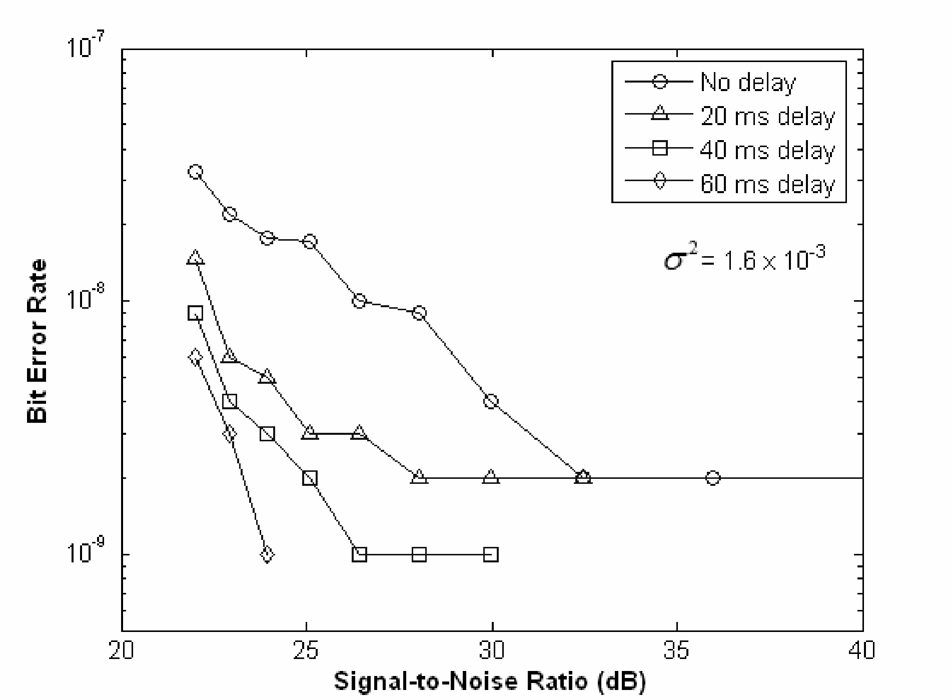

Figure 4.6: BER performance of time delayed diversity FSO system measured under convective turbulence with $s^2 = 1.6\times10^{-3}$, and for the case of no delay, $t = 20$ ms, 40 ms, and 60 ms.

4.4 Clear Atmospheric Turbulence Experiment

According to the initial results obtained from the laboratory experiment, we were confident that the time delayed diversity technique would also work in real turbulence case. To study the performance of the system under clear atmospheric turbulence conditions, a test-bed consisting of an FSO link between buildings was constructed, which allows the performance of the time delayed diversity system to be investigated and analyzed over a broader range of turbulence conditions [16]. Discussions on system design, experimental test-bed setup, and data measurements are presented.

4.4.1 Experimental System Design and Setup

The experimental FSO link is constructed between the roof of A.V. Williams Building and an office in the Chesapeake Building at the University of Maryland, College Park campus; and is approximately 1 km long. At the transmitter, two 785 nm laser diode modules with 70 mW power each are used for the prompt and delayed channels. The optical transmitter is located outdoors on the roof, while the host computer is placed inside an HVAC control room. These two subsystems are optically connected, meaning that serial RS-485 signals generated by the computer are converted into optical signals using electro-optical media converters and transported using multi mode fiber optic cables to the optical transmitter.

Since optical power efficiency is very important factor in constructing long-range FSO systems, a PBS is not a good optical component to use in producing polarized light. One major disadvantage of using PBS is that some portion of the laser power may be discarded, which can be problematic for longer communication links. If a laser output light has already linearly polarized with an arbitrary polarization angle, then half-wave plates can be used to rotate this polarized light to become either P- or S-polarization. In our optical transmitter, two zero-order half-wave plates are used to produce two orthogonal polarizations of the collimated laser output beams and then a PBS is used to combine these two beams. Fig. 4.7 shows the setup of our FSO transmitter system.

The receiver system is installed indoor and uses a plano-convex lens with 200 mm aperture diameter. The lens has a focal length of 300 mm and 90% spectral transmissions for 785 nm wavelength. The orthogonal polarizations of the received optical beam are then split using a PBS with 1000:1 extinction ratio, and separately detected by high-speed amplified silicon photodetectors. These detectors are designed for detection of light signals from DC to 50 MHz, and have active area of 0.8 mm^2. For optical wavelength of 785 nm the detector responsivity is about 0.43 A/W, which corresponds to about 70% in quantum efficiency.

Figure 4.7: Picture of time delayed diversity FSO transmitter system in clear atmospheric turbulence link.

The amplifiers are terminated with 50 Ω resistors to produce output signal levels up to 5 V. However, the received electrical signals are in general very weak. Therefore, a variable amplifier is needed in order to bring the signals back to the usable levels. After that the signals are threshold detected and the detection results are converted to RS-485 signal levels used as the communication protocols. Electronics circuits were designed and manufactured to implement these functions. The recovered serial data from both channels are collected, synchronized, and combined by the host computer. Fig. 4.8 shows the setup of our FSO receiver system.

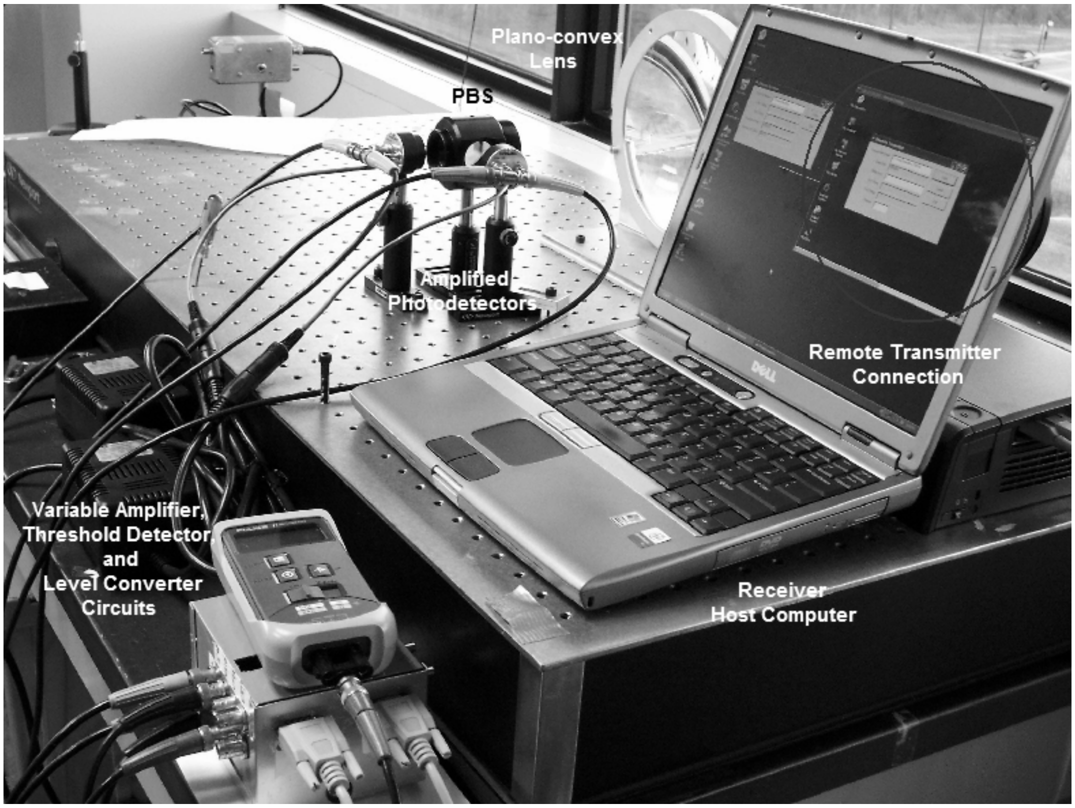

Figure 4.8: Picture of time delayed diversity FSO receiver system in clear atmospheric turbulence link.

4.4.2 Link Budget Analysis

When choosing the required laser power in FSO communications, it is very important to consider the appropriate link budget. Link budget is a design method to ensure that enough power will reach the optical receiver given that there will be some losses on the optical link. The FSO link budget equation is normally written in dB and is given by

$$P_R = P_T + L_{FSO} + L_{Atm} + L_{System} + M_L \, , \tag{4.2}$$

where L_{FSO}, L_{Atm}, and L_{System} are the FSO losses due to beam diffraction, atmospheric attenuation, and various transceiver system losses, respectively. The link margin M_L represents the maximum additional loss the system can handle, including the effects of atmospheric turbulence, severe weather conditions, and imperfect alignment for system with no tracking.

The link budget of our FSO test-bed system, in the absence of the atmospheric turbulence, is listed in Table 4.1. From this table, the link margin M_L can be computed as

$$\begin{aligned} M_L &= P_T + L_{FSO} + L_{Atm} + L_{System} - P_R \\ &= 18.45 - 20 - 1.7 - 1.35 + 35.48 \\ &\cong 30.9\text{dB}. \end{aligned} \tag{4.3}$$

Table 4.1: Link budget analysis for 1 km experimental FSO link.

System Components	Descriptions	Power
785 nm Laser Module	70 mW maximum transmitted power	18.45 dBm
Transmitter Clear Glass Window	4% surface reflectivity	–0.18 dB
Atmospheric Transmission	Assuming 10 km visibility (clear air)	–1.7 dB
Building Double Pane Window	15% surface reflectivity	–0.71 dB
FSO Loss	Geometrical loss due to beam diffraction	–20 dB
Plano-Convex Receiver Lens	90% spectral transmission	–0.46 dB
High Speed Amplified Si Photodetector	40 pW/vHz maximum receiver sensitivity (NEP)	–35.48 dBm

In the absence of turbulence, this link margin is sufficient to maintain BER performance of 10^{-9} in a digital communication system, which corresponds to 21.5 dB noise margin. However, in the presence of atmospheric turbulence, received intensity fading induced by the turbulence may result in the detection errors. Fading may easily provide up to 10 dB additional losses to the link margin, and there were occasions when 40 dB fading were observed [47]. Thus, it is reasonable to assume that bit errors encountered in our experiment were mostly due to the effects of fading.

4.4.3 User Interface and Data Acquisition Algorithm

In this experiment, the data are transmitted in frames for more reliable transmissions, as in the case of Ethernet protocols. The size of the frames can be varied and typically are between 10 and 100 bytes per frame. Unlike in previous experiment, the delay is realized using timer function specified by the transmitter. The timer can be specified in multiples of milliseconds, which is on the order of the coherence time of intensity fluctuations. The timer starts when the first frame is transmitted in the prompt channel. While the prompt channel keeps transmitting the data frames, the delayed channel will not start its transmission until the timer reaches its end value.

Since transmission is performed frame-by-frame, the receiver does not need to know about the delay. The receiver can readily synchronize and recover the received data frames, given that the frame size is known. The combiner is performed per frame according to the order in which they are received. This will automatically result in delay of the recovered data with respect to transmitted data. However, for most communication systems, such a small fixed delay is generally acceptable. The flowcharts of the user interface and software control are illustrated in Fig. 4.9. For this experiment, the software for our time delayed diversity system was programmed using Visual Basic.

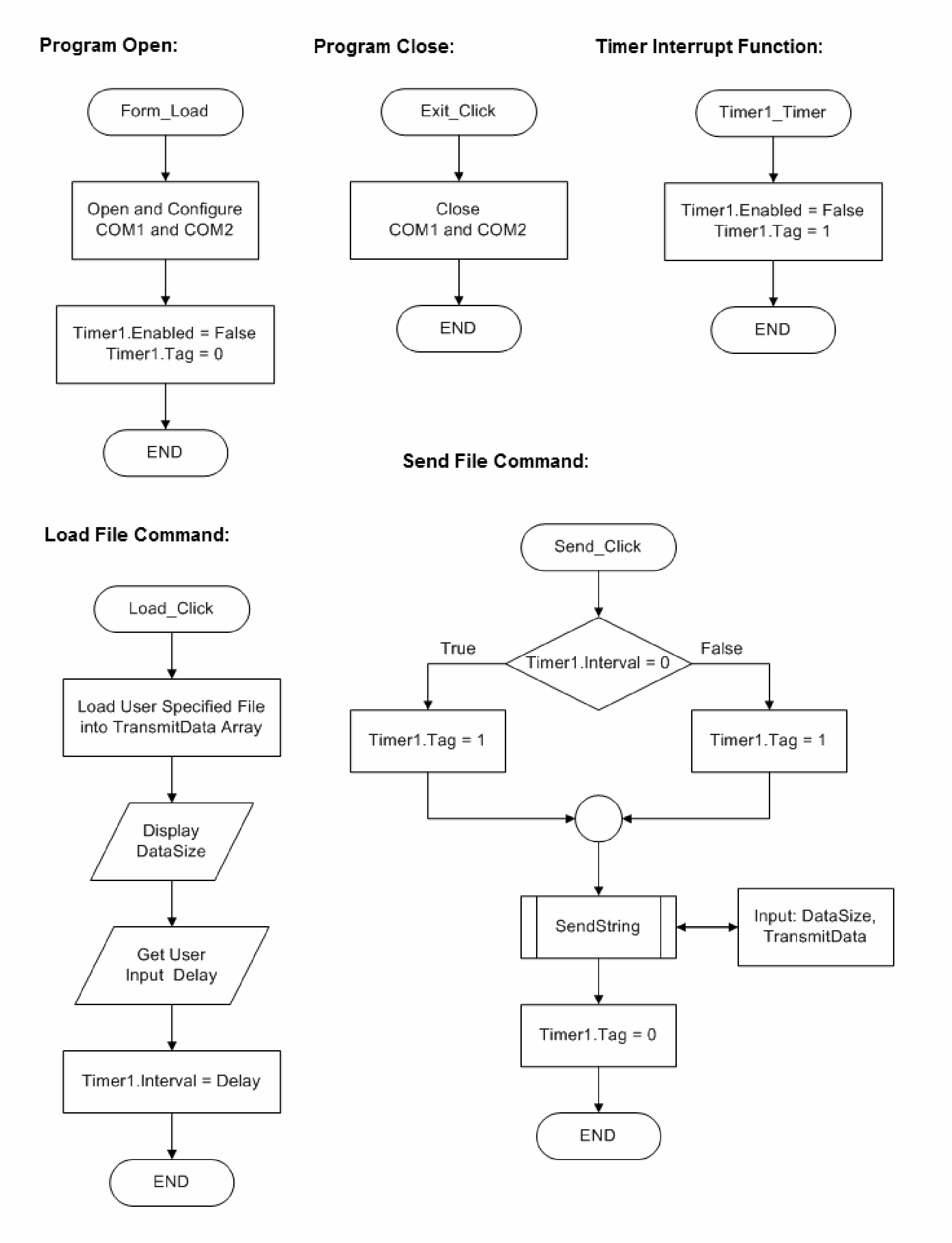

Figure 4.9: Flowcharts of user interface and control processes.

To obtain bit error measurements, a file containing *N* bytes random data is created at the transmitter. At the receiver, the recovered data are saved into a file in order to be compared to the input source file at the transmitter. The bit errors are then

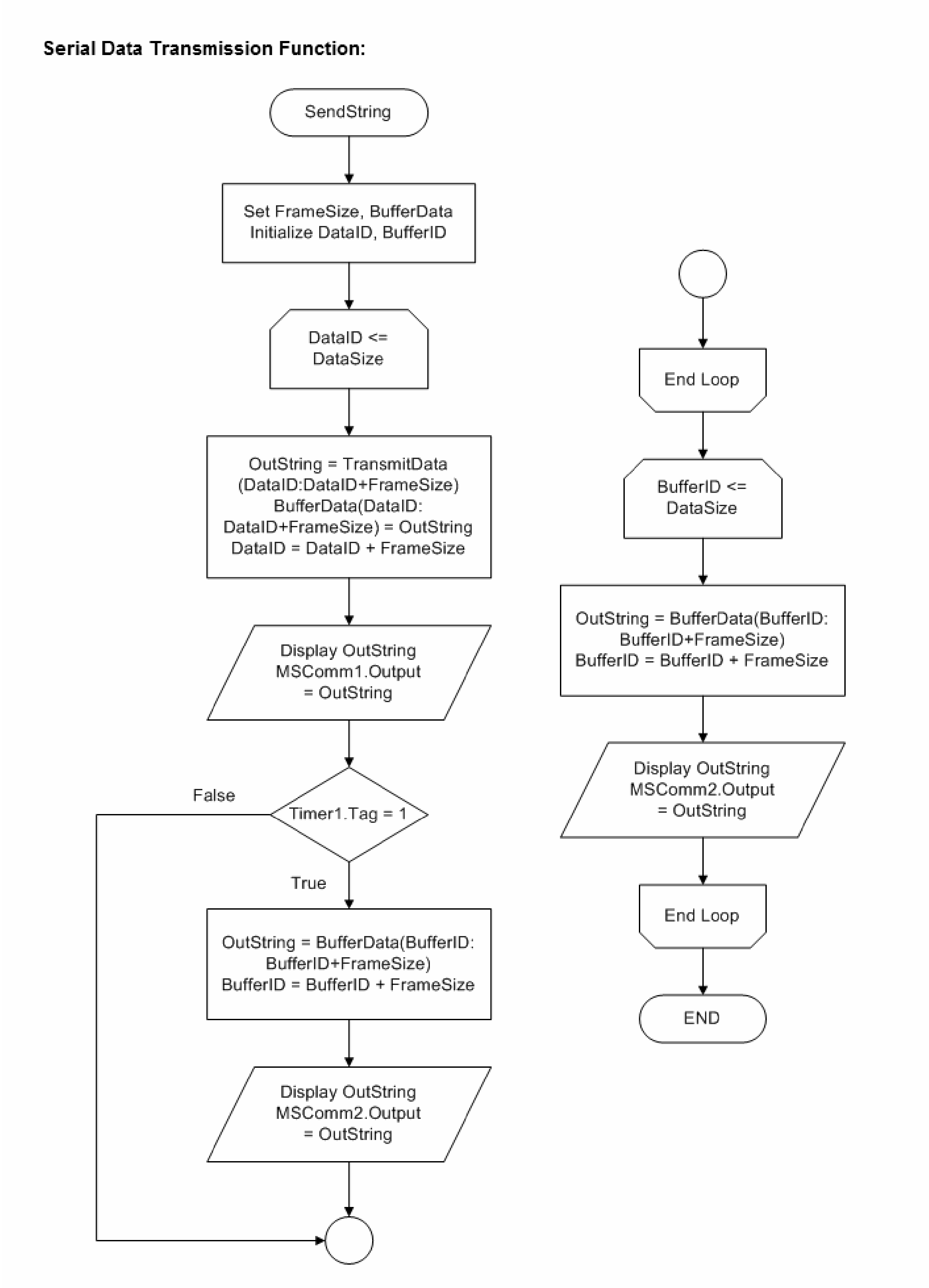

Figure 4.9: (cont.)

measured by comparing bit-by-bit between these files, similar to measurements made by a bit error rate tester (BERT). To control both systems from only one site, an

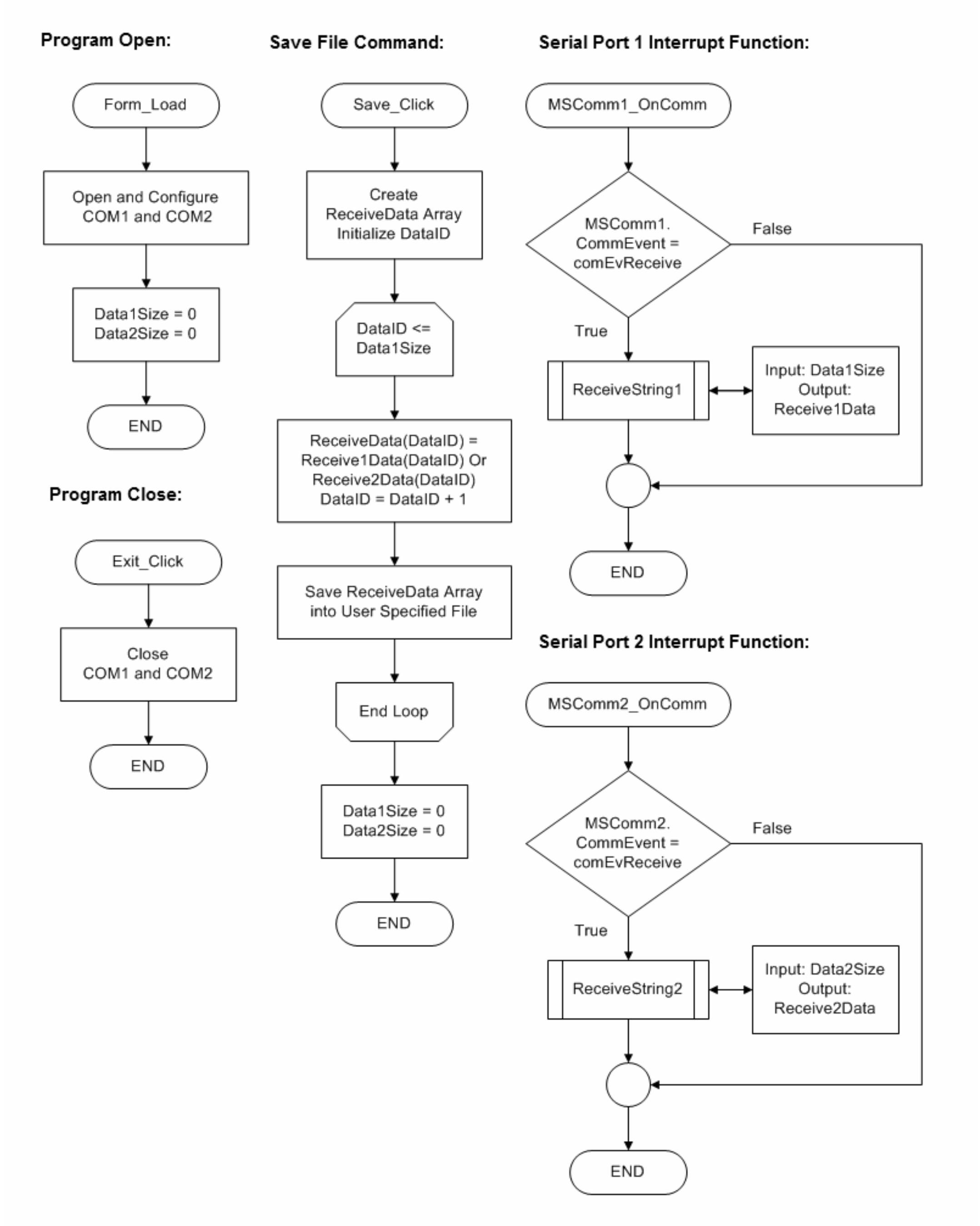

Figure 4.9: (cont.)

Ethernet based remote desktop connection is utilized using a directional radio frequency (RF) link to provide point-to-point connection between transmitter and receiver. The error data acquisition and measurement program was written using MatLab.

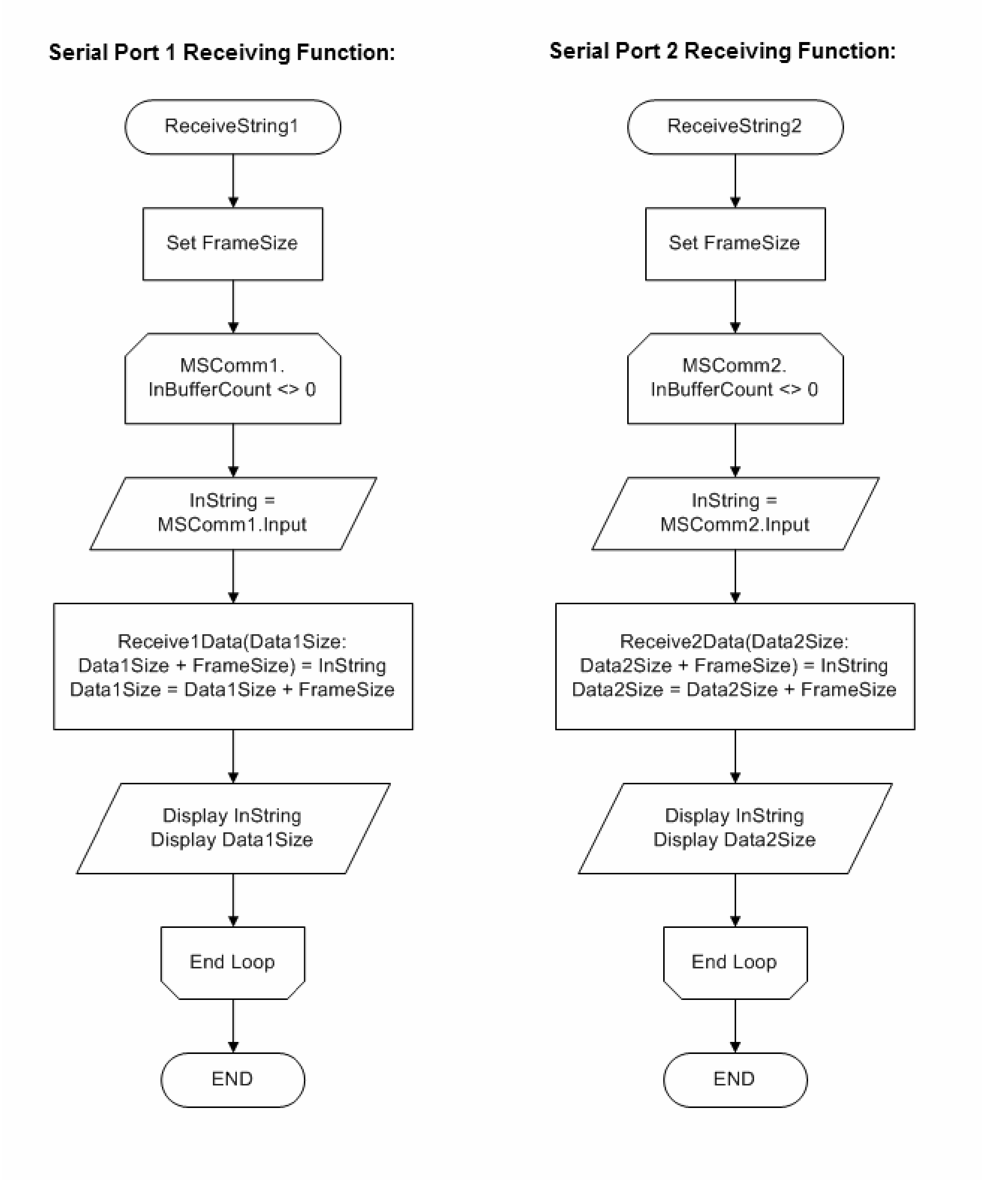

Figure 4.9: (cont.)

4.5 Results and Analysis for Clear Atmospheric Turbulence

To characterize the performance of our time delayed diversity FSO system; we first observe signal fluctuations induced by the turbulence across the link. We are mostly interested in investigating the crosstalk effects between the two laser polarizations. Only few experimental studies were conducted on this subject and they were typically limited by the sensitivity of the equipments [48,49]. Previous measurements of the same experimental site conducted by our group suggest that the polarization states are well preserved [2]. Fig. 4.10 shows typical examples of atmospheric polarization crosstalk observed using our FSO system. The results clearly confirm minimal crosstalk, although there are small amounts of fluctuation in the polarization ratio, which may be caused by geometrical and/or mechanical instability.

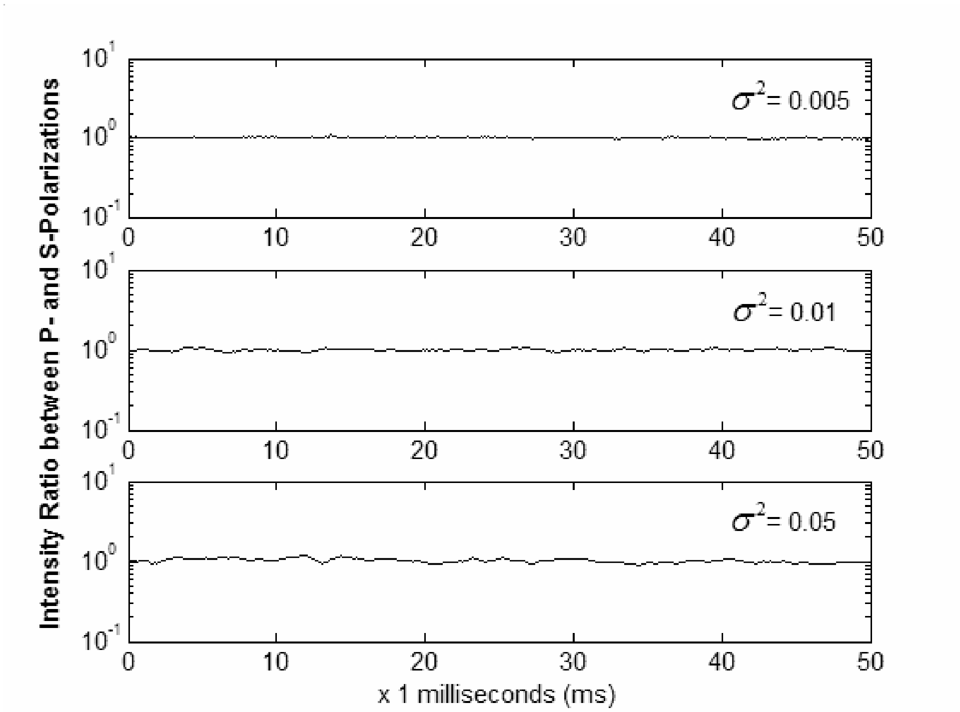

Figure 4.10: Measurements of intensity ratio of orthogonally polarized signals conducted for inter-building FSO link with $l = 785$ nm; $s^2 = 0.005$, 0.01, and 0.05.

In our laboratory experiment, turbulence induced scintillations can relatively easily be reproduced by setting the hot plates to the corresponding temperature control scale. However, this is not true in the atmospheric turbulence case. To fully characterize system performance, multiple measurements needed to be carried out for different parameters, which in our experiment were the delay periods and data rates.

Then, the results from similar intensity fluctuation conditions were compared, and they were characterized by the average intensity variance. Three sets of representative results are presented in this work with the average intensity variance values correspond to 0.01, 0.02, and 0.05. Fig. 4.11 illustrates the graphs of the average normalized covariance functions obtained from our experiment.

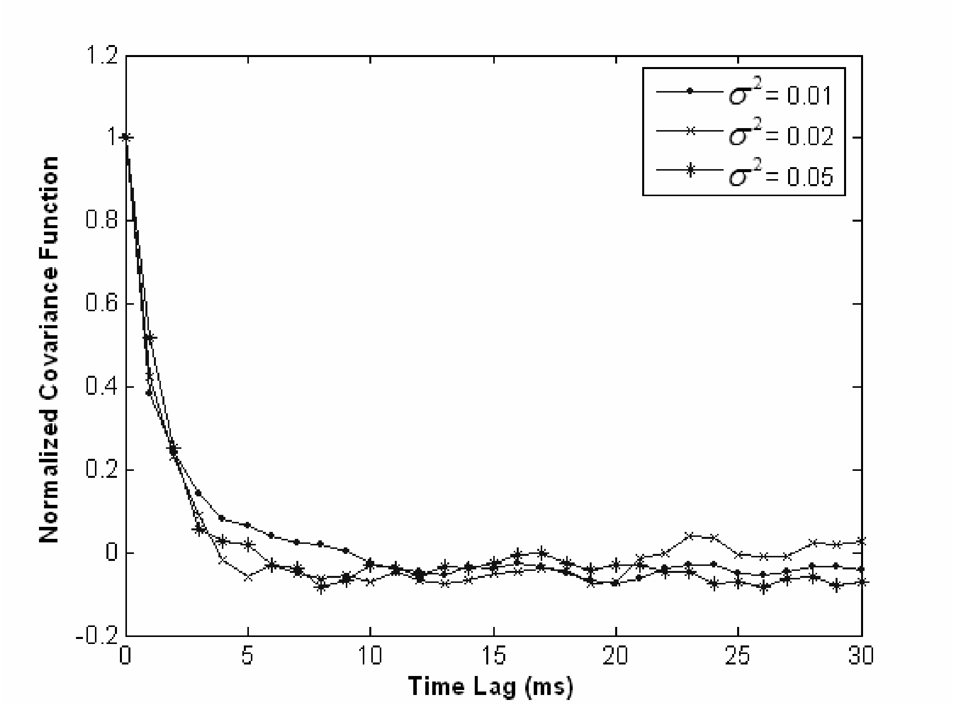

Figure 4.11: Temporal covariance functions of the atmospheric turbulence obtained from measurements made with $l = 785$ nm; $s^2 = 0.01$, 0.02, and 0.05.

Since the coherence times are not exactly known and will vary from time to time, we predetermined and used three different delay periods in our experiment: 5 ms, 10 ms, and 20 ms. The measurements were made for several different data rates from 1 to 10 Mbps, and the results for the average intensity variance of 0.01, 0.02, and 0.05 are represented in Figs. 4.12 to 4.14. The measured results for no diversity, no delay, 5 ms, 10 ms, and 20 ms periods are indicated by dots, asterisks, circles, triangles, and squares; respectively. Theoretical calculations for FSO link with no diversity and idealized dual diversity are also plotted to serve as performance limits.

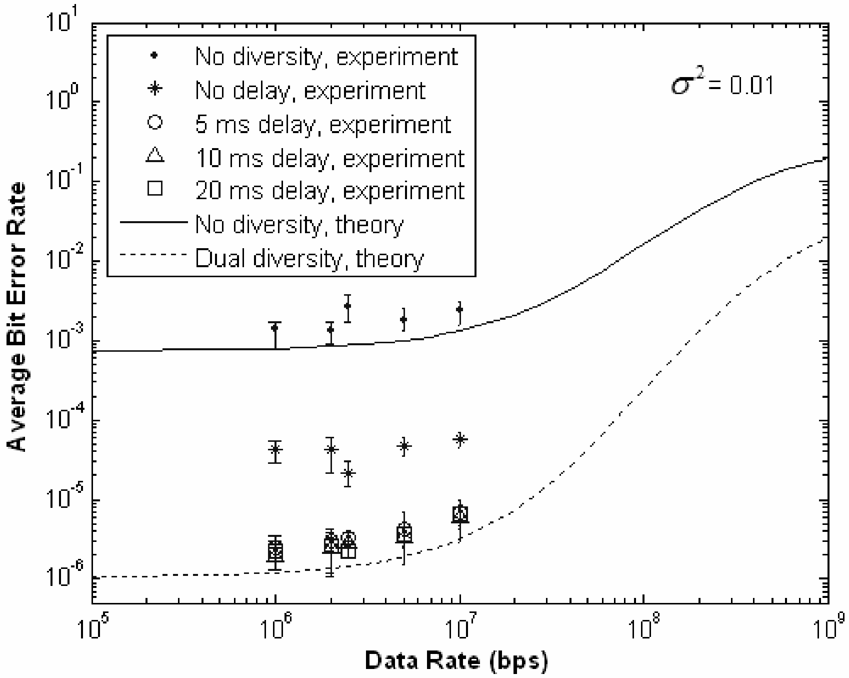

Figure 4.12: BER performance of time delayed diversity FSO system measured under clear atmospheric turbulence with $s^{2} = 0.01$, for the case of no diversity, no delay, $t = 5$ ms, 10 ms, and 20 ms. The theoretical curves were calculated from Eq. (3.48) for the case of no diversity and dual diversity with independent channels.

The experimental performance is quantified in terms of the BER improvement. Recall that for an on-off keying (OOK) modulated system with BER value of p_e, the SNR value Γ can be found by

$$\Gamma(p_e) = 8\left[\operatorname{erfc}^{-1}(2p_e)\right]^2, \tag{4.4}$$

where $x = \operatorname{erfc}^{-1}(y)$ is the inverse complimentary error function for *y*, and it satisfies $y = \operatorname{erfc}(x)$ for $0 \le y \le 2$ and $-\infty < x < \infty$. We define the SNR gain g (in dB) as

$$g = 20\log_{10}\left[\frac{\operatorname{erfc}^{-1}\left(2\left\langle \Pr(e)\right\rangle_{TDD}\right)}{\operatorname{erfc}^{-1}\left(2\left\langle \Pr(e)\right\rangle\right)}\right], \tag{4.5}$$

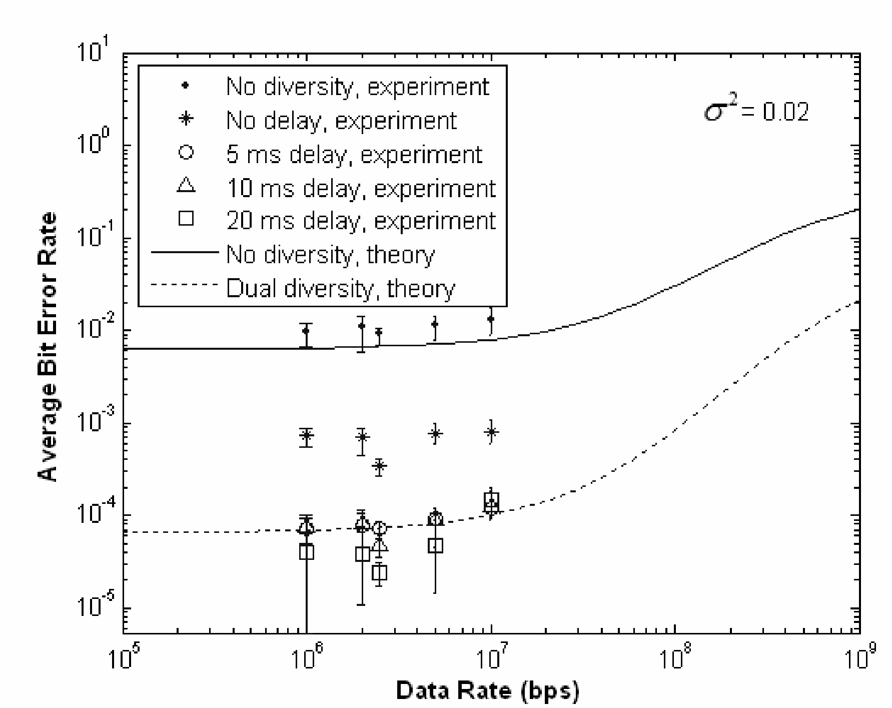

Figure 4.13: BER performance of time delayed diversity FSO system measured under clear atmospheric turbulence with $s^2 = 0.02$, for the case of no diversity, no delay, $t = 5$ ms, 10 ms, and 20 ms. The theoretical curves were calculated from Eq. (3.48) for the case of no diversity and dual diversity with independent channels.

where $\langle \Pr(e) \rangle$ and $\langle \Pr(e) \rangle_{TDD}$ are the average BER for no diversity and the time delayed diversity FSO system, respectively. In terms of this performance metric, the experimental system gives SNR gains of about 3.5 dB, 4.2 dB, and 4.7 dB for difference variance values. Compare to the computed theoretical SNR gains of 3.5 dB, 3.7 dB, and 4.2 dB; excellent agreement is found between the experimental and theoretical results. It suggests that optimum performance of a dual diversity system can be achieved using a time delayed diversity technique.

4.6 Polarization Modulation in Free Space Optical Communications

Polarization shift keying (PolSK) scheme has been studied and proposed as a possible improvement for optical communications, and shown to have 3 dB better sensitivity than an OOK scheme [50]. However, the birefringence of fiber optics causes the polarization state to alter and becomes difficult to track at the receiver, resulting in high complexity of the receiver [51]. In contrast, the atmospheric channel only causes negligible crosstalk between the polarization states, and they can be easily detected at the receiver. Experimental performance of PolSK and OOK modulations in FSO systems is presented.

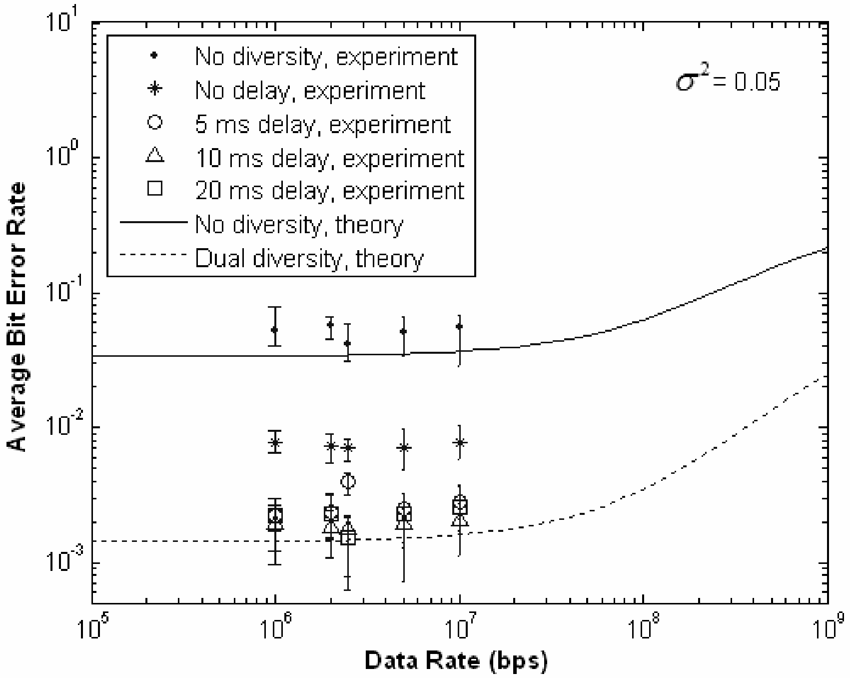

Figure 4.14: BER performance of time delayed diversity FSO system measured under clear atmospheric turbulence with $s^2 = 0.05$, for the case of no diversity, no delay, $t = 5$ ms, 10 ms, and 20 ms. The theoretical curves were calculated from Eq. (3.48) for the case of no diversity and dual diversity with independent channels.

4.6.1 Free Space Optical System using Binary Polarization Modulation

PolSK transmission encodes information on a constellation of signal points in the space of Stokes parameters. In general, each point corresponds to a given polarization state and a given power. If only the polarization of the light, and not its power, is modulated, all the signal points lie on the Poincaré sphere. A binary PolSK constellation is made up of two points that are antipodal over this sphere. The optical field at the transmitter output of a binary system can be written as

$$\mathbf{U}_T \propto \sqrt{P_T}\begin{bmatrix} \vec{\mathbf{e}}_{\|} \\ \vec{\mathbf{e}}_{\perp} \end{bmatrix}, \tag{4.6}$$

where P_T is the transmitted optical power, $\vec{\mathbf{e}}_{\|}$ and $\vec{\mathbf{e}}_{\perp}$ represent the components of the signal in P- and S-polarizations respectively.

At the receiver, the optical signal after the receiver aperture may be expressed as

$$\mathbf{U}_R \propto \sqrt{G_T P_T}\begin{bmatrix} \vec{\mathbf{e}}_{\|} \\ \vec{\mathbf{e}}_{\perp} \end{bmatrix} = \sqrt{P_R}\begin{bmatrix} \vec{\mathbf{e}}_{\|} \\ \vec{\mathbf{e}}_{\perp} \end{bmatrix}, \tag{4.7}$$

where G_T is the total power loss occurred along the FSO link, and P_R is the received optical power. The received signal passed through a PBS, which separates the two linear P- and S-polarizations. These signals are subsequently detected by two photodetectors resulting in signal currents i_P and i_S given by

$$\begin{aligned} i_P &= \Re P_R \left|\vec{\mathbf{e}}_{\|}\right|^2 + i_{N,1}, \\ i_S &= \Re P_R \left|\vec{\mathbf{e}}_{\perp}\right|^2 + i_{N,2}, \end{aligned} \tag{4.8}$$

where $i_{N,1}$ and $i_{N,2}$ are the total noises contributing in the detection process. To recover the information, these two signals are subtracted and the result is compared to the signal constellation mapping.

4.6.2 Experimental Results and Analysis

An experiment to investigate the performance of PolSK modulated FSO system had been conducted using our laboratory convective turbulence setup. In this setup, only two orthogonal polarizations are utilized for modulation while the optical power remains constant (i.e. binary PolSK). The ‘one’ and ‘zero’ bits are coded by P- and S-polarizations of the transmitted light. At the receiver, the received optical beam is split into P- and S-polarized lights by a PBS and independently detected. The demodulator compares the two detected signals, and chooses ‘one’ if the S-polarization is smaller than the P-polarization, and ‘zero’ otherwise. This system can easily be implemented using our time delayed diversity system by sending bit ‘one’ in the prompt path and bit ‘zero’ in the delayed path with no delay.

The performance of the PolSK modulated FSO system is shown in Fig. 4.15. Our experimental results show on average 2.2 dB performance improvement of PolSK system over OOK modulated FSO system. As in the optical fiber communication systems, PolSK provides better performance than OOK scheme [51]. Moreover, multilevel PolSK scheme brings the possibility of transmitting more than one bit per symbol. This is not only helpful in increasing the spectral efficiency, but also reducing the symbol rate, and thus the cost of high-speed electronics. Together with its simplicity of implementation, PolSK could become a possible option as a standard modulation scheme in FSO communication systems.

4.7 Summary

We have presented the experimental performance of a time delayed diversity system and shown a notable BER improvement compared to non-diversity FSO system. Although, the system may suffer a 3 dB power penalty for dividing the transmitted power into two channels, our simulated convective turbulence experiment suggests that a performance improvement of up to 4.6 dB can be obtained. These experimental studies confirmed the usefulness of time delayed diversity technique to mitigate the effects of fading induced by turbulence. Moreover, the experiment also showed the validity of hot-plate generated turbulence as a simple and inexpensive method to emulate the effects of atmospheric turbulence for investigating the performance of FSO systems.

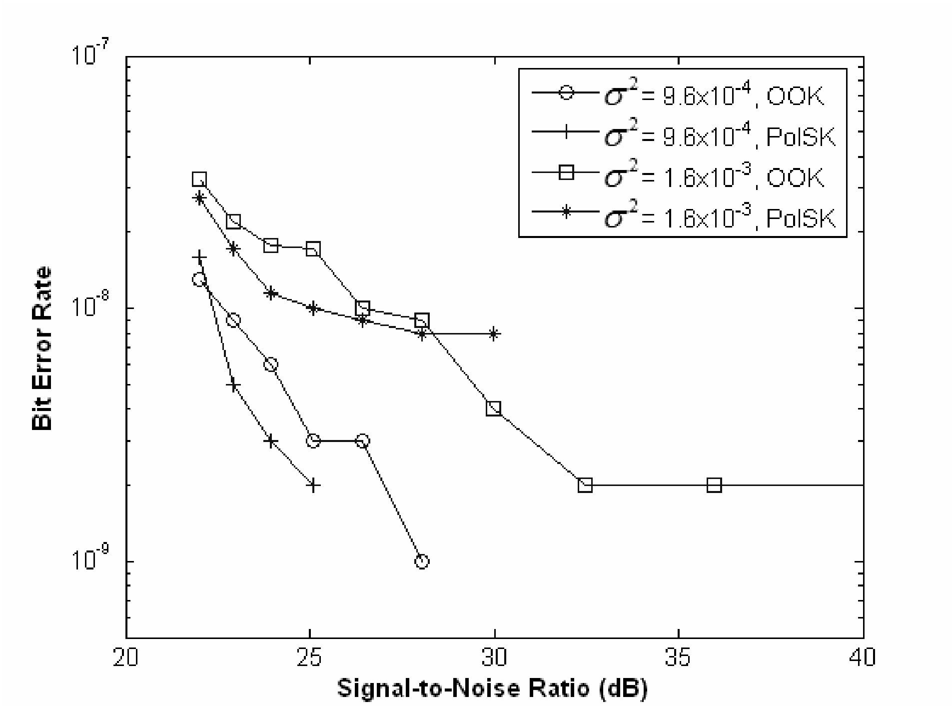

Figure 4.15: Performance comparison between OOK and PolSK FSO system measured under convective turbulence with $s^2 = 9.6\times10^{-4}$ and 1.6×10^{-3}.

The performance of time delayed diversity system under clear atmospheric turbulence conditions was also investigated. Measurements of the atmospheric polarization crosstalk at the experimental site suggest that the polarization states of light are preserved; hence the utilization of time delayed diversity. In terms of BER performance, the experimental time delayed diversity system doubles the BER of non-diversity FSO system. It suggests that time delayed diversity reaches the ideal performance of a dual diversity system. We have also shown that PolSK modulation is simpler to be implemented in FSO systems. Furthermore, in turbulence conditions, it can give better performance compared to OOK modulation. This suggests possible performance improvements of time delayed diversity systems, if the transmitted signal can indeed be made PolSK modulated.

Chapter 5: Omnidirectionality in Free Space Optical Communications

5.1 Diffuse and Line-of-Sight Transmissions

Non-directed optical links, which do not require precise alignment between transmitter and receiver, can be categorized as either line-of-sight (LOS) or diffuse. A LOS link requires an unobstructed path in order to get reliable communication, whereas a diffuse link relies instead upon diffuse reflections from various surfaces. The two types of links are illustrated in Fig. 5.1. The dominant source of noise in a non-directed link is background light, which is typically a combination of fluorescent light, sunlight, and incandescent light. The background light produces significant shot noise in the photodetector and can be quite intense, which could decrease the receiver signal-to-noise ratio (SNR) by 25 dB or more [27].

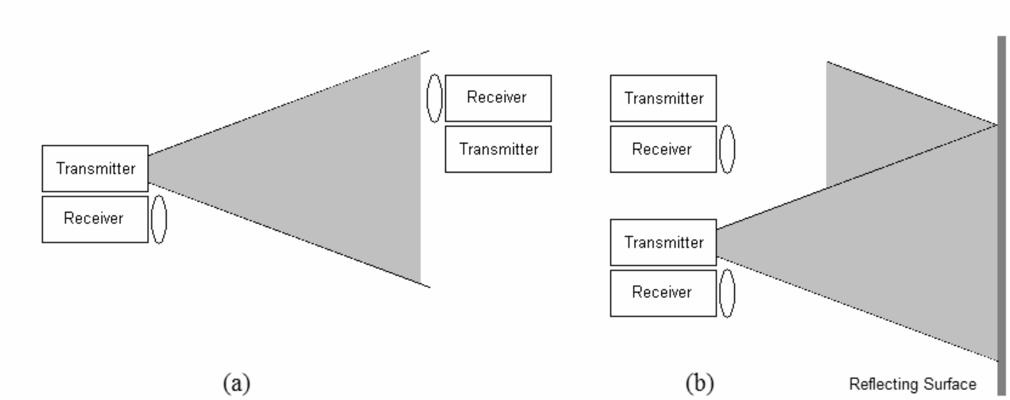

Figure 5.1: Two types of non-directed optical links: (a) LOS, and (b) diffuse.

Diffuse links are mostly appropriate for indoor wireless infrared communications, since they exploit the excellent reflective properties of most indoor environments. Reflectivity measurements of typical office materials, such as painted surfaces, wood, carpets, and plaster walls, show that about 40% to 90% infrared power is available after reflections [52]. Furthermore, these surfaces are well approximated by an ideal Lambertian reflector, so that the incident infrared energy will be reradiated in all directions. Although there is no multipath fading, the multipath optical propagation does produce dispersion and increases the duration of the channel impulse response, thus reducing the bandwidth. It is shown that in systems with field-of-view (FOV) close to 90°, the channel bandwidth is limited to 37 MHz [53].

On the other hand, the non-directed LOS makes better use of signal power than the diffuse link. This configuration may find use in high speed and long distance applications, for which the energy transfer in the diffused link is insufficient. Our LOS approach for non-directed free space optical (FSO) communications is using omnidirectionality [19]. In this system, the transmitter consists of an array of moderately wide directed beams, such that the combined effect is an omnidirectional optical beam. Similarly the receiver consists of an array of detectors looking in different direction, such that the total effect is a wide FOV receiver. In FSO communications, in practice only the LOS approach is feasible since reflecting surfaces are not necessarily available in outdoor environments.

5.2 Theoretical Analysis of Omnidirectional Systems

In omnidirectional FSO, the transmitters typically use large angle beam divergence to provide inter-node communication capability that requires no pointing. In contrast to infrared data association (IrDA), which is only intended for very short-range, low data rate exchange using incoherent infrared light, an omnidirectional FSO system can potentially be used for moderately long-range communication in FSO networks applications. For understanding various system design issues, theoretical modeling of the omnidirectional FSO link and transceiver is required. Subsequently, the potential range and data rates of these systems can be analyzed in various performance scenarios.

5.2.1 Omnidirectional Optical Link Analysis

The transmitter of the optical link being analyzed is assumed to have power P and emit its power with an angular intensity pattern $I(q,f)$. The total power through a hemisphere can be written as

$$P = \int_{0}^{2p} \int_{0}^{p/2} I(q,f) \sin q \, dq \, df \ . \tag{5.1}$$

For a point source that emits uniformly into a hemisphere $I(q,f) = P/2p$. For a Gaussian beam of small divergence angle the intensity distribution is usually written in a radial format as in Eq. (2.6). For a highly divergent Gaussian beam an appropriate angular intensity distributions I is written as

$$I(q,f) = \frac{2P\cos q}{pw^{2}} \exp\left(-\frac{2\sin^{2} q}{\sin^{2} q_{B}} \right), \tag{5.2}$$

where w and q_B are the beam spot size and the half angle beam divergence given in Eqs. (2.3) and (2.5), respectively. The intensity of an azimuthally symmetric beam on axis is

$$I(q = 0) = \frac{2P}{pw^2}\,. \tag{5.3}$$

To provide omnidirectionality coverage over a full sphere requires a number of transmitters. If each transmitter is assumed to provide axisymmetric intensity, then the solid angle Ω covered by each transmitter is

$$\Omega(q_B) = 2p\,(1 - \cos q_B)\,. \tag{5.4}$$

The number of transmitter N required to cover a full sphere, in this case, is $N = 4p/\Omega(q_B)$. However, this mode of operation will not provide very smooth overlap of illumination over the surface of a sphere. This may require operation with transmitter angular spacing of $q_B/2$, necessarily resulting in more transmitters. Fig. 5.2 shows the number of transmitters required in each case for different beam divergence angles. It is of course possible to use a beam splitter arrangement inside the transceiver to multiply up the number of directions that can be interrogated by each transmitter.

Also note that the solid angle of the transmitted beam causes additional FSO loss due to beam divergence. Recall that FSO loss L_{FSO} is given by

$$L_{FSO} = \frac{A}{p\,w^2} \cong \frac{D^2}{4q_B^2 L^2}\,, \tag{5.5}$$

where A is the receiver aperture area with diameter D, and L is the operating range. Fig. 5.3 illustrates the FSO loss in dB experienced by omnidirectional FSO systems.

To get a comparable performance to directional FSO systems, omnidirectional systems require additional link margin ranges from 40 to 60 dB, depending on the transmitted beam solid angle. It also implies that for the same optical power, the operating range of omnidirectional links may decrease by three orders of magnitude.

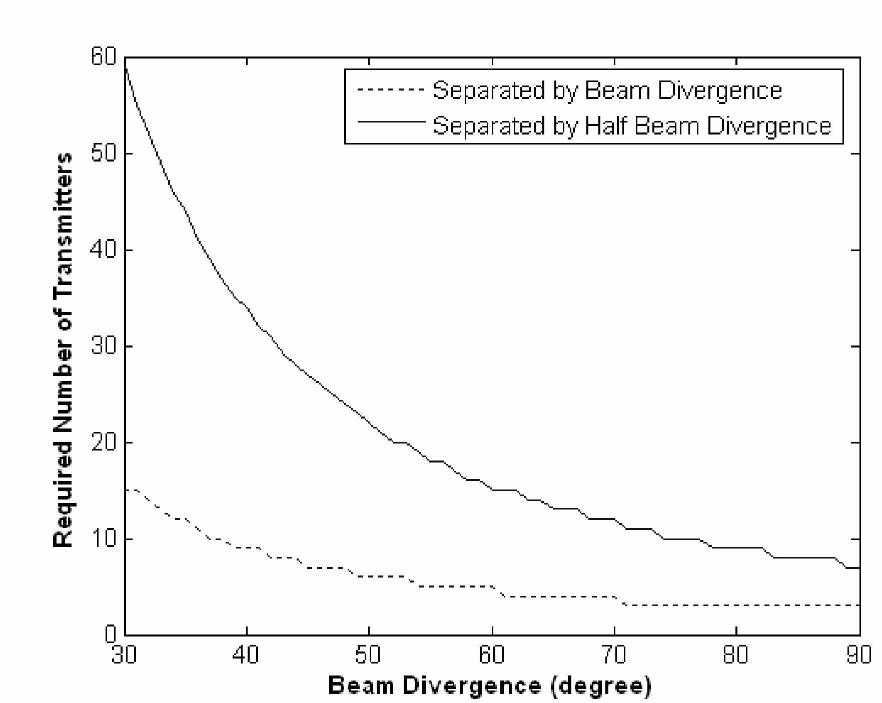

Figure 5.2: Number of required transmitters for spherical omnidirectional coverage calculated for angular separations at full and half beam divergence.

5.2.2 Modeling of Omnidirectional Receivers

Let us assume that each photodetector in an omnidirectional receiver has narrow enough FOV such that it can only receive signal from one laser source. This is particularly true for FSO applications, since there are no significant multipath effects encountered. Since turbulence will not be considered in this analysis, the performance of an ideal omnidirectional link can be calculated based on a consideration of the power received at a given range. For a transmitted power P_T emitting uniformly over a solid angle Ω, the power received P_R at range L by a receiver with received area A is given by

$$P_R = \frac{P_T A}{\Omega L^2}. \tag{5.6}$$

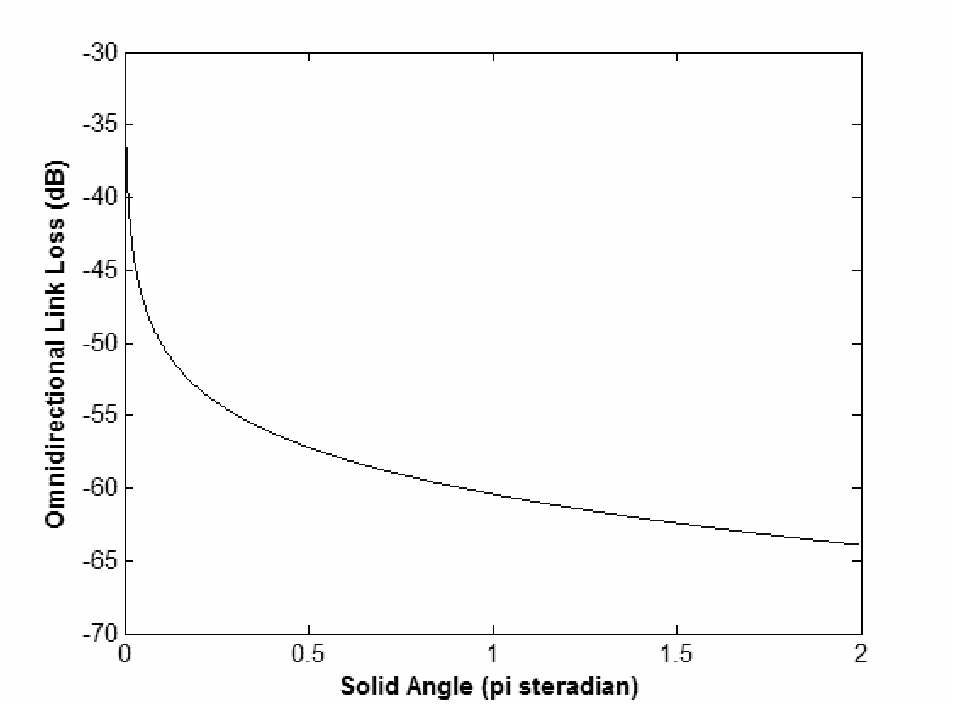

Figure 5.3: FSO loss experienced in omnnidirectional links calculated from Eq. (5.5) for system having optimum performance at $q_B = 1$ mrad.

The photocurrent produced in the receiver is given by $i_S = \Re P_R$. The contributing noise terms are shot noise resulting from both signal and background radiation, and Johnson noise. For an omnidirectional receiver with a number of N detectors, the output signal can be obtained using a post-detection combining method. Assuming that background illumination can be removed by means of band pass optical filters, the effective SNR of omnidirectional receiver Γ can be written as

$$\Gamma = \frac{i_S^2}{2qi_S\Delta f + 4kTN\Delta f / R}. \tag{5.7}$$

The ideal receiver would be shot noise limited, and for practical values of *N* the SNR is given by

$$\Gamma_{SNL} = \frac{\Re P_R}{2q\Delta f}\,. \tag{5.8}$$

However, a more realistic scenario would involve a Johnson noise limited receiver, in which case

$$\Gamma_{JNL} = \frac{\Re^2 P_R^2 R}{4kTN\Delta f}\,. \tag{5.9}$$

5.2.3 Theoretical Performance of Omnidirectional Systems

The performance of an omnidirectional FSO transceiver was calculated for the following transceiver specifications, which are close to those used in our prototype experiments: $A = p\,D^2/4$ (with $D = 10$ mm) and $\Omega = p/2$ sr; for transmitted powers of 1 mW, 10 mW, and 100 mW. The performance was simulated using the following scenarios: shot noise limited, Johnson noise limited, and receiver sensitivities of –35 dBm and –45 dBm, for bandwidths of 1 kHz and 1 MHz. The shot noise and Johnson noise limit are given for a received power ten times above the value that gives an SNR of 1. This corresponds to performance of 10 photons/bit. For an on-off keying (OOK) system, a bit rate of R_b bps would require a bandwidth $\Delta f = R_b$.

We believe that our simulations provide a realistic picture of the performance of an omnidirectional FSO transceiver system in both a realistic scenario and for an optimized receiver. Figs. 5.4 and 5.5 show the received power as a function of range for transmitted powers of 1 mW, 10 mW, and 100 mW. The horizontal lines show the limiting performance for different scenarios, namely: –35 dBm receiver sensitivity,

–45 dBm receiver sensitivity, Johnson noise limited, and shot noise limited; calculated for bandwidths of 1 kHz and 1 MHz, respectively. These results show that without high performance, close to shot noise limited receivers, operational ranges with $p/2$ sr omnidirectional transmitters are limited to not much above 10 m.

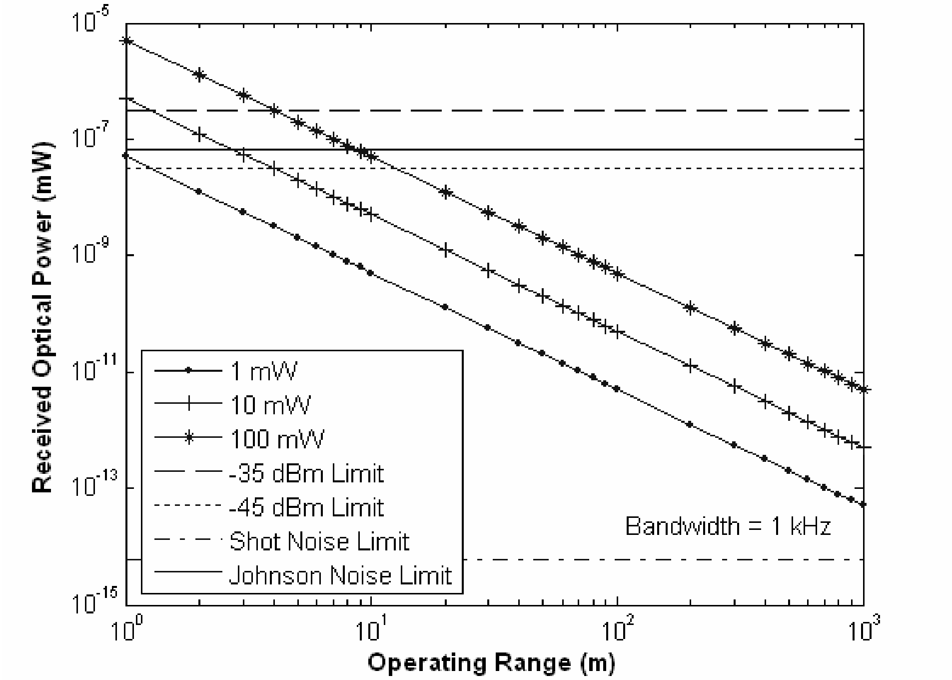

Figure 5.4: Optical power received by omnidirectional receiver with –35 dBm, –45 dBm, shot noise, and Johnson noise limit performance; calculated for $\Delta f = 1$ kHz and $P_T = 1$ mW, 10 mW, and 100 mW.

Figs. 5.6 and 5.7 show these results in terms of the SNR at various ranges for bandwidths of 1 kHz and 1 MHZ, respectively. These SNR curves are computed for transmitted optical powers of 1 mW, 10 mW, and 100 mW. The upper three curves in each case are SNR performance for shot noise limited operation. The horizontal line represents the SNR of 141, which corresponds to a minimum acceptable operational value resulting in a bit error rate (BER) of 10^{-9}. Our simulations have not included any additional SNR that could be gained by appropriate data coding.

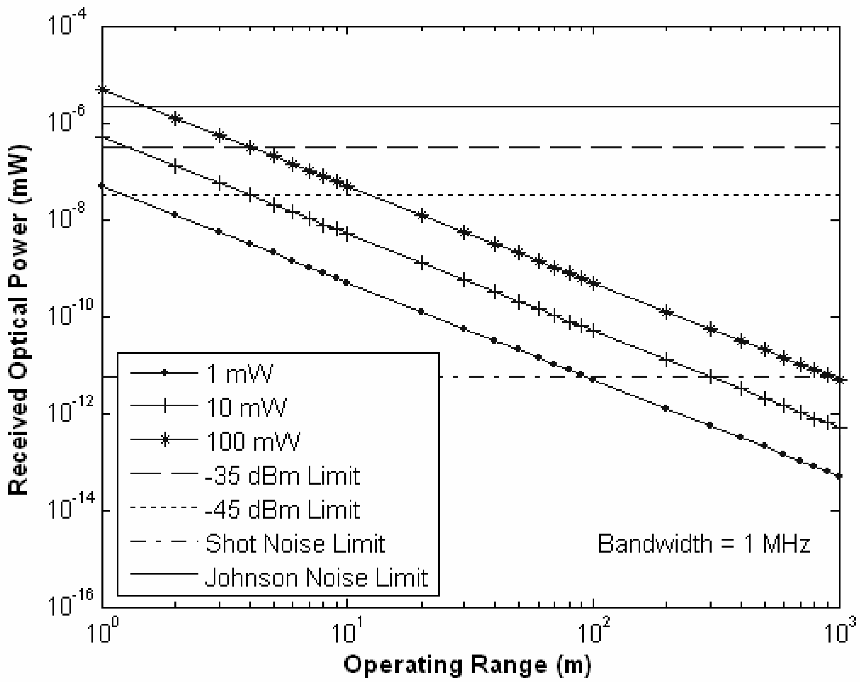

Figure 5.5: Optical power received by omnidirectional receiver with –35 dBm, –45 dBm, shot noise, and Johnson noise limit performance; calculated for $\Delta f = 1$ MHz and $P_T = 1$ mW, 10 mW, and 100 mW.

5.3 Beam Forming Optics and Optical Filters

Two types of optical front-end are needed in omnidirectional transceiver design, one to provide a wide divergence transmitted beam and another to mitigate the effects of received background light. In our design, omnidirectionality is provided using concave lenses, since they do not alter the nature of the beam while increase the divergence of the beam. An alternative approach is to use compound parabolic concentrators (CPCs) as non-imaging beam forming optics [54]. At the receiver, narrow-band optical filters are used to reject out-of-band ambient light. The angle dependent performance of thin film optical filters, which is critical in wide FOV applications, is explored.

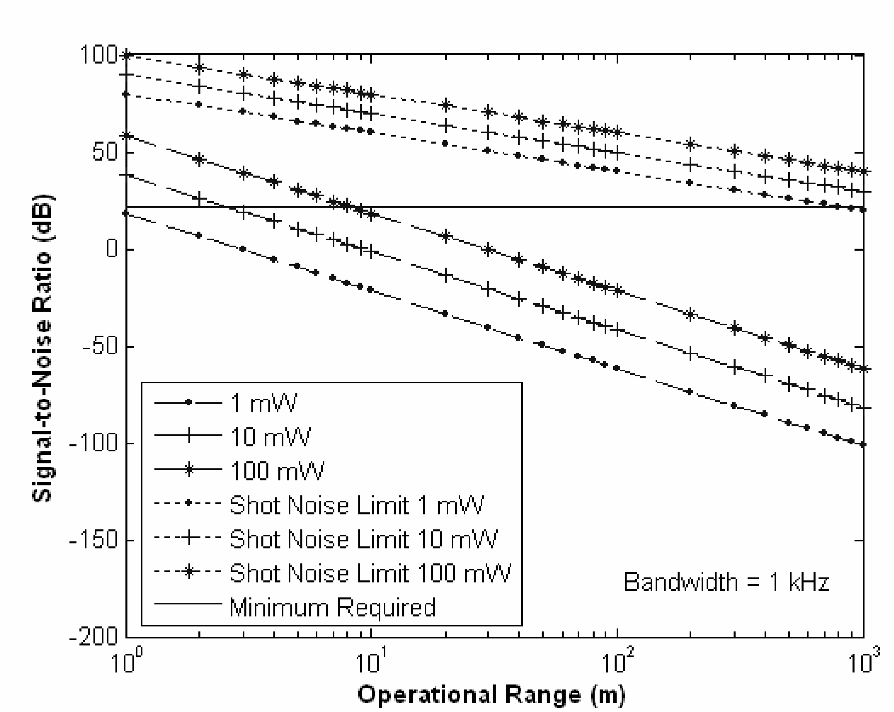

Figure 5.6: SNR performance calculated for $P_T = 1$ mW, 10 mW, and 100 mW, under practical and ideal shot noise limited receivers, for $\Delta f = 1$ kHz. The horizontal line depicts the operational SNR value corresponds to a BER of 10^{-9}.

5.3.1 Gaussian Beam Transformation by Lens

A lens can be used either to focus or expand a laser beam. In an ideal thin lens, the transverse mode beam intensity pattern will not be changed, and only the radius of curvature of the phase fronts of the beam is altered. Lenses that tend to expand the light are called concave, divergent, or negative lenses. These lenses have a negative dioptric power *F*, or equivalently a negative focal length $f = 1/F$, given by

$$F = (n-1)\left(\frac{1}{R_1} - \frac{1}{R_2}\right), \tag{5.10}$$

where R_1 and R_2 are the radius of curvature of the front and back surfaces of the lens, and *n* is refractive index of the lens material.

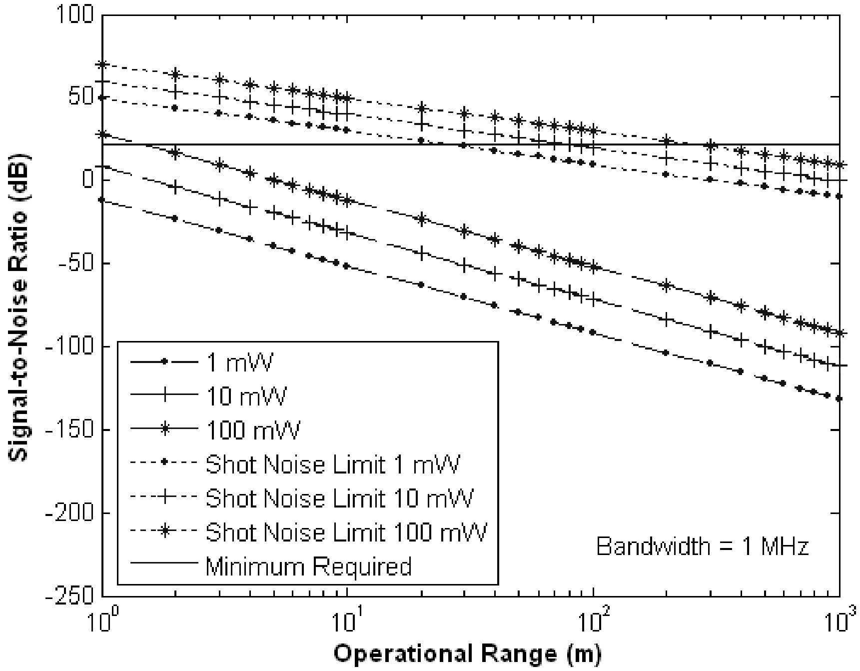

Figure 5.7: SNR performance calculated for $P_T = 1$ mW, 10 mW, and 100 mW, under practical and ideal shot noise limited receivers, for $\Delta f = 1$ MHz. The horizontal line depicts the operational SNR value corresponds to a BER of 10^{-9}.

A concave lens can be used to increase the divergence of the light arriving from an object plane to form a wider image on an image plane. The relation of object distance l_1, image distance l_2, and focal length *f*, is given by a fundamental imaging equation

$$\frac{1}{l_1}+\frac{1}{l_2}=\frac{1}{f}\,. \tag{5.11}$$

For Gaussian beams, an analogous formula can be obtained by assuming that the waist of the input beam represents the object, and the waist of the output beam represents the image. Thus, the modified lens equation can be written as [55]

$$\frac{1}{l_1+z_R^2\big/\left(l_1-f\right)}+\frac{1}{l_2}=\frac{1}{f}, \tag{5.12}$$

where $z_R = p\,w_0^2 / l$ is the Rayleigh range of the input beam.

The location of the new beamwaist l_2 and the spot size w_2 of the output Gaussian beam can be determined as

$$l_2 = \frac{f}{1+\left(l\,f / p\,w_0^2\right)^2}, \tag{5.13}$$

and

$$w_2 = \frac{l\,f / p\,w_0}{\sqrt{1+\left(l\,f / p\,w_0^2\right)^2}}. \tag{5.14}$$

In the frequent case of $l\,f / p\,w_0^2 \ll 1$, they can be simplified to give $l_2 \cong f$ and $w_2 \cong f q_B$. Fig. 5.8 illustrates the diagram of this optical configuration. The laser beam will appear to be expanding from a virtual source placed at distance *f* behind the lens, and the output beam divergence $q_{B,\,out}$ can be computed from Eqs. (5.13) and (5.14). If the incident beam waist exceeds the lens dimension, then the finite size of the lens with radius *r* would determine the approximate output divergence, i.e.

$$q_{B,\,out} \simeq \tan^{-1}\left(\frac{r}{f}\right). \tag{5.15}$$

5.3.2 Non-imaging Concentrators

Although we have used imaging optics in our prototype system, the use of non-imaging optics such as CPCs is also analyzed as possible improvements in beam diverging optics. The CPC is an extension of the basic cone concentrator. A concentrator is a device whose main purpose is to increase the power density of radiation. It works by collecting rays over its entrance (larger) aperture and concentrating them over an exit (smaller) aperture, but with a concomitant increase in angular range. The cone concentrator is limited in its performance, because some rays are reflected back through the entrance aperture.

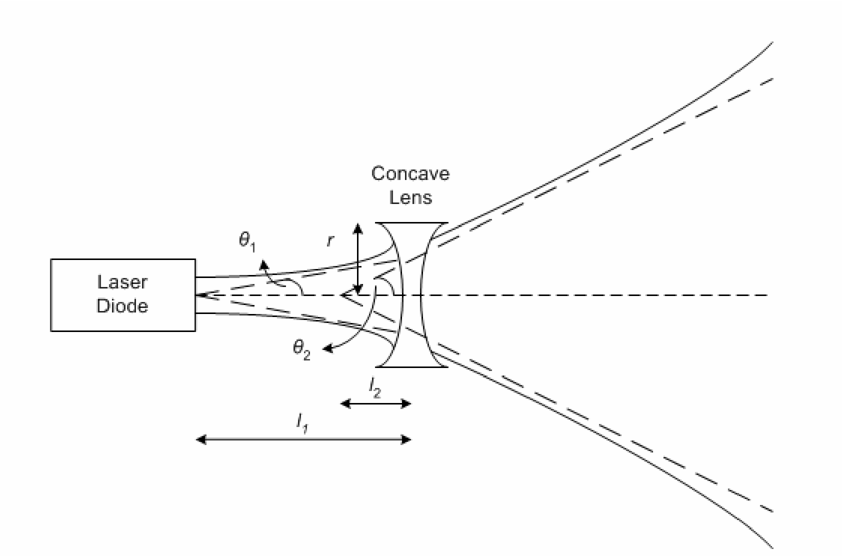

Figure 5.8: Diagram of a Gaussian beam transformed by a concave lens.

A CPC uses surfaces traced out by an off-axis parabola to address this problem [54]. The input rays that can be collected by the CPC are limited by maximum input angle q_i. This angle is related to the radius of entrance and exit apertures, a_{in} and a_{out}, by

$$\frac{a_{in}}{a_{out}} = \frac{1}{\sin(q_i)}. \tag{5.16}$$

The focal length *f* of the parabola and the length of the concentrator *L* are given by

$$f = a_{out}\left[1+\sin(q_i)\right], \tag{5.17}$$

and

$$L = \frac{2f\cos(q_i)}{1-\cos(2q_i)} = (a_{in}+a_{out})\cot(q_i). \tag{5.18}$$

Thus, the design of a CPC is completely determined by the entrance aperture a_{in}, and maximum input angle q_i. When a light beam enters a CPC with an angle less than q_i, the output beam will be diverged over a solid angle up to $2p$ sr. Fig. 5.9 illustrates the operation of CPC as beam diverging optical front-end.

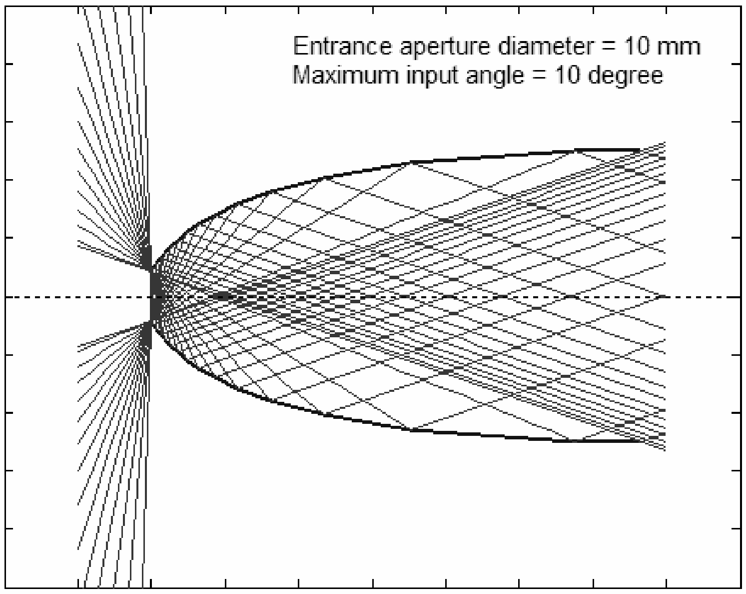

Figure 5.9: Example of rays entering and then expanding from the back of a CPC.

The concentration ratio is defined as the ratio of the area of input beam divided by the area of the output beam, which the maximum value $C_{\max}$ is

$$C_{\max} = \frac{1}{\sin^2(q_i)}. \tag{5.19}$$

In the case of a 2-dimensional (2-D) CPC, no rays inside the maximum collecting angle are turned back and the concentrator achieves its theoretical limit. This is not the case with a 3-D CPC constructed by rotating the 2-D profile about the axis of symmetry. The 3-D concentrator is a figure of revolution and some skew rays are turned back by multiple reflections inside the CPC. This results in the non-maximal concentration ratio of 3-D CPC, hence decreases the laser power transmission.

While it seems that CPCs are interesting solution for beam diverging optics, it is not a trivial task to customize their design. Their apertures, maximum angle, size, and concentration ratio need to be optimized when designing these devices. Table 5.1 summarizes the parameters of several CPCs with exit apertures range from 0.1 to 2 mm and fixed 5 mm entrance aperture. It is obvious that trade-offs need to be made between size and concentration performance. For example for a CPC with $q_i = 1.15^\circ$, the length of approximately 255 mm is considerable, making it impractical for our omnidirectional FSO system. Furthermore, their availability and cost of manufacturing are other factors that also need to be considered.

Table 5.1: Design parameters and performance of various CPCs.

Exit Aperture (mm)	Input Angle	Length of CPC (mm)	Logarithm of $C_{\max}$
0.1	1.15°	254.95	3.4
0.5	5.74°	54.72	2
1	11.54°	29.39	1.4
1.3	15.07°	23.4	1.17
1.7	19.88°	18.53	0.94
2	23.58°	16.04	0.8

5.3.3 Thin Film Interference Filters

In combination with narrow band optical sources, such as laser diodes, filters with narrow optical bandwidths are desirable to mitigate the effects of background light. An efficient narrow-band optical filter can be made using multiple layers of thin dielectric films. A thin film filter consists of a stack of thin dielectric slabs with varying indices of refraction. By carefully adjusting the slabs thickness and their indices of refraction, a constructive interference at the desired wavelength can be obtained while other wavelengths are suppressed. With this interference filter, narrow pass band (on the order of 10 nm) and high transmittance (typically 40% to 90%) can be obtained.

The basic building block of a thin film interference filter is the Fabry-Perot filter, which is in turn based on the Fabry-Perot interferometer [56]. A typical Fabry-Perot interferometer consists of a pair of highly reflective parallel mirrors that are facing each other and spaced at distance *d*. The transmission characteristic *T* is given by

$$T = \frac{1}{1 + 4R\big/(1-R)^2 \sin^2\left(d/2\right)}, \tag{5.20}$$

where *R* is the mirror reflectivity, and $d = 4p\, d \cos\left(q\right)\big/ l$ with l is the wavelength in the material between the reflectors and q is the incidence angle. At normal incidence, the interferometer acts as a comb filter with a series of passband at wavelengths equal to $2d/m$ for all integers *m*.

The thin film all dielectric Fabry-Perot filter can be visualized as a Fabry-Perot interferometer with the mirrors replaced by distributed reflectors consisting of a stack of high and low index dielectrics, each a quarter wave thick with respect to a design wavelength l_0. To achieve narrow optical bandwidths below 100 nm, two or more Fabry-Perot filters are typically coupled together [57]. Unfortunately, the phase shift through the layer changes with angle of incidence, causing dramatic changes in the filter characteristics at non-normal incidence. This effect may be disadvantageous for optical wireless communications applications [24,27].

The shift in the center wavelength l of the transmission pass band for angle of incidence q can be approximated by [27]

$$l(q) = l_0\sqrt{1-\left(\frac{n_1}{n_E}\right)^2 \sin^2(q)}\,, \tag{5.21}$$

where n_1 is the index of input layer and n_E is the effective index of the filter medium. Fig. 5.10 shows the fractional center wavelength shift l/l_0 for an interference filter with $n_E = 2.05$. Observe that as the angle of incidence increases, the center wavelength decreases; hence the detected signal power is reduced. This provides an additional motivation for using an array of narrow FOV receivers instead of one with a wide FOV.

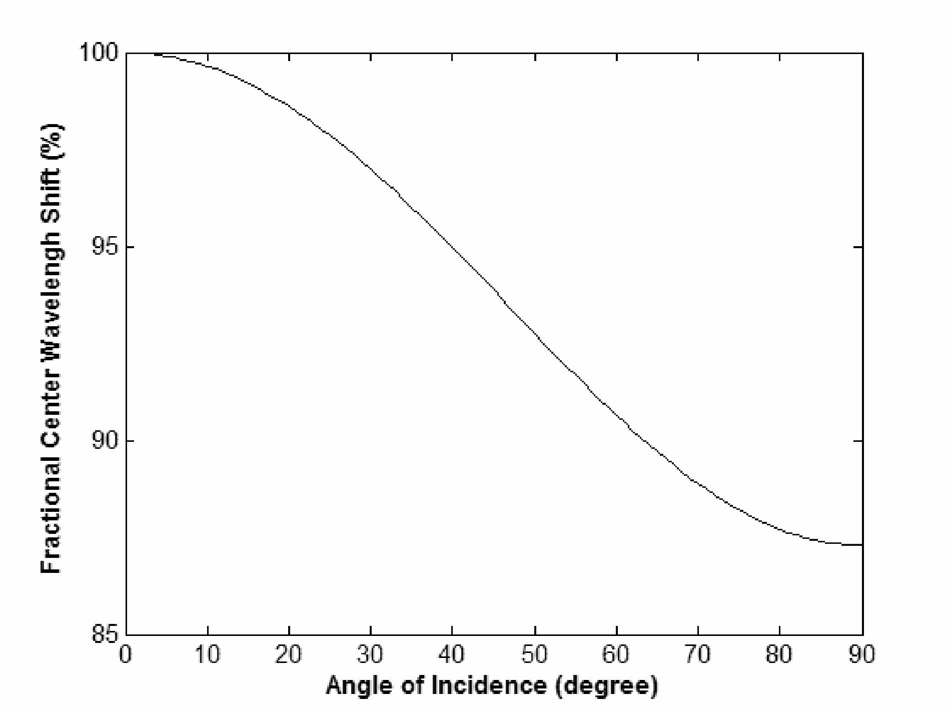

Figure 5.10: Dependence of transmission wavelength on light incidence angle calculated from Eq. (5.21) for a thin film interference filter with $n_E = 2.05$.

5.4 Construction of Omnidirectional Free Space Optical System

Prototype experimental systems of omnidirectional FSO transceivers, specifically those with relatively low data rate performance for potential use in covert deployable sensor networks, have been built [19]. In these prototypes, the omnidirectionality is limited only to a hemisphere. The transmitter consists of an array of four laser diodes and the receiver has four optical photodetectors arranged in four quadrants. The system employs a serial communications protocol. The optical and electrical designs of the transmitter and receiver units are presented.

5.4.1 Transmitter System Design

The transmitter produces four diverging beams that cover part of a hemisphere. The transmitted beam was designed to cover up to $p/2$ sr, thus at least eight laser beams would be required to achieve full omnidirectionality coverage. Each laser beam has a maximum operating optical power of 70 mW, which gives a maximum total transmitted power of 280 mW per transmitter. The center wavelength of the transmitted beam is 785 nm, and their parallel and perpendicular beam divergences, $q_{B,||}$ and $q_{B,\perp}$, are 7° and 17°, respectively.

In order to diverge the laser beam over $p/2$ sr, a strong concave lens is placed in front of each laser diode. The lens was chosen and placed such that it could achieve the optimum trade-offs between the desired beam divergence and the required power transmission to achieve reliable communications. The design optimizations were carried out using CodeV. By restricting the maximum distance between lens and laser diode, we kept the overall system as small as possible and were able to design for a focal length of the lens of –6 mm and a distance between lens and laser diode of 10 mm.

The system uses serial communication protocols in OOK modulation, i.e. the bit stream from the serial port directly modulates the laser intensity. A ‘one’ bit turns the laser diode on, while a ‘zero’ bit does not. The laser driver circuit provides fast current switching between 30 mA (laser threshold current) and 100 mA (laser operating current) using PNP silicon epitaxial transistors designed for switching applications. Since laser power is inversely dependent on temperature, a driver controlled by an optical feedback scheme is designed to maintain the laser diode at constant average optical output power level [58]. The construction of the transmitter system is schematically shown in Fig. 5.11.

5.4.2 Receiver System Design

The receiver needs to accept a transmitted beam over a large angular range, and be fast enough to respond at the desired data rate. For this purposes, a 4-array of fast response silicon photodiode detectors are used. The photodiode has large active area (±100 mm^2), 8 MHz bandwidth, and low capacitance (375 pF). The photodiode dark current is 600 nA and the responsivity is 0.55 A/W at 785 nm. To filter out ambient light, 3 cavity band pass interference filters with nominal center wavelength of 782.5 nm and 10 nm bandwidth are used. The optical filter has a narrow transmission band with 40 dB blocking outside the pass band, which removes most background light.

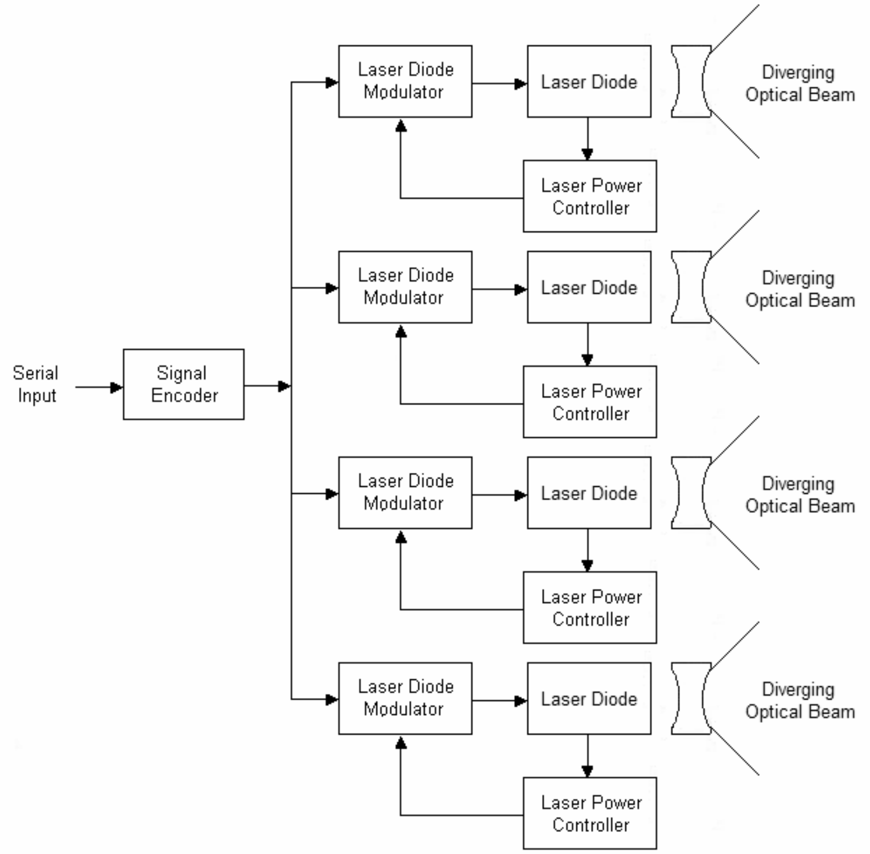

Figure 5.11: Block diagram of the transmitter in an omnidirectional FSO system.

As in typical FSO systems, the receiver uses direct detection and operates in a current mode. Since the received optical power is typically low, a variable amplifier is used to amplify the current produced by the photodiode [59]. The amplifier circuit is constructed using a high-speed op amp with unity gain stable bandwidth of 10 MHz. The receiver 3 dB bandwidth was designed to set around 4 MHz and was determined by the time constant of the amplifier feedback resistor and photodiode capacitance.

The signal is then threshold detected and re-shaped for data recovery process. For optimum detection, the threshold value can be adjusted depending on the noise level that appears in the system. To recover the transmitted information, the detected data from each branch are logically added using a quad input OR gate. The recovered information is then converted into a serial data format and passed to the serial port of the host computer. Fig. 5.12 shows the block diagram of our omnidirectional FSO receiver system.

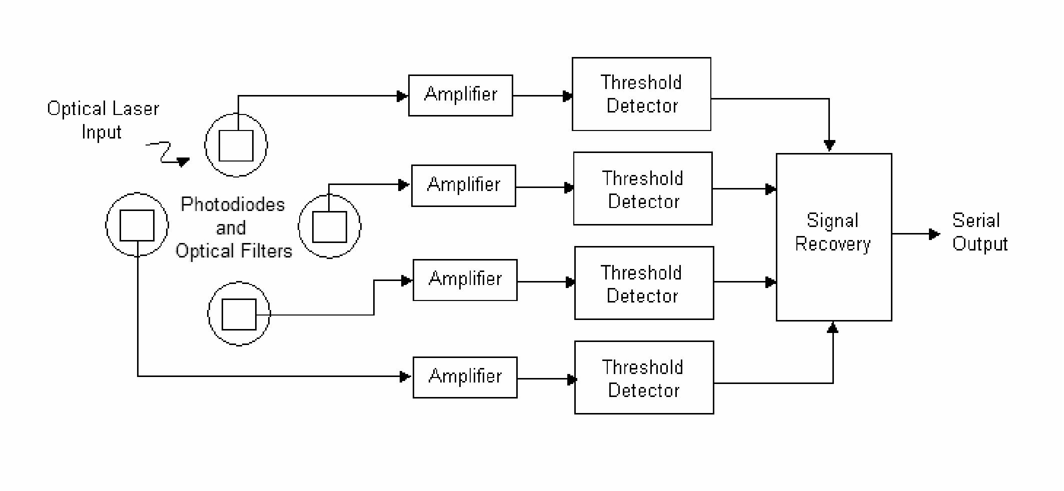

Figure 5.12: Block diagram of the receiver in an omnidirectional FSO system.

5.5 Overall Transceiver Experimental Performance

The system was primarily designed to operate at an optimum data rate of 115 kbps in serial communications and a typical operating range around ten meters. This data rate is consistent with the RS-232 standard we were using for a communications protocol. Higher operation rates are possible if different control protocols are used, for example up to 10 Mbps data rate may be obtained if RS-485 protocol is used. The optomechanical design and construction is made such that a hemisphere area can be covered. Fig. 5.13 shows a prototype of a fully functional omnidirectional FSO transceiver system.

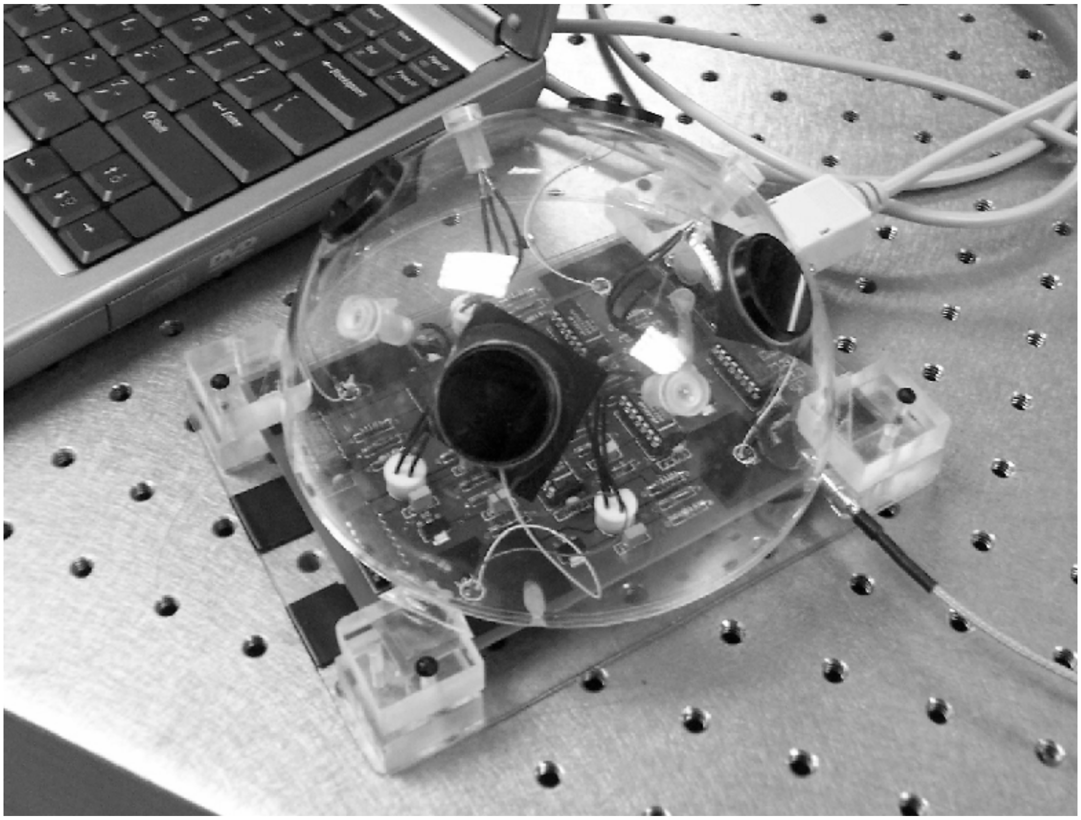

Figure 5.13: Prototype of the omnidirectional FSO communication system.

We had tested the performance of an optical link between two of our omnidirectional FSO transceivers. The experimental results are summarized in Figs. 5.14 and 5.15, and are fitted to theoretical curves for system with SNR of 22.7 dB and operating bandwidth of 730 kHz, respectively. As expected, achievable ranges out to 10 m have been achieved at audio data rates. The performance decreases with operational range in quite good agreement with the predictions of our simulations. At an operational range of 10 m a data rate of 3.9 kbps has been achieved, and the BER performance deteriorates to about 5×10^{-3}.

The performance of the unit degrades in the presence of high levels of ambient lighting, for example in direct sunlight outdoors. The current narrow band interference filters used allow a relatively broad range of wavelengths to pass through them because ambient light can pass through over a large range of angles. This effect can be reduced by utilizing more photodetectors array and efficiently limiting their FOV. Another way to reduce receiver sensitivity to background ambient light is by modifying the receiver electronics to provide active DC level compensation.

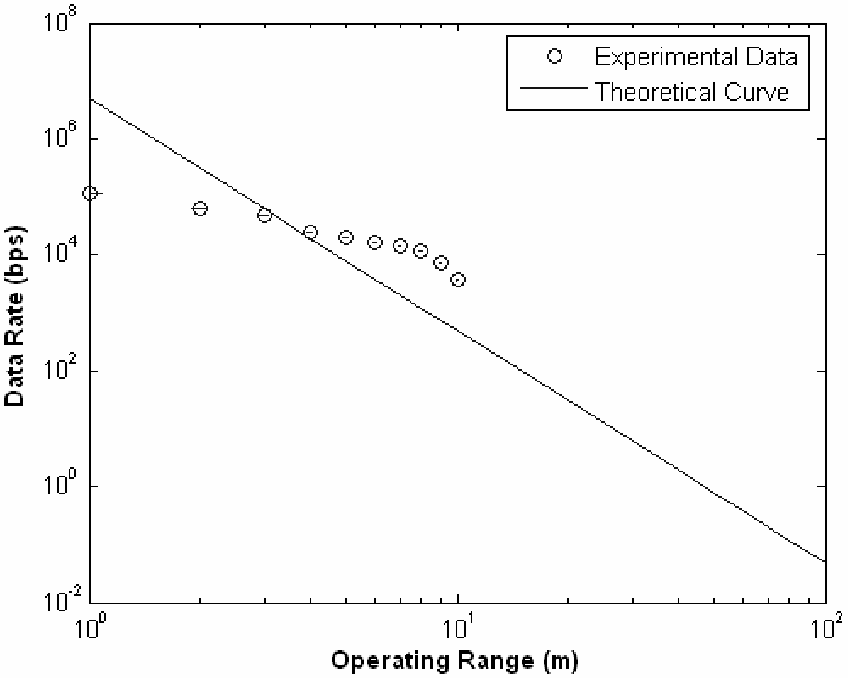

Figure 5.14: Measurements of achievable data rate in omnidirectional FSO link. The theoretical curve was calculated based on Eq. (5.9) for $\Gamma \cong 22.7$ dB.

In certain hi-tech military applications, various infrared sources with wavelengths range from 632.8 to 1064 nm are commonly used as laser range finders, ground/vehicle laser locator designators, for night vision illumination, etc. They have the potential of producing additional interference for the receiver, since these wavelengths are detectable at the photodetectors. However, these optical sources are typically operated at low modulation frequencies or DC. By implementing electrical band pass filter circuits with a center frequency in the data rate of interest, this particular type of interference should be substantially reduced.

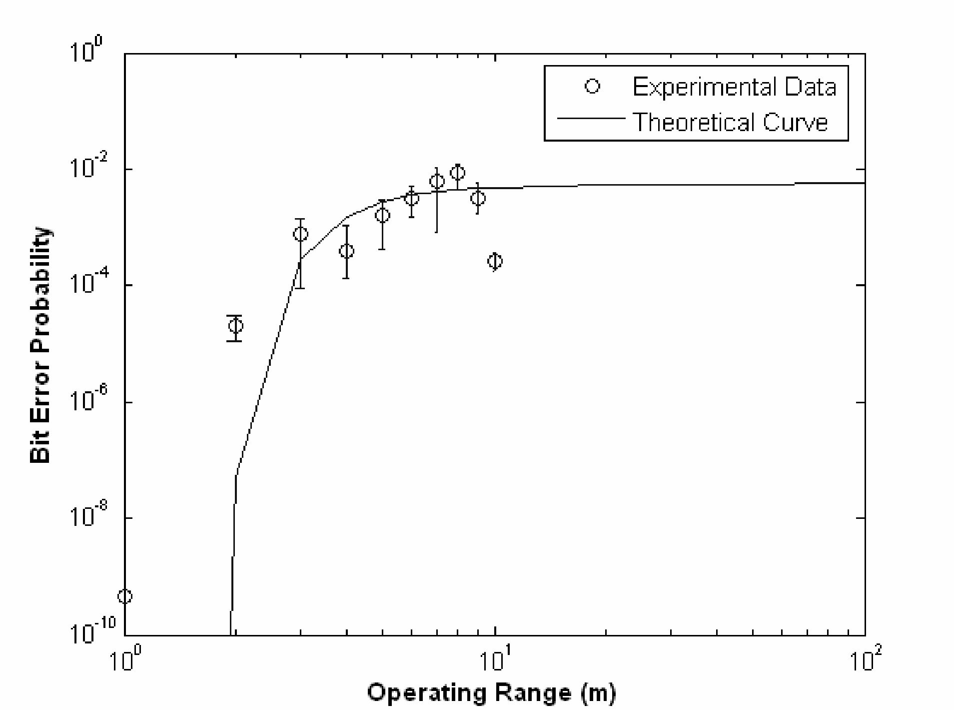

Figure 5.15: BER performance of prototype omnidirectional FSO transceiver. The theoretical curve was calculated based on Eq. (2.38) for $\Delta f \cong 730$ kHz.

5.6 System Level Design Issues

The discussions in the previous sections have concentrated on the physical layer problem of point-to-point communications using non-directed FSO links. The purpose of this section is to present some of the issues that arise in designing FSO networks using the omnidirectional links. The fundamental non-physical layer problems faced in the design of a FSO network, or wireless networking in general, are: how to multiplex data onto the downlink signals, and how to provide multiple access to the uplink node [60]. The solutions to these problems will depend on the applications and network environments.

From the perspective of higher network layers, an optical wireless network is mostly similar to a radio frequency (RF) network. Therefore, the concept of cellular based networks can also be applied to FSO networks. Without any constraints on the wavelengths and sub-carrier frequencies of the up link and down link, communication between nodes can be viewed as taking place on a shared bidirectional bus. Therefore, in principle, it should be possible to adapt any bus protocol to the wireless case. The protocol designed to isolate the uplink and downlink transmissions is needed to prevent interference and can be achieved without sacrificing capacity (due to large available bandwidth).

Two other typically used architectures are: wavelength duplex and sub-carrier duplex systems. In a wavelength duplex system, the up-link transmissions can be isolated from the downlink transmissions by using different wavelengths for the up and down links. In a sub-carrier duplex system, the electrical bandwidth is divided into sub-band allocated to the uplink and downlink, reducing amount of available bandwidth on each link. For ad-hoc networking, each unit would be required to have the capability to transmit and detect at either two distinct wavelengths or carrier frequencies. Thus, in adopting these schemes, the complexity of the physical layer is added for the benefit of simplifying the higher layers of the networks.

5.7 Summary

Experimental work in the design and construction of omnidirectional FSO transceivers is presented, and their performance is studied and analyzed. The results are valuable for understanding the challenges and potential of these promising systems. Omnidirectional transmitter systems are realized using beam diverging optics in front of laser diodes array. Specialty optical component, such as CPC, can also be used to get better omnidirectionality performance at the expense of increasing cost and complexity. The use of narrow FOV receiver elements can also improve the performance of a non-directional FSO link. This performance improvement is due to the reduction in background noise and from reduced multipath distortion in such a system.

Omnidirectional FSO systems provide a broadcast capability, which is an important requirement for all types of network, to distribute node status and control information over the network. Once the FSO link has this capability, the relationship between the physical layer and higher layers for an omnidirectional FSO network is similar to those for a cellular-based RF network. Thus, based on particular requirements and applications, an appropriate network topology can be implemented. Furthermore, the designer of a FSO network has more degrees of freedom in designing network architecture, because of the abundant bandwidth of the optical spectrum, and also because FSO links are less susceptible to multipath interference.

Chapter 6: Conclusions

6.1 Summary of Main Contributions

The analysis and practical design of two advanced enhancements to free space optical (FSO) communication systems are presented in this dissertation. They are intended to deal with two important issues in FSO communications, namely: atmospheric turbulence on long-range point-to-point connections and multi-connectedness for networking applications. On long-range FSO links, atmospheric turbulence causes intensity fluctuations and degrades the bit error rate (BER) performance. Through theoretical and experimental studies, the use of time delayed diversity shows the ability to significantly improve the FSO link performance. For networking applications, broadcasting capability is frequently required to establish and maintain communications among multiple nodes. An omnidirectional FSO system, which is based on non-directed line-of-sight (LOS) technique, is shown to have the potential to provide this important inter-node communication capability.

Theoretical analysis and performance characterization of a time delayed diversity FSO system are presented. Weak intensity fluctuation conditions are observed on our experimental range and are used as the channel model throughout the derivations. Experimental system have been designed and constructed to study the performance of this technique under simulated convective and clear atmospheric turbulence. In both cases, the performance of time delayed diversity system is shown to offer a notable improvement compared to non-diversity FSO system. Furthermore, the experimental performance results are shown to be in a very good agreement with the theory, and can achieve the ideal performance of a dual diversity system. We anticipate that our results will encourage the implementation of this novel technique in future commercial FSO system.

Prototypes of omnidirectional FSO transceiver are designed and their performance is studied. Investigations of the theoretical performance of the omnidirectional system have been conducted for different performance scenarios. In order to get performance comparable to the directional FSO system, the receiver has to be near ideal and would probably need to be a coherent receiver. The experimental studies show that omnidirectional FSO links cannot be expected to provide the range or data rate performance of directional FSO links, yet they have unique capabilities that can be exploited in sensor networks, for example as data egress or locator beacons. They may also provide an alternative medium for traditional wireless networks, when radio frequency (RF) technology cannot be used due to security and/or interference concerns.

6.2 Future Work

This dissertation is pioneering in its efforts to implement the two advanced enhancements in FSO communication systems, namely: time delayed diversity and omnidirectionality. Therefore, some suggestions can be made for future research in the design of FSO communication systems. For example, in the current time delayed diversity receiver system, the random signal is threshold detected using a constant threshold value, yielding non-optimal system performance. As it has been shown in Chapter 3, the ideal performance may be achieved if adaptive thresholding is used.

Since the signal fluctuation is relatively slow compared to the data, a digital low pass filter can be used to provide the dynamic threshold. Therefore, future research could try to incorporate this method into the system and should provide additional performance improvement.

Another possible receiver improvement is in the data recovery process. In the current system, logical addition, which assumes that the turbulence always causes a fading channel, is used. However, in reality, intensity fluctuations can cause either a fading or surging channel. An intensity measurement device can be incorporated into the system to monitor the state of the channel. When the channel is fading a logical addition is performed, otherwise a logical multiplication is performed. It has also been shown that polarization shift keying (PolSK) modulation gives better performance over the on-off keying (OOK) modulation in FSO communications under turbulence condition. The utilization of PolSK modulation in time delayed diversity FSO system should be studied in future research. Lastly, the integration of the overall system into a single microcontroller board could also be implemented.

In the omnidirectional FSO system, the design of the optical front-end is critical in obtaining the optimum omnidirectionality. Despite their costs and complexity, compound parabolic concentrators (CPCs) are ideal for beam shaping optics, and their utilizations for omnidirectional transmitters should be explored in the future research. It is also possible to use CPCs as optical front-ends at the receiver. By directly placing a photodetector at the CPC exit aperture, an effective optical gain can be obtained. Since the CPC typically has only modest field-of-view (FOV), several units have to be combined to form a single receiver [18]. The design and performance of the CPC based optical front-end for an omnidirectional transceiver also needs to be investigated.

Ongoing development of UV emitting semiconductor lasers promises the availability of lasers operating in the solar-blind region of the spectrum [61]. This would be the ideal operational wavelength for an omnidirectional FSO system, as there is no ambient light in the solar blind region and it lies outside the wavelength ranges commonly used in military systems. Also, it will be more advantageous if omnidirectional FSO transceiver could have many more and narrower beam divergence transmitters. To minimize power requirements, the system could identify which transmitter is effective in linking to a neighboring receiver, and then not power up the un-needed transmitter lasers. As MEMS beam steering technology improves and matures, it should be possible to exploit such devices in an intelligent omnidirectional FSO transceiver.

Bibliography

[1] A.C. Boucouvalas, "Challenges in Optical Wireless Communications", in *Optics & Photonics News*, Vol. 16, No. 5, 36-39 (2005).

[2] I.I. Smolyaninov, L. Wasiczko, K. Cho, C.C. Davis, "Long Distance 1.2 Gb/s Optical Wireless Communication Link at 1550 nm", in *Free-Space Laser Communication and Laser Imaging*, Proc. SPIE 4489, 241-250 (2002).

[3] C.C. Davis, I.I. Smolyaninov, "Effect of atmospheric turbulence on bit-error rate in an on-off-keyed optical wireless system," in *Free-Space Laser Communication and Laser Imaging*, Proc. SPIE 4489, 126-137 (2002).

[4] A. Acampora, *Last Mile by Laser* (Scientific American, 2002).

[5] P. Gupta, P.R. Kumar, "The capacity of wireless networks", IEEE Trans. Inf. Thry. **46**, 388-404 (2000).

[6] R.K. Crane, *Electromagnetic Wave Propagation through Rain*, (Wiley, New York, 1996).

[7] C.C. Davis, I.I. Smolyaninov, S.D. Milner, "Flexible Optical Wireless Links and Networks", IEEE Comm. Mag. **41**, 51-57 (2003).

[8] J.R. Barry, J.M. Kahn, E.A. Lee, D.G. Messerschmitt, "High-Speed Nondirective Optical Communication for Wireless Networks," IEEE Netw. Mag. **5**, 44-54 (1991).

[9] J.B. Carruthers, J.M. Kahn, "Angle Diversity for Nondirected Wireless Infrared Communication", IEEE Trans. Comm. **48**, 960-969 (2000).

[10] T.H. Ho, S. Trisno, I.I. Smolyaninov, S.D. Milner, C.C. Davis, “Studies of pointing, acquisition, and tracking of agile optical wireless transceivers for free-space optical communication networks”, in *Optics in Atmospheric Propagation and Adaptive Systems VI,* Proc. SPIE 5237, 147-158 (2004).

[11] T.H. Ho, S.D. Milner, C.C. Davis, “Fully optical real-time pointing, acquisition, and tracking system for free space optical link”, in *Free-Space Laser Communication Technologies XVII*, Proc. SPIE 5712, 81-92 (2005).

[12] L.C. Andrews, R.L. Phillips, C.Y. Hopen, “Aperture averaging of optical scintillations: power fluctuations and the temporal spectrum”, Waves Random Media **10**, 53-70 (2000).

[13] X. Zhu, J.M. Kahn, “Free-Space Optical Communication Through Atmospheric Turbulence Channels”, IEEE Trans. Comm. **50**, 1293-1300 (2002).

[14] A. Belmonte, A. Comeron, J.A. Rubio, J. Bara, E. Fernandez, “Atmospheric-turbulence-induced power-fade statistics for a multiaperture optical receiver”, Appl. Opt. **36**, 8632-8638, (1997).

[15] S. Trisno, I.I. Smolyaninov, S.D. Milner, C.C. Davis, “Delayed diversity for fade resistance in optical wireless communications through turbulent media”, in *Optical Transmission Systems and Equipment for WDM Networking III*, Proc. SPIE 5596, 385-394 (2004).

[16] S. Trisno, I.I. Smolyaninov, S.D. Milner, C.C. Davis, “Characterization of time delayed diversity to mitigate fading in atmospheric turbulence channels”, in *Free-Space Laser Communications V,* Proc. SPIE 5892, 388-397 (2005).

[17] S.H. Khoo, W. Zhang, G.E. Faulkner, D.C. O'Brien, D.J. Edwards, "Receiver angle diversity design for high-speed diffuse indoor wireless communications", in *Optical Wireless Communications IV*, Proc. SPIE 4530, 116-124 (2001).

[18] E.B. Zyambo, D.C. O'Brien, G.E. Faulkner, D.J. Edwards, "Design of a high-speed optical wireless LAN at long wavelengths", in *Optical Wireless Communications III*, Proc. SPIE 4214, 115-123 (2001).

[19] S. Trisno, T.H. Ho, S.D. Milner, C.C. Davis, "Theoretical and Experimental Characterization of Omnidirectional Optical Links for Free Space Optical Communications", in *Military Communications Conference 2004,* Proc. IEEE MILCOM 3, 1151-1157 (2004).

[20] H. Ghafouri-Shiraz, B.S.K. Lo, *Distributed Feedback Laser Diodes: Principles and Physical Modeling*, (Wiley, New York, 1995).

[21] G.M. Smith, J.S. Hughes, R.M. Lammert, M.L. Osowski, G.C. Papen, J.T. Verdeyen, J.J. Coleman, "Very narrow linewidth asymmetric cladding InGaAs-GaAs ridge waveguide distributed Bragg reflector lasers", IEEE Photon. Tech. Lett. **8**, 476-478 (1996).

[22] C.C. Davis, *Lasers and Electro-Optics: Fundamentals and Engineering*, (Cambridge University Press, Cambridge, 1996).

[23] G. Keiser, *Optical Fiber Communications*, (McGraw-Hill, 2000).

[24] R. Otte, *Low Power Wireless Optical Transmission*, (Delft University Press, The Netherlands, 1998).

[25] A.N. Kolmogorov, “The local structure of turbulence in an incompressible viscous fluid for very large Reynolds numbers”, C.R. (Dokl.) Acad. Sci. USSR **30**, 301-305 (1941).

[26] V.I. Tatarskii, *Wave Propagation in a Turbulent Medium, trans. by R.A. Silverman*, (McGraw-Hill, New York, 1961).

[27] J.R. Barry, *Wireless Infrared Communications*, (Kluwer Academic Publishers, 1994).

[28] R.M. Gagliardi, S. Karp, *Optical Communications, 2^{nd} Ed.*, (Wiley, New York, 1995).

[29] E.A. Lee, D.G. Messerschmitt, *Digital Communication*, (Kluwer Academic Publishers, Boston, 1994).

[30] A.B. Carlson, *Communication Systems: An Introduction to Signals and Noise in Electrical Communication*, (McGraw-Hill, New York, 1986).

[31] M.D. Audeh, J.M. Kahn, “Performance Evaluation of *L*-Pulse-Position-Modulation on Non-Directed Indoor Infrared Channels”, Proc. Supercomm./ICC 94, 660-664 (1994).

[32] L.A. Chernov, *Wave Propagation in a Random Medium, trans. by R.A. Silverman*, (McGraw-Hill, New York, 1960).

[33] L.C. Andrews, R.L. Phillips, *Laser Beam Propagation through Random Media*, (SPIE Optical Engineering Press, Bellingham, 1998).

[34] R.S. Lawrence, J.W. Strohbehn, “A survey of clear-air propagation effects relevant to optical communications”, Proc. IEEE **58**, 1523-1545 (1970).

[35] L.M. Wasiczko, *Techniques to Mitigate the Effects of Atmospheric Turbulence on Free Space Optical Communication Links*, (Ph.D. Dissertation, Univ. of Maryland, College Park, 2004).

[36] H. Yuksel, *Studies of the Effects of Atmospheric Turbulence on Free Space Optical Communications*, (Ph.D. Dissertation, Univ. of Maryland, College Park, 2005).

[37] E. Jakeman, "On the statistics of *K*-distributed noise", J. Phys. A **13**, 31-48 (1980).

[38] J.H. Churnside, S.F. Clifford, "Log-normal Rician probability-density function of optical scintillations in the turbulent atmosphere", J. Opt. Soc. Am. A **4**, 1923-1930 (1987).

[39] M.A. Al-Habash, L.C. Andrews, R.L. Phillips, "Mathematical model for the irradiance probability density function of a laser beam propagating through turbulent media", Opt. Eng. **40**, 1554-1562 (2001).

[40] G.I. Taylor, "The spectrum of turbulence", Proc. Royal Soc. London A **164**, 476 (1938).

[41] J.W. Strohbehn, S.F. Clifford, "Polarization and Angle-of-Arrival Fluctuations for a Plane Wave Propagated Through a Turbulent Medium", IEEE Trans. Ant. Prop. **15**, 416-421 (1967).

[42] E.J. Lee, V.W.S. Chan, "Part 1: Optical Communication Over the Clear Turbulent Atmospheric Channel Using Diversity", IEEE J. Sel. Area Comm. **22**, No. 9, 1896-1906 (2004).

[43] H. Manor, S. Arnon, "Performance of an optical wireless communication system as a function of wavelength", Appl. Opt. **42**, No. 21, 4285-4294 (2003).

[44] R. Martini, C. Gmachi, J. Falcigia, F.G. Curti, C.G. Bethea, F. Capasso, E.A. Whittaker, R. Paiella, A. Tredicucci, A.L. Hutchinson, D.L. Sivco, A.Y. Cho, "High speed modulation and free-space optical audio/video transmission using quantum cascade lasers", Electron. Lett. **37**, 191-193 (2001).

[45] L. Wasiczko, I.I. Smolyaninov, S.D. Milner, C.C. Davis, "Studies of free-space optical links through simulated boundary layer and long-path turbulence", in *Optics in Atmospheric Propagation and Adaptive Systems VI*, Proc. SPIE 5237, 127-135 (2004).

[46] J. Goldie, "Ten Ways to Bulletproof RS-485 Interfaces", National Semiconductor, App. Note AN-1057 (1996).

[47] A. Biswas, M.W. Wright, "Mountain-Top-to-Mountain-Top Optical Link Demonstration: Part I", IPN Prog. Rep. 42-149, (Jet Propulsion Laboratory, Pasadena, 2002).

[48] D.L. Fried, G.E. Mevers, "Atmospheric Optical Effects – Polarization Fluctuation", J. Opt. Soc. Am. **55**, 740-741 (1965).

[49] A.A.M. Saleh, "An Investigation of Laser Wave Depolarization Due to Atmospheric Transmission", IEEE J. Quantum Electron. **QE-3**, No. 11, 540-543 (1967).

[50] S. Betti, G. De Marchis, E. Iannone, “Polarization modulated direct detection optical transmission systems”, IEEE J. Lightwave Tech. **10**, No. 12, 1985-1997 (1992).

[51] S. Benedetto, “Direct Detection of Optical Digital Transmission Based on Polarization Shift Keying Modulation”, IEEE J. Sel. Area Comm. **13**, 531-542 (1995).

[52] F.R. Gfeller, U.H. Bapst, “Wireless In-House Data Communication via Diffuse Infrared Radiation”, Proc. IEEE **67**, 1474-1486 (1979).

[53] H. Hashemi, G. Yun, M. Kavehrad, F. Behbahani, P. Galko, “Frequency Response Measurements of the Wireless Indoor Channel at Infrared Optics”, in *Mobile Communications: Advanced System Components*, Proc. 1994 Int. Zurich Seminar on Digital Comm., 273-284 (1994).

[54] W.T. Welford, R. Winston, *High Collection Nonimaging Optics*, (Academic Press, San Diego, 1989).

[55] S.A. Self, “Focusing of spherical Gaussian beams”, Appl. Opt. **22**, 658-661 (1983).

[56] M. Born, E. Wolf, *Principles of Optics: Electromagnetic Theory of Propagation, Interference and Diffraction of Light, 6th Ed.*, (Pergamon Press, Oxford, 1980).

[57] J.D. Rancourt, *Optical Thin Films*, (Macmillan Publishing, New York, 1987).

[58] F.S. Chen, “Simultaneous Feedback Control of Bias and Modulation Currents for Injection Lasers”, Electron. Lett. **16**, 7-8 (1980).

[59] P. Horowitz, W. Hill, *The Art of Electronics*, (Cambridge University Press, Cambridge, 1989).

[60] W.C.Y. Lee, *Mobile Communications Design Fundamentals, 2nd Ed.*, (Wiley, New York, 1993).

[61] Defense Advanced Research Projects Agency (DARPA), *Semiconductor Ultraviolet Optical Sources*, (http://www.darpa.mil/mto/suvos/).